Irradiation study of different silicon materials for the CMS tracker upgrade

DISSERTATION

zur Erlangung des Doktorgrades
des Fachbereichs Physik
der Universität Hamburg

vorgelegt von
Joachim Erfle
aus Heilbronn

Hamburg
2014

Gutachter der Dissertation:

- Dr. Georg Steinbrück, Institut für Experimentalphysik, Universität Hamburg, Luruper Chaussee 149, 22761 Hamburg, Germany
- Prof. Dr. Wolfgang Hansen, Institut für Angewandte Physik und Zentrum für Mikrostrukturforschung, Universität Hamburg, Jungiusstraße 11, 20355 Hamburg, Germany

Gutachter der Disputation:

- Dr. Georg Steinbrück, Institut für Experimentalphysik, Universität Hamburg, Luruper Chaussee 149, 22761 Hamburg, Germany
- Prof. Dr. Erika Garutti, Institut für Experimentalphysik, Universität Hamburg, Luruper Chaussee 149, 22761 Hamburg, Germany

Datum der Disputation: 24.04.2014
Vorsitzender des Prüfungsausschusses: Dr. Michael Martins
Vorsitzender des Promotionsausschusses: Prof. Dr. Peter Hauschildt
Leiterin des Fachbereichs Physik: Prof. Dr. Daniela Pfannkuche

Abstract

Around 2022, an upgrade of the LHC collider complex is planned to significantly increase the luminosity (the High Luminosity LHC, HL-LHC). This means that the experiments have to cope with a higher number of collisions per bunch crossing and survive in a radiation environment much harsher than that at the present LHC. Especially the tracking detectors have to be improved for the HL-LHC. The increased number of tracks requires an increase of the number of readout channels while the higher radiation makes new sensor materials necessary. Within CMS, a measurement campaign was initiated to study the performance of different silicon materials in a corresponding radiation environment. To simulate the expected radiation the samples were irradiated with neutrons and with protons with two different energies.

Radiation damage can be divided in two categories.
First, ionizing energy loss in the surface isolation layers of the sensor leads to a change of the concentration of charged states in the sensor surface and therefore alters the distribution of the electrical fields in the sensor.
Second, non-ionizing energy loss in the bulk of the sensor material leads to a variety of defects in the silicon lattice. Electrically active defects can influence the material properties.
The three properties under investigation are the reverse current, the full depletion voltage and the charge collection. While the reverse current and full depletion voltage influence the power dissipation and the noise of the detector, the charge collection directly influences the measurement.
The material properties were studied using pad and strip sensor. The structures were electrically characterized before and after irradiation with different fluences of neutrons and protons, corresponding to the expected fluences at different radii of the outer tracker after $3000\,\mathrm{fb}^{-1}$. The charge collection measurements were mainly performed using the ALiBaVa readout system and the charge was induced with β-sources and lasers.

In addition to the bulk properties, surface effects were studied. It was found that surface conditions have a great influence on the charge collection as well as on the noise and therefore have to be considered in the design of silicon sensors.

Zusammenfassung

Um 2022 ist eine Aufrüstung des LHC und seiner Vorbeschleiniger geplant, um die Luminosität zu erhöhen. Diese Ausbaustufe heißt High Luminosity LHC, HL-LHC. Die höhere Luminosität bedeutet für die Experimente, dass sie mit einer höhren Zahl von Kollisionen pro Paketkreuzung arbeiten müssen und die höhere Strahlung des HL-LHC im Vergleich zum LHC überleben müssen. Vor allem die Spurdetektoren müssen dafür verbessert werden.
Die höhere Anzahl von Spuren macht eine vergrößerte Zahl von Auslesekanälen und die höhre Strahlenbelastung neue Sensormaterialien notwendig. Innerhalb von CMS wurde eine Messkampagne gestartet, um verschiedene Siliziummaterialien nach einer hohen Strahlenbelastung zu testen. Um die erwartete Strahlung zu simulieren wurden die Teststrukturen mit Neutronen und mit Protonen niedriger und hoher Energie bestrahlt.

Die Strahlenschäden können in zwei Kategorien aufgeteilt werden:
Erstens führt ionisierender Energieverslust in der Oberfächenisolationsschicht des Sensors zu einer Änderung der geladenen Zustände in der Sensoroberfläche und verändert damit das elektrische Feld im Sensor.
Zweitens führt nicht ionisierender Energieverlust im Siliziummaterial zu einer Reihe von verschiedenen Defekten im Siliziumgitter. Elektrisch aktive Defekte können die Materialeigenschaften verändern.
Die drei untersuchten Eigenschaften sind der Leckstrom, die Verarmungsspannung und die Ladungssammlung. Während der Leckstrom und die Verarmungsspannung die Verlustleistung und das Rauschen des Detektors beeinflussen, beeinflusst die gesammelte Ladung direkt die Messung.
Zur Untersuchung der Materialeigenschaften wurden Flächensensoren und Streifensensoren verwandt. Die Teststrukturen wurden mit Neutronen und Protonen entsprechend der erwarteten Fluenzen an verschiedenen Radien des äusseren Spurdetektors nach 3000 fb^{-1} bestrahlt und vor und nach Bestrahlung elektrisch charakterisiert. Die Messung der Ladungssammlung wurde hauptsächlich mit dem ALiBaVa Auslesesystem durchgeführt. Die Ladung wurde dabei mit Hilfe von β-Quellen und Lasern induziert.

Zusätzlich wurden Oberflächeneffekte untersucht. Es wurde ein großer Einfluß der Oberflächenbedingunden auf die Ladungssammlung und das Rauschen gefunden. Die Oberflächeneffekte sollten im Design der Siliziumsensoren berücksichtigt werden.

Contents

The Large Hadron Collider

1.1 The collider

The Large Hadron Collider (LHC) is a 27 km long proton-proton collider at CERN[1] near Geneva. It was built in a tunnel 50 m to 150 m underground. The nominal energy of 7 TeV per beam (collision energy of 14 TeV) should be reached after the first long shutdown in 2013/2014, whereas from 2009 to 2013 only an energy of 3.5 to 4 TeV per beam is used. The protons run through a system of pre-accelerators (Linac2 (50 MeV), Booster (1.4 GeV), PS (28 GeV), SPS (450 GeV)) (see figure 1.1).

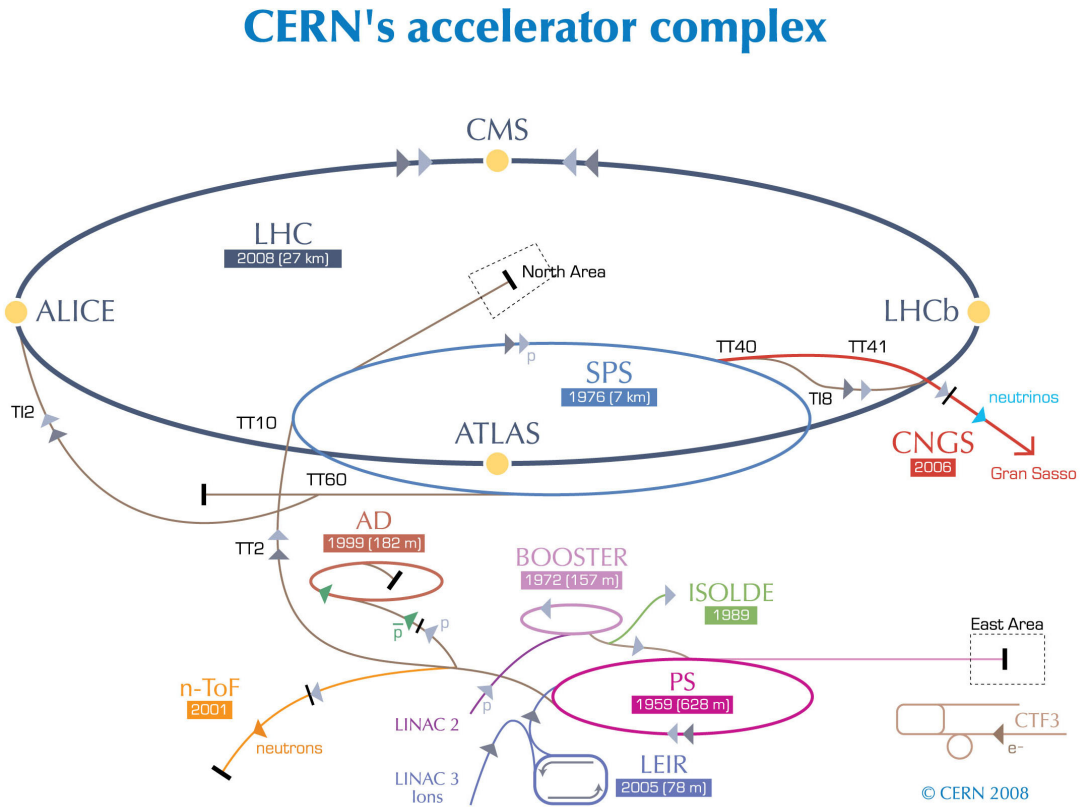

Figure 1.1: CERN accelerator scheme. Figure taken from [1].

The main purpose of the LHC is the search for new particles, like the Higgs boson or super-

[1]CERN: Conseil Européen pour la Recherche Nucléaire, en: European Organization for Nuclear Research

symmetrical particles. Therefore the collision energy is higher than in previous machines as the Fermilab TeVatron (near Chicago) with 1.96 TeV.

1.2 The experiments

1.2.1 A Large Ion Collider Experiment (ALICE)

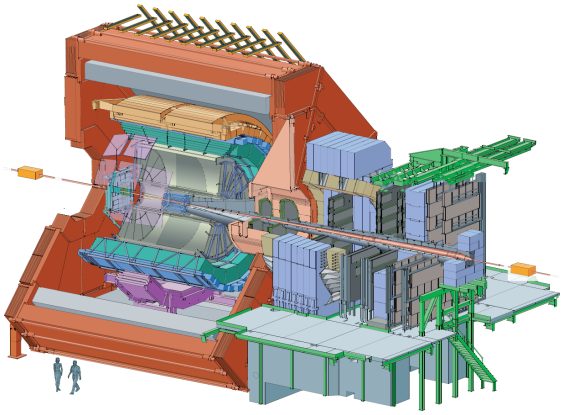

Figure 1.2: The ALICE detector. Figure taken from [2].

The ALICE experiment has the aim to improve the understanding of QCD. Therefore proton-proton, proton-ion and ion-ion collisions are performed, using different ions to vary energy density and volume of the quark-gluon plasma produced at the interaction point. The heaviest ion used is lead with a maximum center of mass energy of about 570 TeV. ALICE is a symmetric detector in 4π-configuration (see figure 1.2). [2]

1.2.2 A Toroidal LHC Apparatus (ATLAS)

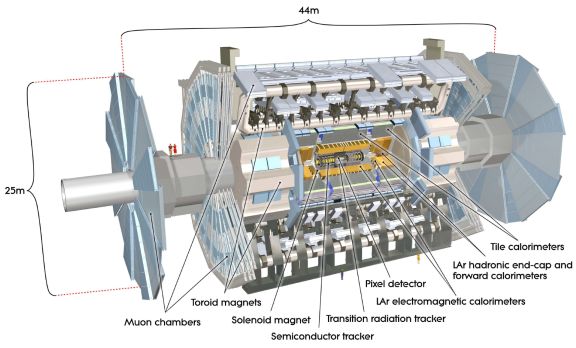

Figure 1.3: The ATLAS detector. Figure taken from [3].

Like CMS, ATLAS is a general purpose detector. That means it searches for all kinds of decays coming from proton-proton collisions. To do so, it is a symmetric detector in 4π-configuration. It is specifically designed to cope with the high luminosity of the LHC. That includes very fast and radiation hard sensors and readout-electronics throughout the detector, a very efficient trigger-system, good muon identification and missing transverse energy resolution. (see figure 1.3). [3]

1.2.3 Large Hadron Collider beauty (LHCb)

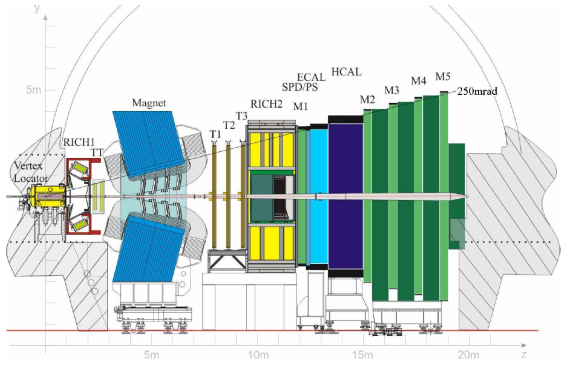

Figure 1.4: The LHCb detector. Figure taken from [4].

LHCb is a single-arm detector, covering only the forward region. It searches for CP-violation in a huge amount of B-mesons produced by the LHC. In order to get cleaner signals only about one collision per bunch crossing is realized by "luminosity leveling" by defocusing the beam, which also leads to a reduced radiation damage. This way the other experiments can run at a higher luminosity without disturbing LHCb measurements (see figure 1.4). [4]

1.2.4 Compact Muon Solenoid (CMS)

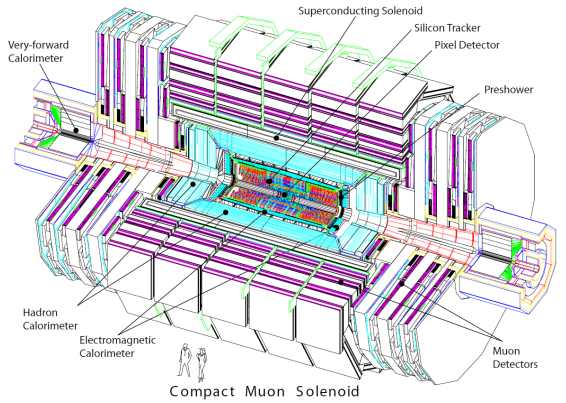

Figure 1.5: The CMS detector. Figure taken from [5].

CMS, like ATLAS, is a general purpose detector in 4π-configuration. It is designed to cope with the high luminosity including many channels for low occupancy and radiation hard materials. It has a high magnetic field to enable the silicon tracker to measure the momentum of charged particles with a high precision, a very efficient trigger-system and a good muon identification (see figure 1.5). [5]

The CMS detector consists of several sub detectors. The biggest and most important systems are

- Tracking system: locates the vertex of charged particles and tracks their path through the magnetic field to the calorimeters. Using the path of the particles, the charge and the momentum of particles can be determined.
- Electromagnetic calorimeter: This first calorimeter measures the energy of the electromagnetic particles like electrons and photons.

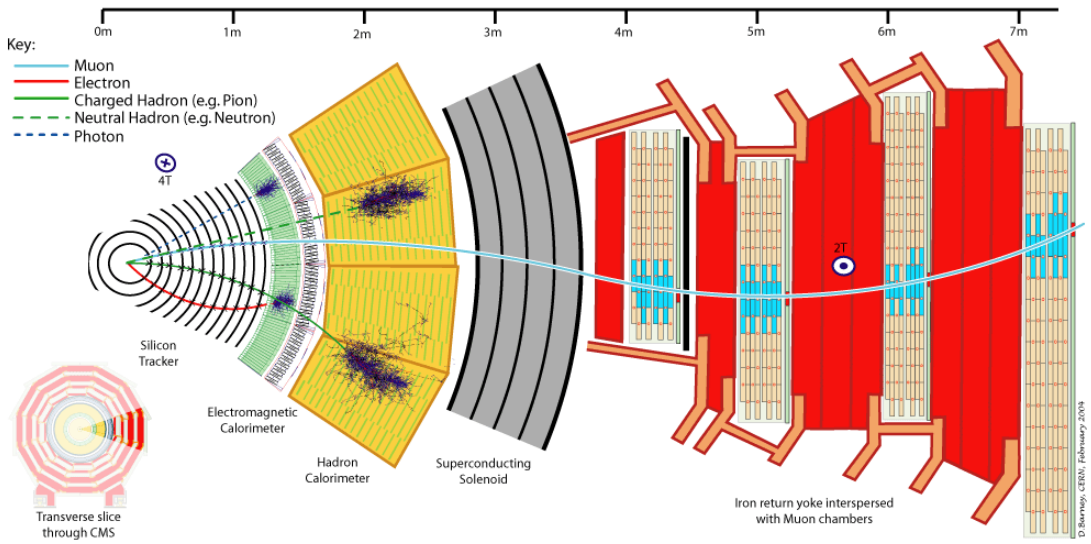

Figure 1.6: CMS transversal slice, showing typical paths for the most important measurable particles passing through CMS. Figure taken from [6].

- Hadronic calorimeter: This second calorimeter measures the energy of the hadronic particles like pions, protons and neutrons.
- Superconducting magnet: The magnetic field enables the momentum and charge measurement of charged particles of the tracker and the muon system.
- Muon system: After passing all of the material of the calorimeters and the magnet, mainly muons and neutrinos are expected to arrive at this system. This last system is dedicated to improve the momentum measurement of the muons. The muon chambers are included in the return yoke for the magnetic field. The neutrinos can not be measured in the detector and are included in the analysis using the missing transverse energy $\not{E}_t$.

In figure 1.6 the typical paths for different particle types are shown.

Tracking system

The tracking system of CMS is built of silicon sensors which are directly coupled to readout electronics. Over the whole tracking volume different sensor geometries are used. It can be divided in three sub volumes, as can be seen in figure 1.7.

- Vertex (pixel) detector: covering the innermost volume around the interaction point. In this region the particles coming from the interaction have only little distance, which means that many small channels are needed to dissolve two particles that are close to each other. In order to achieve that, it consists of 3 layers in the barrel part and 2 layers in the end caps of sensors that are structured with 100×150 µm pixels.

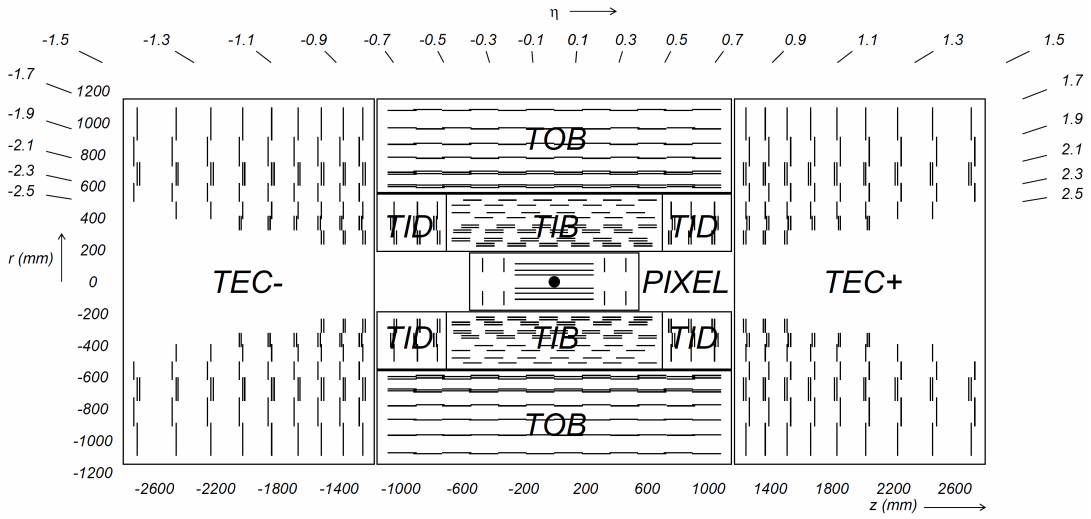

Figure 1.7: Schematic of the CMS tracking system. Figure taken from [5].

- Tracker Inner Barrel (TIB) and Tracker Inner Disk (TID): covering the volume around the pixel detector. It consists of 3 layers of sensors structured with strips of $80 - 120$ µm pitch and a length of 10 cm.
- Tracker Outer Barrel (TOB) and Tracker End Caps (TEC): covering the outer volume. It consists of either 7 (TOB) or 9 (TEC) layers of sensors structured with strips of about 180 µm pitch and a length of 25 cm. The inner three layers of the TEC sensors with a smaller pitch.

Electromagnetic calorimeter

The electromagnetic calorimeter is the first energy measurement stage, with the task to measure the energy of the light particles (like electrons and photons) with a high precision. It consists of lead tungstate crystals with a size of $28.6 \times 28.6 \times 220\,\mathrm{mm}^2$ that are installed in a volume between the tracker and the hadronic calorimeter inside the magnet. The material has a sufficient radiation hardness, a high density and provides fast signals. The drawback is that the light yield is relatively low.
This low light yield makes it necessary to use a directly coupled readout that can operate within the magnetic field and has a high gain. In order to achieve that silicon avalanche photo diodes are used in the barrel and vacuum phototriodes in the end caps.

Hadronic calorimeter

The hadronic calorimeter is the second energy measurement stage that measures the energy of the heavier particles with less precision than the electromagnetic calorimeter. In contrast to the electromagnetic calorimeter no crystals are used. Instead, the system consists of 15 brass plates with a thickness of 5 cm as absorber material and plastic scintillator tiles with a thickness of

3.7 cm in between the brass plates for detection. The light coming from the scintillator tiles is then transported via embedded wavelength shifting fibers and later on clear fibers to be read out by hybrid photo diodes.
To detect the tails of the showers a layer of scintillators is placed after the magnet. That way it is possible for the hadron calorimeter to reach more than 10 interaction length, which improves the energy resolution.

Superconducting magnet

The superconducting solenoid magnet produces a 3.8 T magnetic field inside the magnet and half of it in the muon system. This high field is needed to enable the momentum measurement, especially of the muons.

Muon system

The first measurement of the muons is in the tracker, the second is in the calorimeter. After passing the magnetic coil the muons are measured in the muon system, which tracks the muons on their path through the return yoke. Using the whole track of the muons through all of CMS and the high magnetic field, the momentum can be calculated.

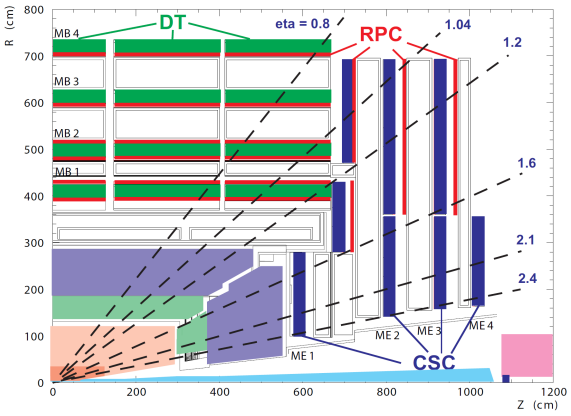

Figure 1.8: The CMS muon system. Figure taken from [7].

The muon system consists of three different detectors of which all are located inside the return yoke.

- DT: drift tube chambers have a very good spacial resolution at a low flux
- CSC: cathode strip chambers have a slightly worse resolution but can work at a higher flux than the DT
- RPC: resistive plate chambers have a high timing resolution but lower spacial resolution

Since the flux in the barrel region is lower than in the end cap region, drift tube chambers are used. Out of the four layers of DT chambers, the inner two layers are sandwiched between resistive plates, the outer two layers have only one RPC coupled to the drift tube chambers. To cope with the higher flux in the forward region, the end caps are equipped with three to four layers of CSCs coupled with RPCs. The advantage of the combination of either DT or CSC with a RPC is to have the bunch identification of the RPC together with the resolution of the DT or CSC.

1.3 Planned upgrades for the collider

This section follows [8].
As shown in figure 1.9, the LHC is planned to run with some upgrades (including the replacement of Linac2 by Linac4 and an upgrade of the PS Booster from 1.4 GeV to 2 GeV) until 2021. It is foreseen to reach an integrated luminosity of $\mathcal{L}_{int} = 500 fb^{-1}$ in this period.

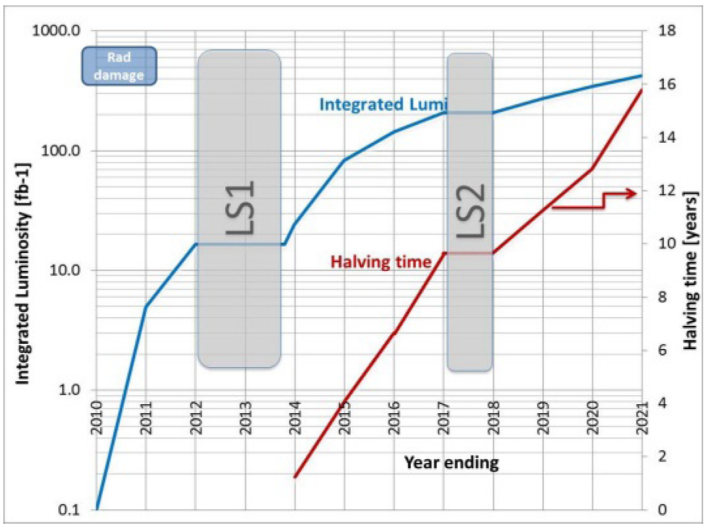

Figure 1.9: LHC upgrade timeline. After the first long shutdown, the design parameters for the design energy and luminosity will be reached. The halving time means the time needed to half the statistical error. Figure taken from [8].

After that the long shutdown 3 (LS3) is planned where the luminosity will be increased by tuning most parameters contributing to it (see table 1.1). This is needed because the statistical error is proportional to $1/\sqrt{N}$ with N the number of events.
The luminosity is given by:

$$\mathcal{L} = \frac{N_b^2 n_b f_r \gamma}{4\pi\epsilon_n \beta^*} \cdot F$$

where N_b is the number of particles per bunch, n_b is the number of bunches, γ is the Lorentz factor, F is the reduction factor which is depending mainly on the crossing angle θ_c, β^* is the amplitude function, ϵ_n is the normalized emittance and $\mathcal{L}_{peak}$ is the peak luminosity scaled to the nominal LHC luminosity. A problem that arises from the higher luminosity is that the number of collisions per bunch crossing (so-called pile up) increases to a level that is hard to handle by the experiments. Therefore it is foreseen to introduce a "luminosity leveling", which means that the peak luminosity is limited to $5 \cdot 10^{34} cm^{-2} s^{-1}$, but, in contrast to the current LHC, the average luminosity is only slightly lower. That way the integrated luminosity should reach $3000 fb^{-1}$ in about 10 years after the upgrade. In order to achieve these better beam parameters, some improvements in the collimation system are needed (including some new

Parameter	Nominal LHC	HL-LHC with 25ns	HL-LHC with 50ns
$N_b[10^{11}]$	1.15	2.0	3.3
n_b	2808	2808	1404
$\beta^*[m]$	0.55	0.15	0.15
$\epsilon_n[\mu m]$	3.75	2.5	2.0
$I[A]$	0.56	1.02	0.84
$\theta_c[\mu rad]$	300	475	445
L_{peak}	1	7.4	8.4

Table 1.1: HL-LHC Parameters for 25 to 50 ns bunch spacing. Table taken from [8].

superconducting magnets with a peak field of $12 - 13T$) and crab cavities will be installed to turn the bunches by a small angle to have a larger overlap.

1.4 Planned upgrades for the CMS experiment

1.4.1 Long Shutdown 1 (2013/2014)

Muon system

In the end cap a fourth disk will be installed and for the high eta region ($\eta > 2.1$) the readout electronics will be replaced to achieve a higher granularity (see [9]). For the high eta region ($\eta > 1.6$) it is also under study to install Gas Electron Multiplier (GEM) detectors in areas where no RPCs are installed (see [10]).

1.4.2 Extended shutdown (2016/2017)

Tracker

The pixel detector will be replaced by a new detector. It will be equipped with the same kind of sensors and an improved version of readout electronics to cope with higher pileup. To improve vertexing at high pile up an extra layer is added (4 barrel layers plus 3 end cap disks instead of the 3 barrel layers and 2 end cap disks of the current pixel detector). In addition, the inner radius is reduced which requires a new beam-pipe. To reduce the material budget and improve the cooling performance the cooling system will be replaced by a CO_2 two phase cooling system and electronics is moved further out. [11]

1.4.3 Long Shutdown 2 (2017/2018)

Hadronic calorimeter

While the readout part is replaced, both the scintillation material and the absorber material will stay the same. Nevertheless it is being investigated if the number of channels can be increased to better handle high pile up events. In the readout system three subsystems are foreseen to be replaced:

- Photo sensor: the current hybrid photo diodes (HPD) will be replaced by silicon photo multipliers (SiPM) that offer a higher gain and a higher dynamic range.
- Readout chip: the current readout chip could not cope with the higher gain of SiPMs. To benefit of the SiPMs a new chip with a higher range is being developed. The new chip will also include precision timing within the 25 ns integration time.
- Data link: the new chip needs more bandwidth, so the transmitter and receiver are replaced.

Using this new readout chain, the HCAL will improve its performance with respect to high pile-up events, out-of-time particles and direct hits of the photo sensor. [12]

1.4.4 Long Shutdown 3 (2021/2022)

The muon System

To improve the level 1 trigger performance in the HL-LHC era, a better p_t resolution is needed. In order to achieve that it is planned to place a muon tracking layer (The Muon Track fast Tag (MTT)) between the hadronic outer calorimeter (HO) and the Muon system. One MTT module will probably consist of a $10 \cdot 10 \cdot 0.5\,\mathrm{cm}^3$ scintillator and two SiPMs. [13]

Tracker

This section follows [14].
The strip tracker (TOB, TEC, TIB and TID) will be replaced by a completely new silicon tracker. This includes new types of modules, capable of delivering input to the level 1 trigger. In order to achieve that, three types of double modules are under discussion:

- The "2S" module: Two strip sensors with 5 cm long strips at a distance of about $1 - 4\,\mathrm{mm}$ are both connected to the same readout chips on either side (see figure 1.10).
- The "PS" module: One short-strip (2.5 cm) and one long-pixel sensor (1.5 mm) are placed at a distance of about $1 - 2\,\mathrm{mm}$ (see figure 1.10). The data of the strip readout is then shipped to the pixel chips which do the combination.
- The "VPS" module: Similar to the "PS" module but with an 3D interposer plus readout electronics in between the sensors. This makes shorter strips (1 cm) possible by connecting the strips from the ”top” instead from the side (see figure 1.11).

All of these possible modules are then able to detect tracks that seem to have a high p_t. The two hits combined form a so-called “stub” that will be shipped out to a tracker internal pattern recognition unit. This pattern recognition unit will then build tracklets from several single stubs. If a tracklets looks promising, this information is shipped to the level 1 trigger (see [15]).

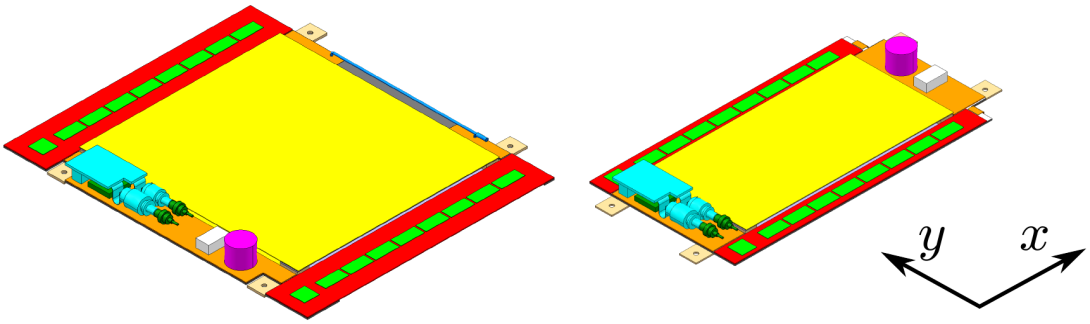

Figure 1.10: On the left: 2s (2 strip) module with 2 long-strip sensors. Both strip sensors are connected with wire bonds to the readout chips.
On the right: PS (pixel strip) module with a strip sensor on one side and a long-pixel sensor on the other. The pixel sensors are bump-bonded to pixel readout chips and the strip sensors are wire bonded to strip readout chips. Both chip types are connected to make the L1 trigger decision. Sensors are shown in yellow, hybrids in red, readout chips in green, the data link in blue and the dc-dc converter in pink. Figure taken from [14].

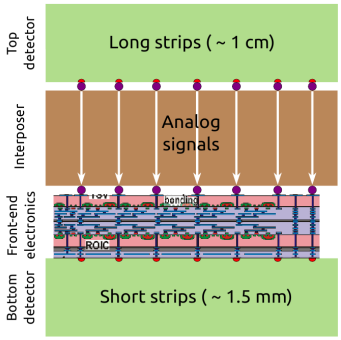

Figure 1.11: Vertically integrated Pixel Strip module (VPS). Here the strips are connected to the readout chips through an interposer material which allows for shorter strips. Figure taken from [14].

Because of the level 1 trigger capability and the higher occupancy, a new readout chip is required. The new tracker readout will be binary (so only the information which strip is hit is shipped out), contrary to the current tracker readout chip, where the analogue signal height is shipped out. The advantage of a binary strip is the reduced bandwidth, while signal hieght is lost. This means that the cluster finding efficiency depends only on the threshold set in the readout chip, so the dependence on the seed signal is higher than in the case of an analogue readout. Also the position resolution is reduced, since the signal on the neighbours can not be used to improve the resolution. The third important part besides the module (including mechanics, powering and cooling) and the readout electronics is the sensor material. To withstand the higher radiation with respect to the current tracker, a new silicon sensor material is required.

Silicon tracking sensors in high energy physics

This chapter follows mainly [16] and [17].

2.1 Advantages of silicon sensors

Silicon sensors are used for particle detectors, because they have a sufficient radiation hardness, a very fast signal collection $\mathcal{O}(10\,ns)$, a high resolution $\mathcal{O}(10\,\mu m)$, a high enough signal level due to the small band gap and an acceptable radiation length.
All of these properties make silicon an ideal tracking sensor, especially for the LHC, where a readout frequency of 40 MHz is used and the high hadronic background damages the sensors. This lead all four large LHC experiments to build at least the inner tracking system out of silicon sensors.

2.2 Working principles

2.2.1 Particle detection with silicon sensors

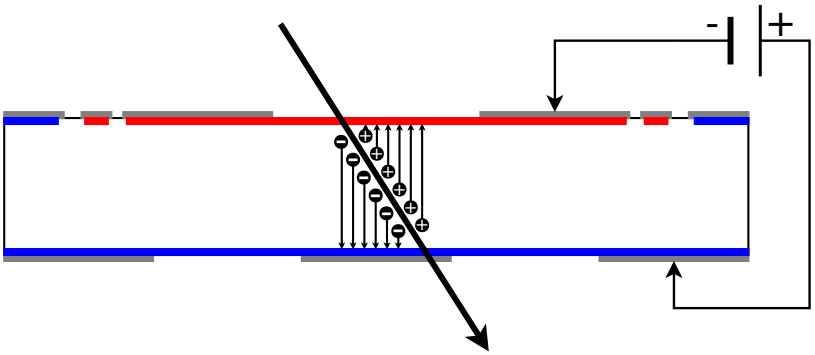

Figure 2.1: Collection of deposited charge in a silicon pad diode. A particle flying through the depleted area of the silicon pad diode ionizes atoms. Because of the applied voltage the created electrons and holes drift to the electrodes and create a measurable signal.

A charged particle flying through the silicon bulk ionizes some of the silicon atoms (see figure 2.1). In a pure silicon bulk material, the number of created charge carriers would be several orders of magnitude lower than the number of free charge carriers and a detection of

the extra charge would be impossible. To be able to measure the extra charge, the number of free charge carriers has to be reduced.
This reduction can be realized by introducing a p-n junction. At the junction a region with a very low number of free charge carriers is formed.
By applying an external voltage, this depletion zone can be enlarged. If the zone covers the whole silicon bulk the sensor is fully depleted and in a silicon detector without defects, nearly no free charge carriers would be left. In a real silicon detector with defects, the number of free charge carriers is reduced to a low enough number, so that the extra charge can be detected.

2.2.2 P-n junction

A typical signal in a silicon sensor is in the order of a few fC. The number of free charge carriers in plain silicon bulk is many orders of magnitude higher. To be able to measure the small signals, the silicon bulk has to be depleted. This can be achieved by building a p-n junction and operate it in reverse bias.
Figure 2.2 shows the properties of an abrupt p-n junction. The depletion zone that is formed by the p-n junction can be enlarged or reduced by applying an external voltage. The depletion width is given by [16] as

$$W_D = \sqrt{\frac{2\epsilon_s}{q_0 N}\left(\Psi_{bi} - V - \frac{2kT}{q_0}\right)} \tag{2.1}$$

with the lower number of dopants N (either N_A or N_D), the silicon permittivity ϵ_s, the elementary charge q_0, the built-in potential Ψ_{bi}. The polarity of the applied voltage V is such, that it is negative in reverse bias and positive in forward bias.

Capacitance of the depletion zone

For silicon sensors with uniform surface structures, the depletion width is approximately constant over the whole area and the system can be approximated as a parallel plate capacitor. Outside the depletion zone the charge carriers can move freely, so that the electrodes of the capacitor are directly at the border of the depletion zone. When the applied voltage is changed, the depletion width changes and therefore the capacitance. From that assumption the dependence of the capacitance on the depth of the depletion zone is given by [16] as

$$\frac{C_D}{A} = \frac{\epsilon_s}{A \cdot W_D} = \frac{1}{A}\sqrt{\frac{q\epsilon_s N}{2}\left(\Psi_{bi} - V - \frac{2kT}{q}\right)^{-1}} \tag{2.2}$$

with the depletion zone capacitance C_D, the area of the depleted zone A, the depletion width W_D and the applied bias voltage V.

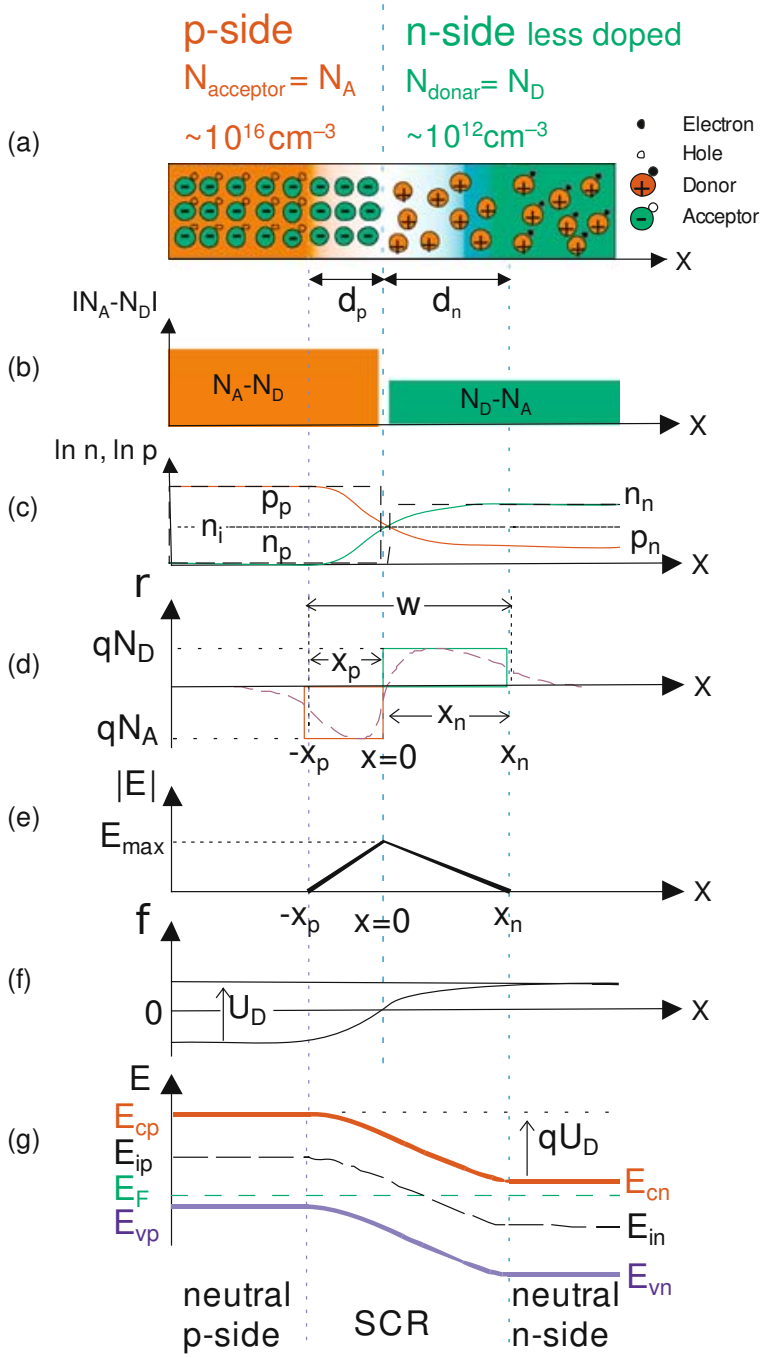

Figure 2.2: A p-n junction in thermal equilibrium. Shown are: (a) a visualization of the atomic and charge configuration, (b) the doping profile, (c) the mobile charge density, (d) the space charge density, (e) the electric field distribution, (f) the electric potential and (g) the energy-band diagram. Figure taken from [17].

Full depletion voltage

Equation 2.2 can be rearranged to (given by [16])

$$\frac{1}{C_D^2} = \frac{2}{q\epsilon_s N}\left(\Psi_{bi} - V - \frac{2kT}{q}\right) \qquad \text{for } V < V_{dep} \tag{2.3}$$

$$\frac{1}{N} = -\frac{q\epsilon_s}{2} \cdot \frac{d(1/C_D^2)}{dV} \qquad \text{for } V < V_{dep} \tag{2.4}$$

Equation 2.3 shows that for bias voltages below full depletion (the voltage where the depletion

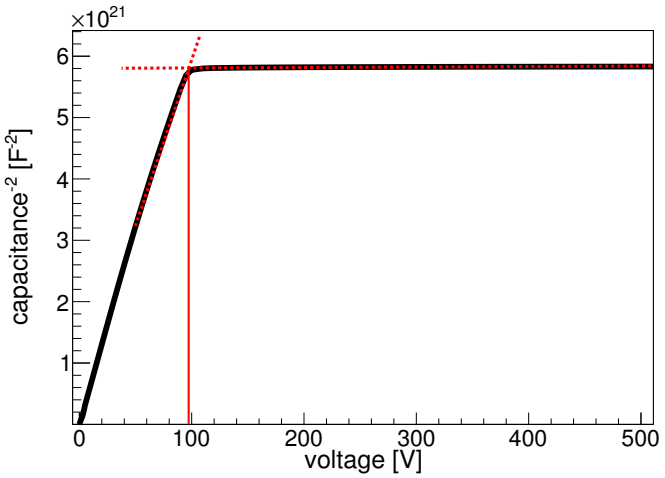

Figure 2.3: A typical C-V curve for a diode. From the intersection of the fitted straight lines (red) the full depletion voltage is extracted.

zone stretches over the full thickness of the silicon) a $1/C_D^2$ versus bias voltage plot shows a linear increase (see figure 2.3). After full depletion is reached the capacitance stays constant. This can be used to determine the full depletion voltage from the capacitance vs. voltage measurement.
The bulk doping concentration can also be determined from the slope of a $1/C_D^2$ versus bias voltage plot using equation 2.4.
To have optimal detector performance, the operating voltage should be higher than the full depletion voltage to ensure that the full sensor contributes to the charge collection.

Dark current

The dark current consists of two main contributions, the diffusion current and the generation current. A typical dark current versus voltage characteristic is shown in figure 2.4.
The diffusion current contribution comes from the non-depleted region, the generation current from the depleted zone. The full dark current is the sum of both.

Diffusion current The diffusion current is given by the Shockley equation, taken from [16]:

$$J = J_p + J_n = \frac{qD_p n_i^2}{L_p N_D}\left[exp\left(\frac{qV}{kT}\right) - 1\right] + \frac{qD_n n_i^2}{L_n N_A}\left[exp\left(\frac{qV}{kT}\right) - 1\right] \tag{2.5}$$

with the diffusion coefficients D_p and D_n, carrier life times τ_p and τ_n, density of free charge carrier concentration n_i, the dopant densities N_D and N_A and the applied voltage V.

Generation current The generation current is given by [16] as:

$$J_{ge} \approx \frac{qn_i W_D}{\tau_g} \tag{2.6}$$

with the width of the depletion zone W_D and the generation lifetime τ_g. The typical I-V curve

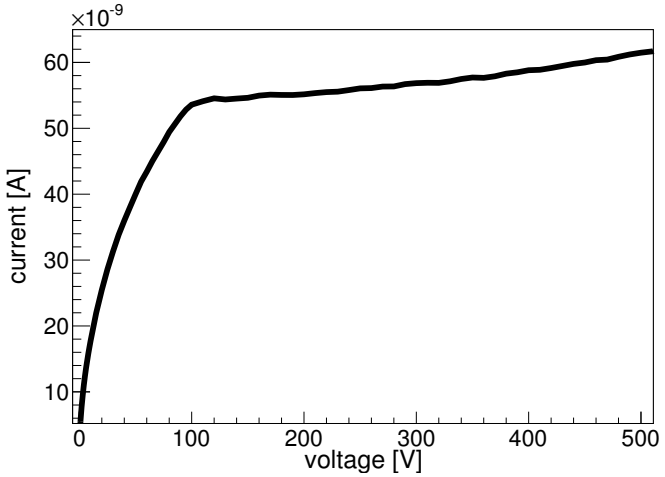

Figure 2.4: A typical I-V curve for a diode.

for a diode is shown in figure 2.4. First depletion zone grows with increasing voltage and the generation current is increased. After full depletion is reached, the current is nearly constant with increasing voltage.

Temperature dependence of the dark current The main contribution in a fully depleted diode is the generation current. The only temperature-dependent parameters of the generation current are the free charge carrier concentration n_i and generation lifetime τ_g. The temperature dependence of the free charge carrier concentration is given by (taken from [18]):

$$n_i \propto T^{3/2} exp\left(-\frac{E_g}{2kT}\right) \tag{2.7}$$

That of the generation lifetime is approximated by [18] to be:

$$\tau_g \propto T^{-1/2} exp\left(-\frac{|\Delta_t|}{2kT}\right) \tag{2.8}$$

with the difference $\Delta_t = E_t - E_i$ between the Fermi level and the defect level. This defect is the assumed source of the generation current. The number of these defects is very low in undamaged silicon sensors, but increases with radiation.
The temperature dependence of the dark current is given by (taken from [18]):

$$J \propto T^2 exp\left(-\frac{E_g + 2\Delta_t}{2kT}\right) \tag{2.9}$$

In [18] it is shown that for silicon $E_g + 2\Delta_t = 1.21$ eV should be used.

2.2.3 Energy deposition of particles in silicon

This section follows mainly [19].
The mean energy loss of heavy particles traversing through matter is described by the Bethe-Bloch formula in the range from $0.1 \lesssim \beta\gamma \lesssim 1000$ (taken from [19]):

$$-\left\langle \frac{dE}{dx} \right\rangle = Kz^2 \frac{Z}{A} \frac{1}{\beta^2} \left[\frac{1}{2} \ln \frac{2m_e c^2 \beta^2 \gamma^2 T_{max}}{I^2} - \beta^2 - \frac{\delta(\beta\gamma)}{2}\right] \tag{2.10}$$

with $K/A = 4\pi N_A r_e^2 m_e c^2 / A \approx 0.307075\,\mathrm{MeV\,cm^2/g}$, the charge of the incident particle z, the electron mass m_e, the kinetic energy T, the mean excitation energy I and the density effect correction to ionization energy loss $\delta(\beta\gamma)$.
As can be seen in figure 2.5, the mean energy loss for electrons differs from that of muons, described by the Bethe-Bloch formula.
The description of Seltzer and Berger ([22] and [23]) accounts for the differences which result in a lower minimum mean energy loss
$-\left\langle \frac{dE}{dx} \right\rangle \approx 1.53\,\mathrm{MeV\,cm^2/g}$ for a $P_{\mathrm{electron}} \approx 1.25\,\mathrm{MeV/c}$ electron, instead of
$-\left\langle \frac{dE}{dx} \right\rangle \approx 1.66\,\mathrm{MeV\,cm^2/g}$ for a $P_{\mathrm{MIP}} \approx 273\,\mathrm{MeV/c}$ muon.
The distribution function of the energy deposition is not a Gaussian distribution. In some cases a very high energy loss can occur leading to a tail on the high energy side.
Mostly the high energy deposition is due to "δ rays", where the incident particle knocks on an electron, transferring a high momentum to the electron. This "δ electron" then traverses through the silicon, ionizing many other atoms and thus inducing a high charge. The tail leads to a non-Gaussian distribution.
For minimum ionizing particles (MIPs) the distribution can be described by Landau and Vavilov, shown in figure 2.6. The most probable value of this distribution is given by (taken from

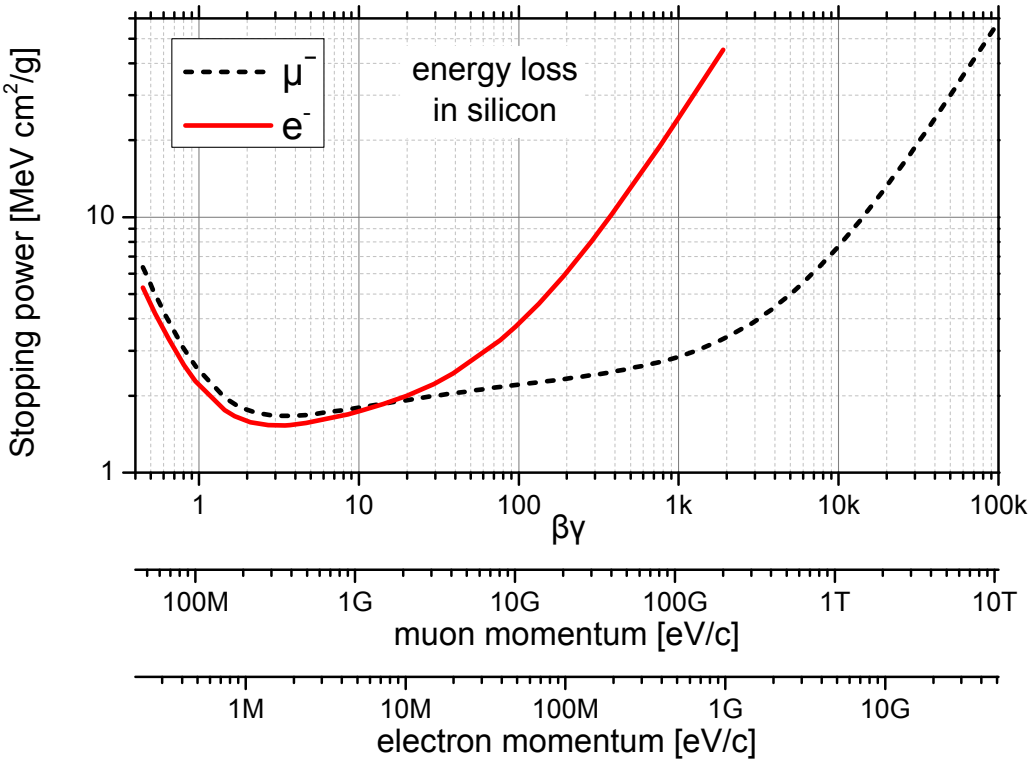

Figure 2.5: Stopping power of muons and electrons in silicon (data for muons taken from [19] which is mainly based on [20], data for electrons taken from [21] in the region P$<$ 50 MeV/c which is mainly based on [22] and [23] and [24])

[19], originally from [25]):

$$\Delta_p = \xi \left[\ln \frac{2m_e c^2 \beta^2 \gamma^2}{I} + \ln \frac{\xi}{I} + j - \beta^2 - \delta(\beta\gamma) \right] \tag{2.11}$$

with $\xi = \frac{K}{2} \left\langle \frac{Z}{A} \right\rangle \frac{x}{\beta^2}$ MeV with a thickness of the detector x in g/cm^2 and j= 0.2.

The mean energy loss $< dE/dx >$ is independent of thickness, but for muons the MPV per thickness Δ_p/x scales with $a \ln x + b$. For more information see [19].

For electrons with an energy of $\approx$ 1 to 2 MeV/c passing through silicon sensor thicknesses of $25 < x < 300\,\mu$m, a fixed factor of $\approx$ 0.8 between the mean and the MPV was found by [26]. (see figure 2.7).

The energy loss can be converted into deposited charge that can be measured in the silicon sensor by (taken from [19]):

$$N_{eh} = \left\langle \frac{dE}{dx} \right\rangle \cdot \frac{\rho_{absorber}}{E_i} \tag{2.12}$$

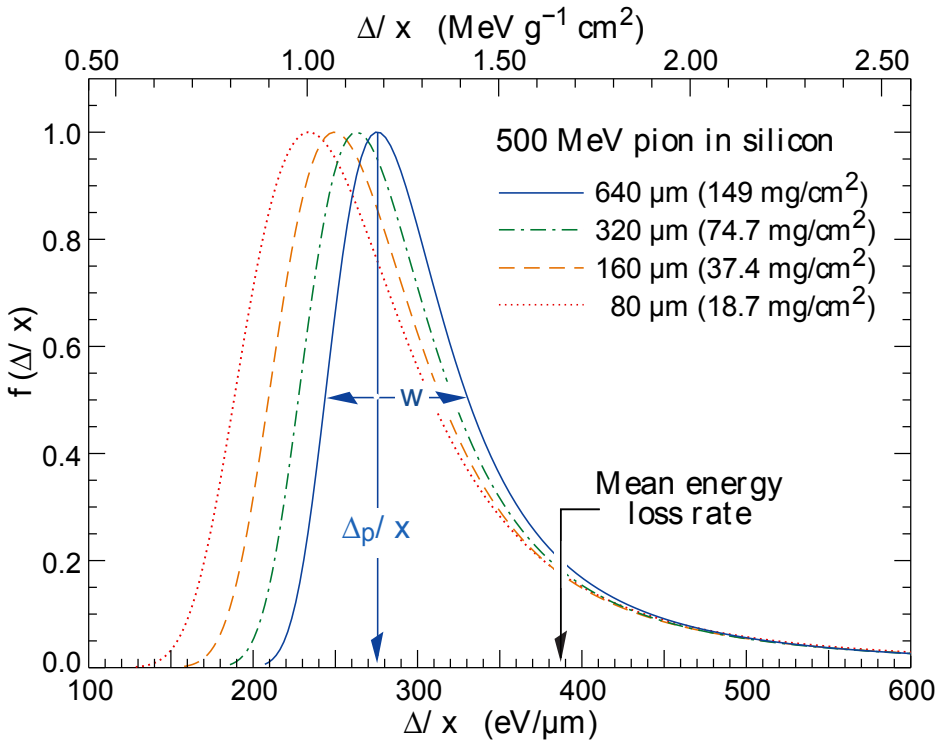

Figure 2.6: Distribution of deposited charge of 500 MeV pions in silicon with different thicknesses. The mean energy loss is different than the most probable value which is also depending on the thickness of silicon for heavy particles. Figure taken from [19].

with the number of created electron hole pairs N_{eh}, the absorber density $\rho_{absorber}$ and the mean energy to create one electron-hole pair E_i. These values for silicon are $\rho_{silicon} = 2.33\,\mathrm{g/cm^3}$ and $E_i = 3.67$ (taken from [19]). E_i was measured using high energetic photons (photon energy $\gtrsim 1.5\,\mathrm{keV}$) but it is assumed that this number also applies for electrons in the relevant energy range.

2.3 Silicon production technologies

2.3.1 Crystal growing technologies

The main production technologies for monocrystalline silicon ingots are the (magnetic) Czochralski method (see figure 2.8) and the floating-zone method (see figure 2.9).
The method that is used mainly in silicon industry is the Czochralski method, since it is pure enough for most appliances. The monocristalline ingot is produced using a seed crystal that is first brought into contact with silicon melt and then slowly pulled out while turned. Due to the contact of the silicon melt with the quartz crucible, atoms (like oxygen) can diffuse in.
This diffusion can be reduced by the magnetic enhancement. It uses magnetic fields to control

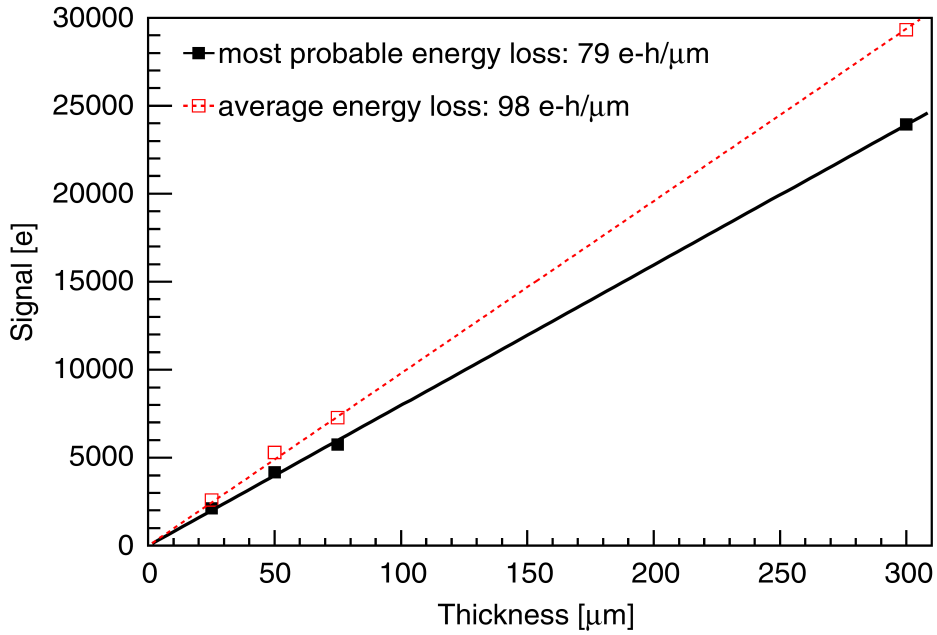

Figure 2.7: Signals of non-irradiated silicon pad sensors of different thicknesses induced by a ^{90}Sr source. The difference of the mean and the MPV that is caused by the non-Gaussian distribution, can clearly be seen. Figure taken from [26].

the fluid movements and reduces the amount of atoms diffusing in from the crucible.

The floating zone method is more expensive but produces purer silicon than the Czochralski method. A polycrystalline ingot is transformed into a mono-crystalline one by a heating coil. The coil starts from a seed crystal that is in contact with the ingot and slowly moves along and melts a small zone. When recrystallizing, the silicon takes on the crystal structure of the seed.

These mono-crystalline ingots are then sliced into wafers of a typical thickness of 300 µm to 500 µm. To produce smaller thicknesses, the wafers are polished down to a thickness of, for example, 200 µm. For small thicknesses the mechanical stability decreases. To increase the stability, two wafers with different doping concentrations can be bonded to have a thin active wafer (with a low doping concentration) on a thick inactive wafer (with a high doping concentration) giving mechanical stability.

Deep diffusion

Another method is to inactivate a part of the wafer by introducing a high number of dopants. This procedure is called “deep diffusion”.
The deep diffused materials are originally oxygen lean floating-zone materials, cut in thick

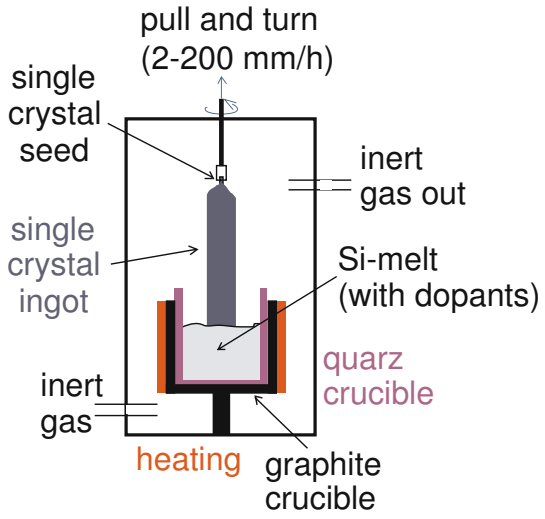

Figure 2.8: Czochralski ingot production method. A pure silicon melt is kept hot (and therefore fluid) in a quartz crucible. From the top a seed crystal is brought to contact with the melt and slowly pulled out while turning. A mono crystalline ingot forms starting from the seed. Figure taken from [17].

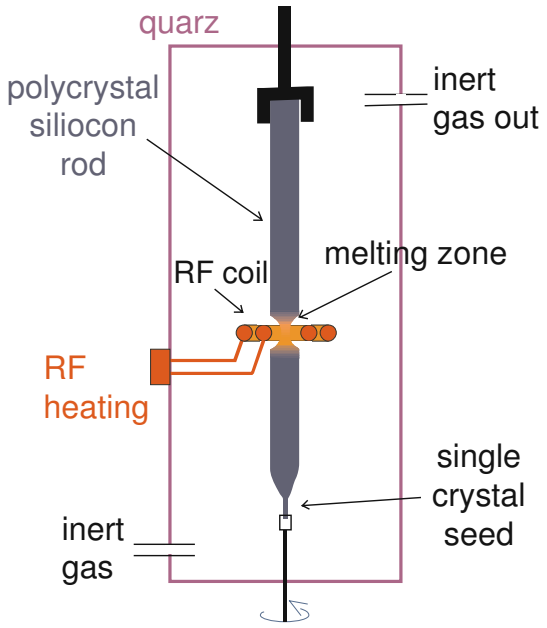

Figure 2.9: Floating zone ingot production method. A polycrystalline ingot is produced first. In the next step a seeding crystal is brought in contact with one side. A heating coil locally heats the ingot, starting from the seed. The silicon rearranges into a monocrystalline structure. Figure taken from [17].

wafers. Since it can be beneficial to have thin active sensors, a part of the sensor is made inactive by introducing a high doping from the backside. This is performed at very high temperatures ($> 1000\,^{\circ}\mathrm{C}$) and for several days, depending on the targeted remaining active thickness. The resulting rise of conductivity towards the back side is not as steep as for materials with standard backside implantation, as shown in figure 2.10.

2.3.2 Bulk doping

To control the electrical properties of silicon it can be doped with other atoms. The main dopants are boron and phosphorus with three and five outer shell electrons, respectively.
Figure 2.11 shows the principle of doping with phosphorus. Since it introduces an extra electron in the silicon lattice, it is called a donor. This extra electron acts as a free charge carrier that can move freely in the lattice.
Figure 2.12 shows the principle of doping with boron. Since it introduces a missing electron in the silicon lattice it is called an acceptor. This free electron position, or "hole", acts as a free carrier of positive charge that can move freely in the lattice, due to electrons that hop from the

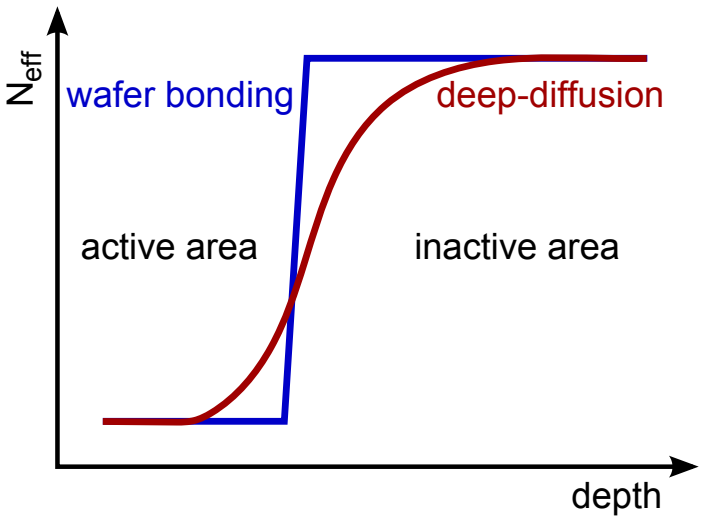

Figure 2.10: Sketch of the doping profile of a deep diffused silicon wafer.

original position to a free neighboring position.
The hole movement is done by electrons hopping from a neighboring position and is therefore slower than that of electrons.

2.3.3 Impurities of the silicon bulk

Depending on the production process there are impurities with different concentrations in the silicon. The main sort of impurities are oxygen, carbon and hydrogen. The carbon and hydrogen concentrations are usually lower than the oxygen concentration. The carbon and hydrogen concentrations are usually $< 10^{16}\,\mathrm{cm}^{-3}$. The lowest achievable oxygen concentration is $\approx 10^{16}\,\mathrm{cm}^{-3}$ for very pure floating zone silicon, but can easily be $\approx 10^{17}\,\mathrm{cm}^{-3}$. The enrichment of carbon and hydrogen concentrations has not shown a positive influence so far. For more information see[28]. An increased oxygen concentration can have a positive influence on some properties, so different production technologies are used.

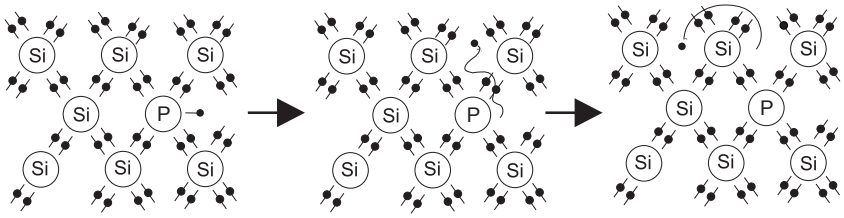

Figure 2.11: Simplified atomic model of phosphorus-doped silicon. Phosphorus has five outer shell electrons, so if an phosphorus atom replaces a silicon atom (with four outer shell electrons) one electron is free. It can move freely inside the crystal lattice and act as a free charge carrier. Figure taken from [27].

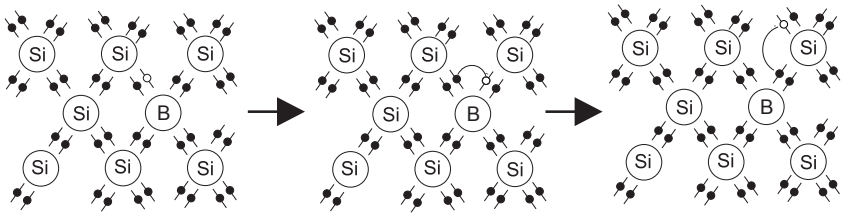

Figure 2.12: Simplified atomic model of boron-doped silicon. Boron has three outer shell electrons, so if an boron atom replaces a silicon atom (with four outer shell electrons) one electron position is free. This missing electron (often called "hole") can move inside the lattice and act as a free charge carrier. Figure taken from [27].

Radiation damage of silicon sensors

This chapter follows [29].
During the (HL-)LHC operation different charged and neutral particles are created and pass through the tracker. The particles passing through the tracker deposit energy that leads to a degradation of the used material. The composition and number of these particles varies with the position in the tracker, which has to be taken into account when predicting the damage to the tracker. In the case of silicon tracking sensors, two effects have to be addressed:

- surface damage
- bulk damage

3.1 Surface damage

Typically SiO_2 is used as an isolation layer. The particles crossing through the SiO_2 create electron-hole pairs. Most of those pairs will recombine shortly after their creation, but some will be separated by diffusion. When the electrons escape the SiO_2, the holes are trapped inside and a positive charge builds up. This charge affects the fields and can lead to very high field regions that eventually leads to an early breakdown and increase of the noise or even limit the maximum operation voltage. The positive charge in the SiO_2 also attracts electrons that can not enter the SiO_2 and build a so-called accumulation layer. Such a conductive layer may change the electric field inside the sensor and also reduce the resistance at the surface of the silicon and therefore between the strips.

3.2 Bulk damage

For a hadron environment, like the LHC, bulk damage is typically dominant. The particles crossing the sensor can knock atoms from their lattice position. These interstitial atoms can then recombine with a vacancy in the lattice and restore the old situation, or they form defects together with other interstitials or impurities. Depending on the density of single defects they can form clusters of many defects or stay small point defects. These defects influence all three essential macroscopic properties of the sensor (see also figure 3.1):

- increase of the dark current by deep defects
- increase of charge carrier trapping
- change of the full depletion voltage

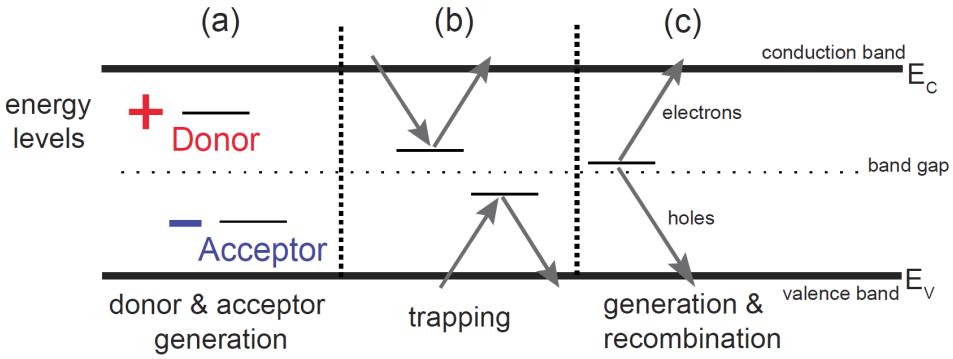

Figure 3.1: Defect levels in the silicon band gap corresponding to the three essential macroscopic effects. Defects close to the edge of the band gap have mainly an influence on the space charge (a). Defects throughout the band gap can trap charges for some time and reduce the collected charge (b). Defects in the middle of the band gap allow charge carriers to cross the band gap and increase the dark current (c). Figure based on [29], taken from [27].

The understanding of the development of the defects in silicon is important to predict if a given sensor would survive the HL-LHC run time.

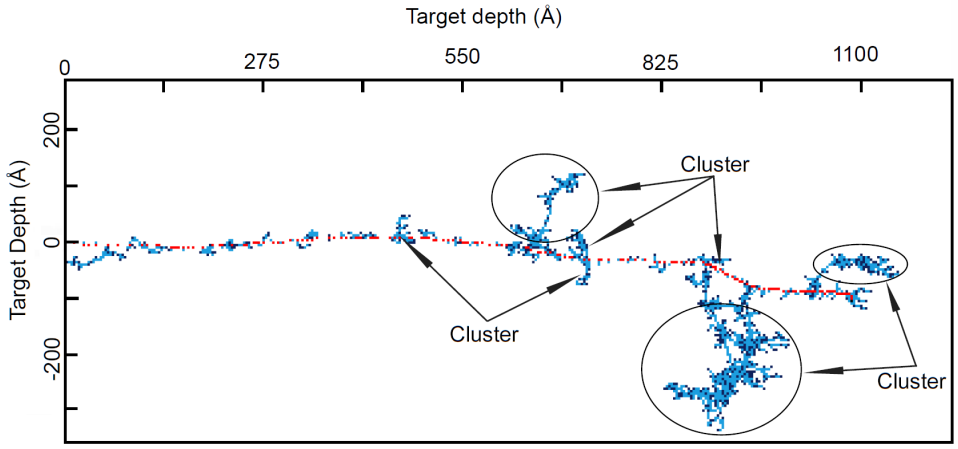

Figure 3.2: Simulation of typical silicon bulk damage caused by a 1 MeV neutron, giving the primary knock on atom (PKA) an energy of 50 keV. Atoms displaced by the PKA are shown in red, additional defects are shown in blue. Figure taken from [27].

The main part of the damage is not done by the traversing particle knocking an atom out of place, but the damage cascade caused by this first hit. This cascade depends on the energy E_R that was transferred to the primary knock on atom (PKA). Figure 3.2 shows the damage caused by a 1 MeV neutron with the average energy transfer of $E_R = 50$ keV as an example. It can be seen that the PKA causes many point defects on its way through the lattice as well as some

defect clusters consisting of many single displacements.
The energy E_R depends on the particle type and energy. Figure 3.3 shows the distribution of vacancies after the simulated passing of $1 \cdot 10^{14}\,\mathrm{cm}^{-2}$ particles of different type and energy simulated by [30].
The different cluster and point defects have to be assigned to different electrical properties and energy levels in the band gap.
There is work ongoing to understand all of these parts, for example in the thesis of [27].
A concept to predict the macroscopic changes of the silicon, using the assumption that the created damage depends on PKA energy E_R, is called non-ionizing-energy-loss (NIEL).

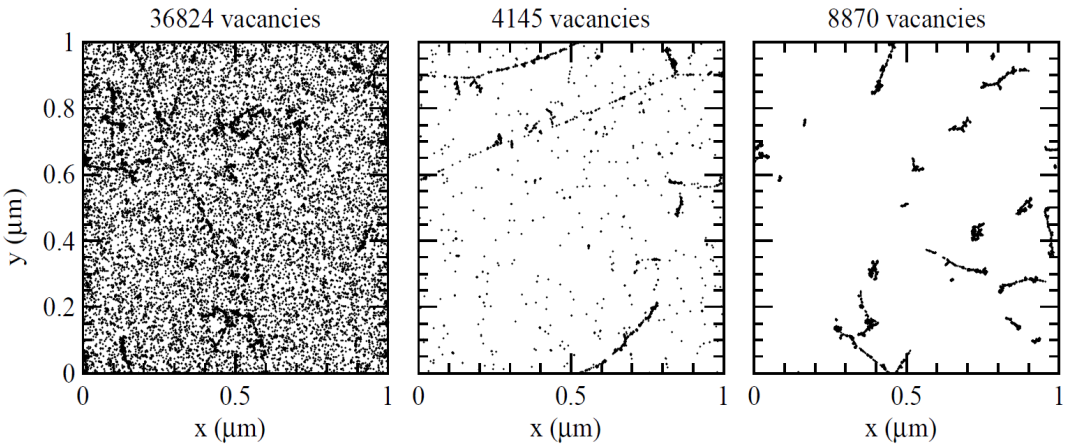

Figure 3.3: Distribution of vacancies created by 10 MeV protons on the left, 24 GeV protons in the middle and 1 MeV neutrons on the right, corresponding to a fluence of $1 \cdot 10^{14}\,\mathrm{cm}^{-2}$ and without annealing. The plots are projections over 1 μm out of 300 μm thick silicon bulk. Figure taken from [30].

3.3 Non-Ionizing-Energy-Loss (NIEL)

The NIEL is given by (taken from [31]):

$$NIEL(E) = \frac{N_A}{A} \sum_i \int_{E_{R,min}}^{E_{R,max}} Q(E_R) E_R \left(\frac{d\sigma(E)}{dE_R} \right)_i dE_R \tag{3.13}$$

with the Avogadro number N_A, the atomic mass of the primary knock on atom A_i, the partition factor $Q(E_R)$ that gives the fraction of energy E_R of the recoil atom to be lost in further displacements and the differential cross section $\frac{d\sigma(E)}{dE_R}$ for a particle to create a recoil atom.
The minimal energy is given by the displacement energy

$$E_{R,min} = E_d$$

which is not exactly known but believed to be about 20 eV.
The maximum energy can be assumed at the energy of the elastic scattering and is given by (taken from [31]):

$$E_{R,max} = 4\frac{m_p \cdot m_i}{(m_p + m_i)^2}E$$

with the mass of the particle (m_p) and of the recoil atom (m_i).
Using this relation, a displacement damage function is defined:

$$D(E) = NIEL(E) \times \frac{A}{N_A} \tag{3.14}$$

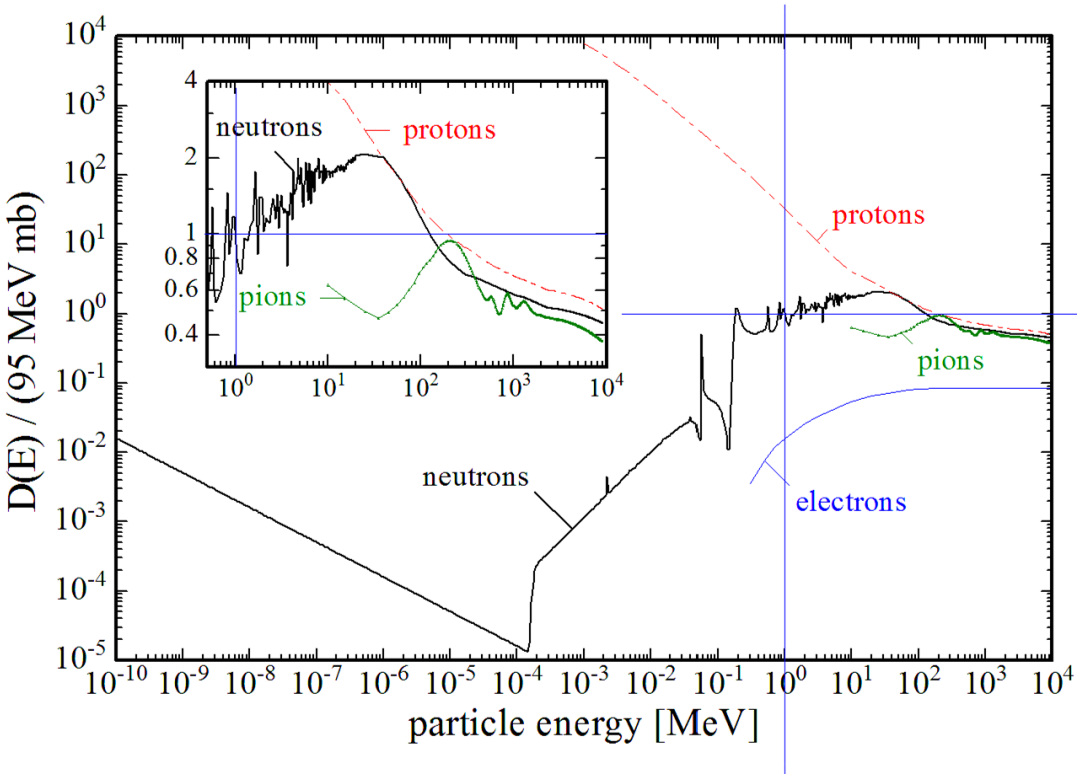

Figure 3.4: Damage function for different particles. Figure taken from [29], data based on a variety of sources.

3.3.1 NIEL scaling

Since the bulk damage due to NIEL is the main contribution to the degradation of the performance of silicon sensors in a hadron environment like the LHC, it would be desirable to be able to predict the damage. It was tried to describe the macroscopic damage (changes in dark

current and effective doping concentration) as proportional to the NIEL. The assumption is that the macroscopic damage is caused by a limited number of different defects, consisting of vacancies, interstitials, oxygen and carbon. The creation of vacancies and interstitials depends only on the NIEL but the formation of higher order defects depends on material characteristics (the availability of oxygen and carbon) and the number of defects close to each other. This means basically, that a proportionality factor depending on the particle energy is needed for every particle type. This factor can be derived from the damage function (see figure 3.4), taken from [32]:

$$\kappa_p = \frac{\int D(E)\phi(E)dE}{D_n(1MeV)\int \phi(E)dE} \tag{3.15}$$

with the hardness factor $\kappa_p(E)$, the particle fluence Φ_p with the energy spectrum $\phi(E)$ and the damage function $D(E)$. Using this concept the fluence is scaled to a so-called *1 MeV neutron equivalent fluence* Φ_{eq}.

$$\Phi_{eq} = \kappa_p \times \Phi_p(E) \tag{3.16}$$

3.4 Macroscopic properties

The created defects are only of interest if they influence the macroscopic properties defining the functionality of a sensor. The three important parameters are:

- Full depletion voltage, which is the nominal voltage needed to fully deplete the sensor of free charge carriers.
- Reverse current, which increases the noise and the power consumption and introduces free charge carriers, which can change the occupation of electrically active levels in the band gap.
- Charge collection, since it is only possible to collect charge of a limited time, charge that is trapped by defects is lost for the read out signal.

3.4.1 Depletion voltage

The full depletion voltage is defined as the voltage that is needed to deplete the silicon bulk of free charge carriers. This depends on the doping concentration through the sensor bulk and the thickness of the bulk.

Since it is difficult to measure the doping concentration through the thickness of a sensor, usually an effective doping concentration is used, that is proportional to the full depletion voltage via (taken from [32]):

$$|N_{eff}| = \frac{2\epsilon\epsilon_0\, V_{dep}}{q_0\, d^2} \tag{3.17}$$

with the effective doping concentration N_{eff}, the permittivity $\epsilon = 8.85 \cdot 10^{-12}$ F/m, the relative permittivity of silicon $\epsilon_0 = 11.7$, the elementary charge $q_0 = 1.6 \cdot 10^{-19}$ C and the depletion depth d.

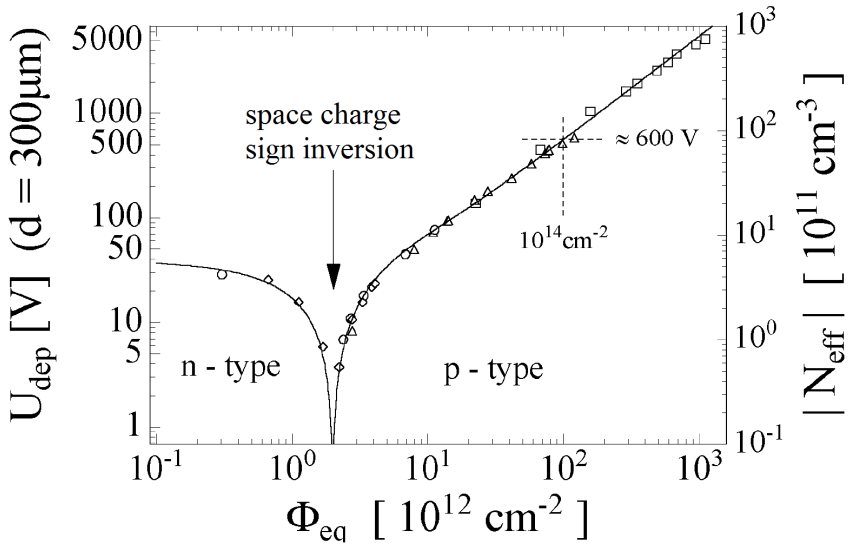

Figure 3.5: Development of the full depletion voltage with neutron irradiation for n-bulk silicon sensors. Figure taken from [32], based on data from [33].

For high fluences $> \mathcal{O}(10^{14})$ the full depletion of the silicon is not possible anymore, due to a high reverse current that increases the number of charge carriers. Moreover the electrical field is no longer growing from one side towards the other, but is present in the whole sensor from the beginning and then grows faster in some regions than in others. But it is still possible to find a saturation of capacitance, reverse current and charge collection. The doping concentration and therefore the full depletion voltage strongly depends on electrically active shallow levels in the band gap. Those are the initial dopants but also defects generated with the irradiation. Depending on initial doping, particle type, energy and fluence, the full depletion voltage can be reduced or increased.
The additional defects after irradiation can lead to a second high field region, the so-called double junction. If this second high field region turns out higher than the original one, the sensor underwent a space charge sign inversion (scsi). After such an scsi the full depletion voltage starts to rise again (see figure 3.5).

Annealing of the full depletion voltage

The full depletion voltage after irradiation changes with time, depending on the temperature. This is caused by the movement of defects (like interstitials or vacancies) through the silicon lattice. The combination of two initial defects forming a new one change the effective doping. For example, the electrical deactivation of dopants leads to an effective donor removal in n-bulk silicon. New dopants can be built by the formation of new defects. All of that changes the space charge in depleted regions and hence the full depletion voltage. Figure 3.6 shows the annealing of a n-bulk sensor after space charge sign inversion, which then has a similar behavior to a p-bulk sensor. In the first part (until about 80 minutes at 60 °C) the short term

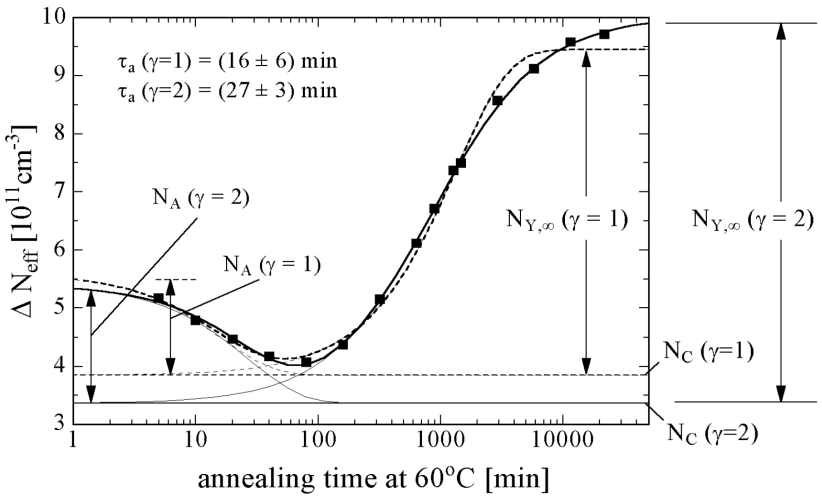

Figure 3.6: Development of the full depletion voltage with time for n-bulk silicon sensors after space charge sign inversion. It was found that the points can best be described by a second order process and hence the second order function with $\gamma = 2$ is used. Figure taken from [32].

annealing is dominant, in the second the long term annealing becomes dominant. The behavior can be described as (taken from [32]):

$$\Delta N_{eff}(\Phi_{eq}, t, T_a) = N_A(\Phi_{eq}, t, T_a) + N_C(\Phi_{eq}) + N_Y(\Phi_{eq}, t, T_a) \tag{3.18}$$

With the fluence Φ_{eq}, the annealing time t and the annealing temperature T_a. The three terms correspond to

- N_A: short term annealing, the part that is dominant in the first 80 minutes at 60 °C. It can be described by

$$N_A = \Phi_{eq} \cdot g_a \cdot exp\left(-\frac{t}{\tau_A(T_a)}\right) \tag{3.19}$$

  With the acceptor introduction rate g_a, the radiation induced acceptor concentration at $t = 0$, $\Phi_{eq} \cdot g_a$ and the annealing time constant $\tau_a(T)$.

- N_Y: long term annealing, the part that is dominant after the first 80 minutes at 60°C. It can be described by

$$N_Y = N_{Y,\infty}\left(1 - \frac{1}{1 + t/\tau_Y(T_a)}\right) \tag{3.20}$$

  With the reverse annealing amplitude $N_{Y,\infty} = g_y \cdot \Phi_{eq}$ and the annealing time constant $\tau_Y(T)$, where $\tau_Y(T) \gg \tau_a(T)$.

- N_C: stable damage, the part that is independent of annealing. It can be described by

$$N_C = N_{C0}(1 - exp(-c\Phi_{eq})) + g_c\Phi_e q \tag{3.21}$$

With the damage parameter N_{C0} (describing the final value of the "incomplete donor removal"), the donor removal constant c and the acceptor introduction rate g_c.

For more information see [32].

3.4.2 Reverse current

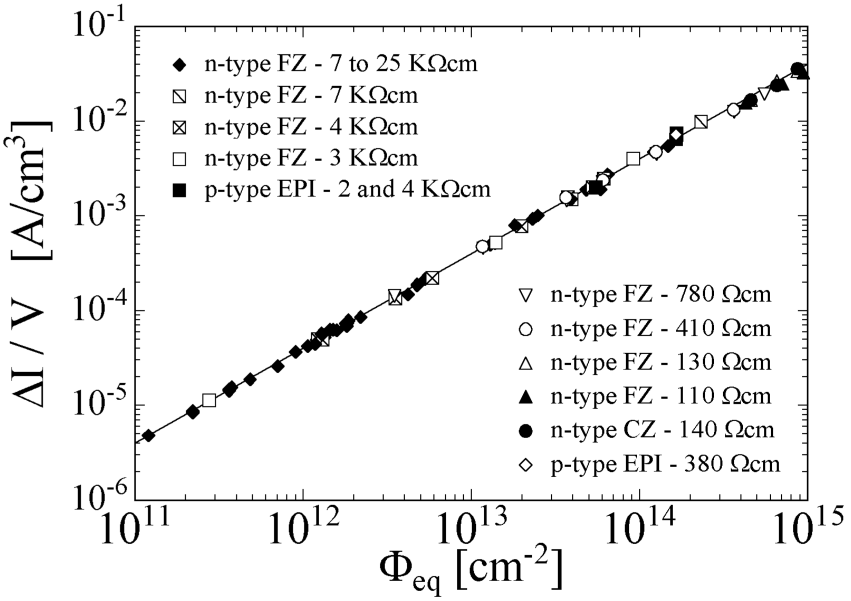

Figure 3.7: Development of the dark current with irradiation. Figure taken from [32].

As shown in 2.2.2, the reverse current depends strongly on the temperature. This means that the temperature should be controlled or at least measured to be able to correct for temperature effects. The change of the reverse current at full depletion voltage is directly proportional to the NIEL scaled fluence Φ_{eq} (See figure 3.7).

$$\Delta I(T) = \alpha(T) \cdot \Phi_{eq} \cdot V \tag{3.22}$$

With the current related damage rate α and the volume V. The temperature dependence is described by 2.9. In [29] it is shown that the change in dark current is independent of silicon material and bulk doping.

Annealing of the reverse current

The annealing behavior of the α parameter is shown in figure 3.8. Like the annealing of the full depletion voltage, it depends on the annealing temperature (T_a). The annealing can best be described by a parametrization using an exponential term for the short term annealing, a

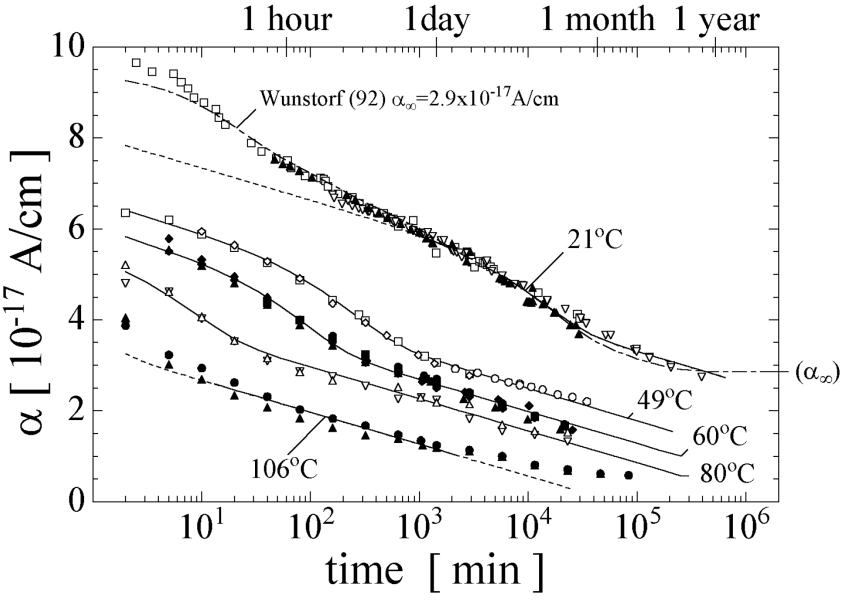

Figure 3.8: Development of the dark current with time. Figure taken from [29].

logarithmic term for the long term annealing and a constant (taken from [32]):

$$\alpha(t, T_a) = \alpha_I(T_a) \cdot exp\left(-\frac{t}{\tau_I(T_a)}\right) + \alpha_0(T_a) - \beta(T_a) \cdot ln(t) \tag{3.23}$$

For different temperatures the values of the parameters can be found in [29]. Equation 3.23 can be resolved to give a temperature scaling factor (taken from [29]):

$$\Theta(T_a) = exp\left(-\frac{E_I^*}{k_B}\left(\frac{1}{T_A} - \frac{1}{T_{ref}}\right)\right) \tag{3.24}$$

With the current annealing scaling factor $\Theta(T_a)$ between the two temperatures T_A and T_{ref}. The activation energy E_I^* is 1.30 ± 0.14 eV according to [29].

3.4.3 Charge collection

The charge collection efficiency of an irradiated sensor is < 1 due to trapping, with more trapping for higher fluences. T. Pöhlsen shows in his thesis [34] that the charge collection of a pad sensor is independent of the material, if the operation voltage is above the full depletion voltage and the sensor thickness is the same. Figure 3.9 shows the signal for different materials that were also investigated in this work. The bulk doping plays only a role via the full depletion voltage, as at high enough voltages no difference is visible. The thicker sensors show a higher signal above full depletion than the thin sensor for the lower fluences $\Phi_{eq} < 1.5 \cdot 10^{15}\,\mathrm{cm}^{-2}$.
In segmented sensors the charge collection can be different, especially if the sensor is not fully

Figure 3.9: Charge collection of pad sensors, calculated from the charge collection efficiency. E-h pairs are generated using infrared laser light. The shown sensors are irradiated with 23 GeV protons, the values are displayed at 600 V operation voltage. Figure taken from [34].

depleted.

Annealing of the charge collection

As described in 3.4.1 the full depletion voltage depends on the annealing time. For the signal as a function of voltage, a shift of the full depletion voltage with annealing time is also visible. For an increased V_{fd} higher voltages are needed to achieve the same signal heights. However, for $V \gg V_{fd}$ no dependence on annealing time has been observed in [34].

Measurement techniques for the understanding of sensor properties

4.1 Measurements of electrical characteristics

To measure the electrical properties of the silicon sensors that are described in 2.2.2, the following measurements are performed.

4.1.1 Current characteristics measurement

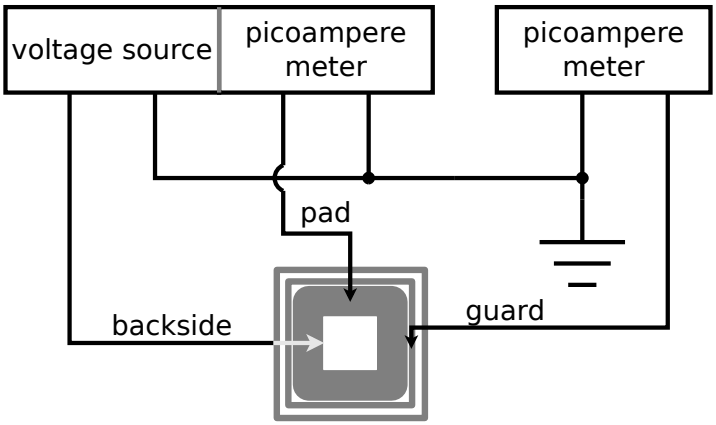

Figure 4.1: Connection layout for the current voltage characteristics measurement. The pad of the DUT is connected to ground through a picoampere meter. The voltage source is connected to the backside. The guard ring is connected to ground through another picoampere meter.

The connection layout for the measurement of a current-voltage characteristic is shown in figure 4.1.
The voltage source applies a bias voltage on the backside of the device under test (DUT). On the front side of the DUT, the implant is connected to ground through a picoampere meter via the aluminum contact. To separate edge effects from the pad volume, the guard ring can be connected to ground through another picoampere meter. Changing the bias voltage does not only lead to a changed dark current, but in the first seconds also to a charging current of the capacitances inside the circuit. To achieve a stable measurement and not endanger the DUT, the bias voltage is not applied abruptly and a short delay is introduced between applying a

new bias voltage and the start of the measurement.

4.1.2 Capacitance characteristics measurement

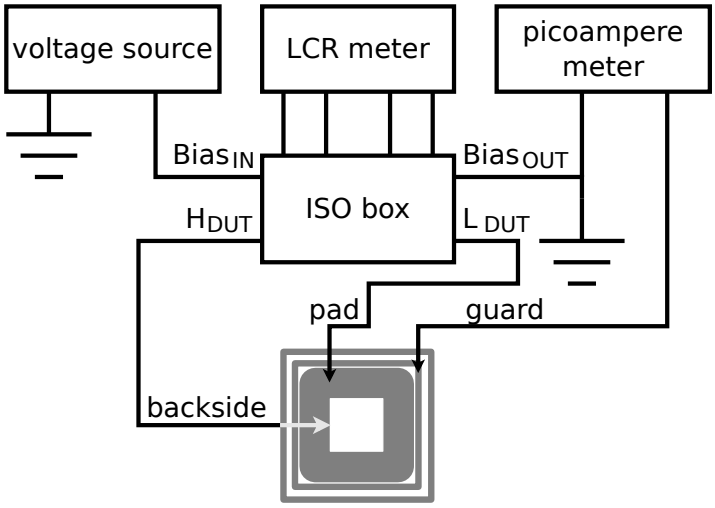

Figure 4.2: Connection layout for the capacitance voltage characteristics measurement. The LCR meter and the voltage source are connected to the ISO box, where the measurement signal is coupled to the bias voltage. The pad and backside of the DUT are connected to the ISO box (see figure 4.3). The guard ring is connected to ground through a picoampere meter.

The connection layout for the measurement of a capacitance voltage characteristic is shown in figure 4.2. The bias voltage is applied by the voltage source through the ISO box to the backside of the DUT. The connection from the pad of the DUT to the LCR meter is also routed through the ISO box. To constrain the active area, the guard ring can be connected to ground through a picoampere meter. A layout of the ISO box is shown in Figure 4.3. The purpose of the ISO box is to separate the high DC voltage bias circuit from the low voltage AC measurement circuit by inserting capacitors in the measurement circuit. Even with the decoupled voltage, the full current has to flow through the LCR meter on the L side to enable the LCR measurement. As described in section 4.1.1, the bias voltage should not be applied abruptly and a delay after applying a new bias voltage is inserted. The measurement principle of the LCR meter is shown in figure 4.4. The middle part (between the labeled connectors H_{CUR}, H_{POT}, L_{CUR} and L_{POT}) is replaced with the ISO box and the DUT. Through the H_{CUR} connection the AC measurement current is supplied. H_{POT} could be used to provide a bias voltage, but only up to 40V in the used device. On the right side, a virtual ground is created via L_{POT} by an operational amplifier. Together with the current that is measured flowing through L_{CUR}, the complex Impedance is determined. From that the resistance, inductance or capacitance can be calculated.

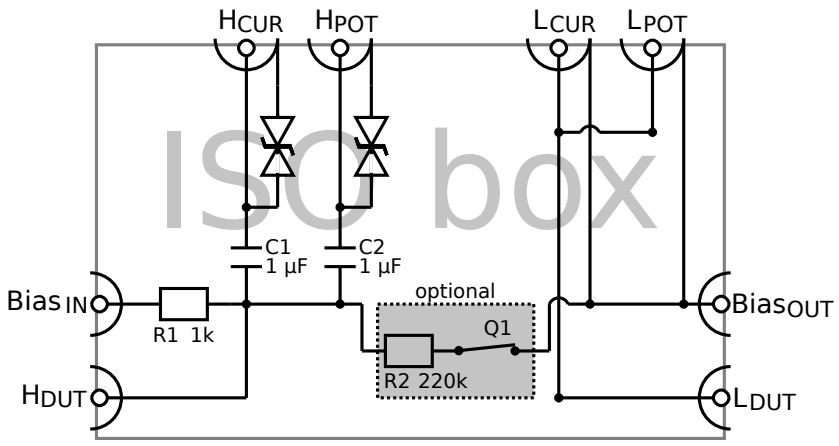

Figure 4.3: The ISO box is needed to couple the AC voltage from the LCR meter to the DC bias voltage. Therefore, the AC voltage is connected to the DUT through 1 μF capacitors (C1 and C2) and the DC voltage is connected through a 1 kΩ resistor (R1). The outputs of the LCR meter are protected against high voltage with transient voltage suppression diodes. The resistor R2 and the Relay Q1 can be used to discharge the capacitors C1 and C2 while not used for measurement.

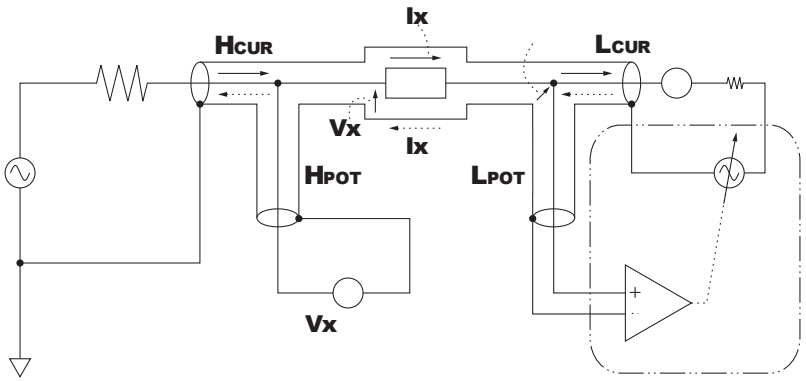

Figure 4.4: The measurement principle of the used LCR meter. An AC voltage is generated and sent through the output connectors H_{CUR} and H_{POT} to the DUT. On the other side, through L_{POT} a virtual ground is created using an operational amplifier and the current flowing through L_{CUR} is measured. The capacitance is then calculated using a simple model of the DUT. The capacitor is assumed to be either parallel with a resistor or serial. Figure taken from [35].

4.2 Transient Current Technique

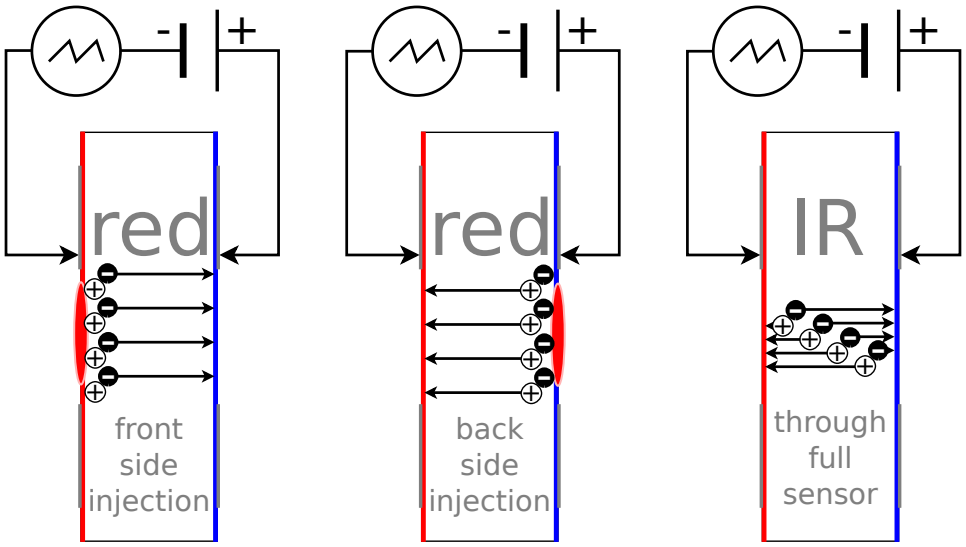

Figure 4.5: The measurement principle of the transient current technique. A DUT is readout by an oscilloscope while laser light induces charge either close to the surface or through the whole depth of the DUT, depending on the wavelength of the laser light. Figure redrawn after [34].

The Transient Current Technique (TCT) measures the time development of charge that is injected by a short laser pulse (see figure 4.5 and 4.6). The penetration depth of the laser light depends on the wavelength. The two standard wavelengths that were used are 670 nm (red) and 1065 nm (infrared). The penetration depth of the red light in silicon is of the order of 3μm and for the infrared of 1mm. That way the electron hole pairs can either be produced close to the surface only or throughout the whole depth of the DUT.
The time resolved signal can be used to estimate the electrical field inside the bulk of the DUT. If trapping can be neglected, the signal height is proportional to the electrical field and the time is proportional to the position along the sensor thickness. A high signal in the beginning of the pulse indicates a high electrical field at the side where the charge start to drift. A high signal at the end of the pulse indicates a high electrical field at the other side of the sensor. In the example figure 4.6 the space charge sign inversion can be seen, since the signal is higher towards the backside with respect to the front side. This indicates a change of the high field region from the frontside to the backside. To measure the charge collection efficiency the signal is integrated and compared to the signal of a non-irradiated DUT of the same material.
To read out the signal on the high voltage side with an applied bias voltage, a voltage source is coupled to the measurement circuit through a bias T. That way the high voltage is decoupled from the oscilloscope.

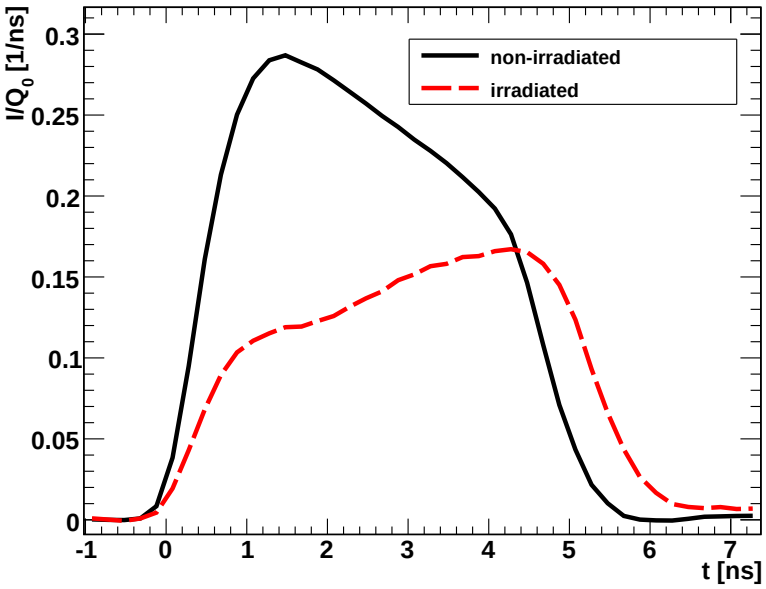

Figure 4.6: Typical TCT pulse of a non-irradiated (black line) and a irradiated dd-FZ300N pad sensor after space charge sign inversion (red, dashed line). The charge was induced with a red laser (672 nm). Figure taken from [36].

4.3 A silicon sensor β-test stand using the ALiBaVa readout system

Although it is important to understand the power consumption and the voltage that is needed to have a sensor fully active, the most important question for a detector in the HL-LHC environment is if it will still work efficiently at the end of the full run time with a given set of environmental parameters like temperature and voltage.
The best way to answer this question is to use test beams. But test beams are very time consuming and thus can only be used for a small set of samples.
To measure a larger set of samples this β-test stand is designed to mimic the running conditions of a silicon tracker in the lab. Therefore, it can apply the different environmental parameters like the ones used in CMS and measure the collected charge of (damaged) silicon strip sensors. Based on this, the efficiency at a given damage level for other readout chips can be estimated.
For the readout of the signals a commercially available system is used, the "Analogue Liverpool Barcelona Valencia readout system" ALiBaVa.

4.3.1 Basic layout

The β-test stand consists of two main parts:

- The control software of environment and measurement parameters including bias voltage, sensor temperature and source or laser position.

- The measurement system where the ALiBaVa system is used. For more information see [37].

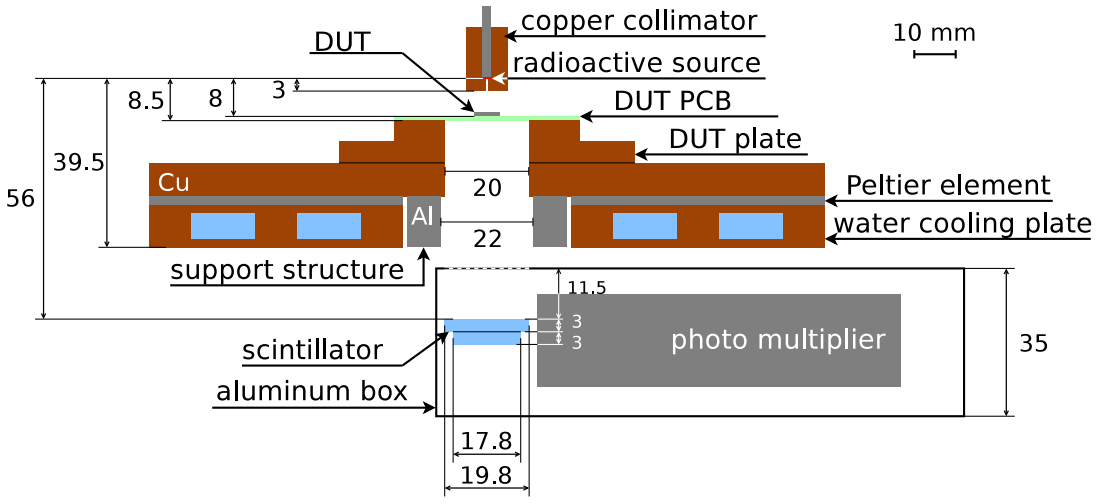

Figure 4.7: Cut through the β-test stand

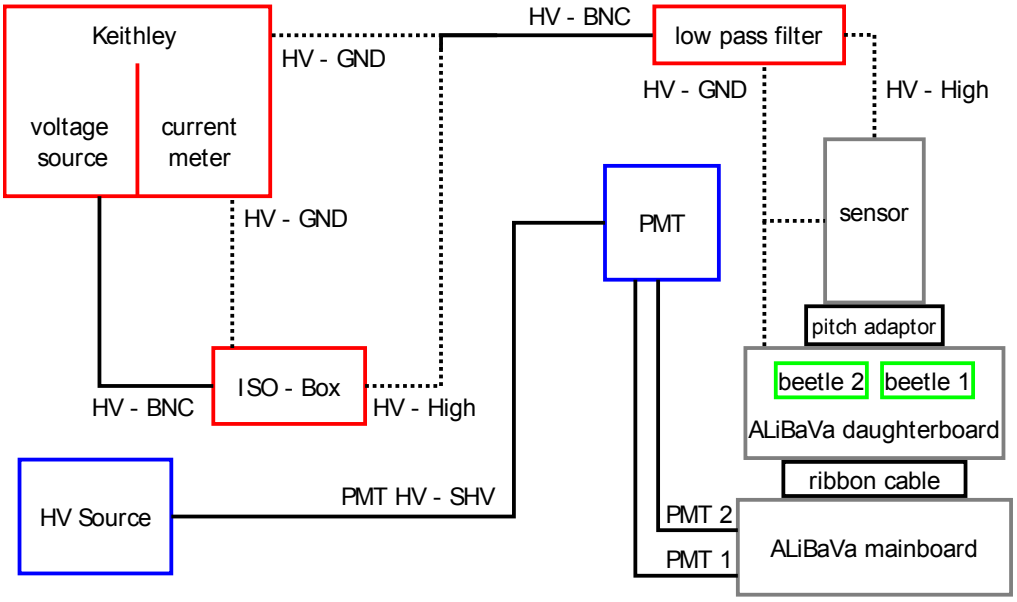

Figure 4.8: Electrical layout of the β-test stand. The bias voltage supply chain is shown in red, the trigger chain in blue and the data acquisition in gray. Dashed lines mean a single lead, solid lines mean the full cable.

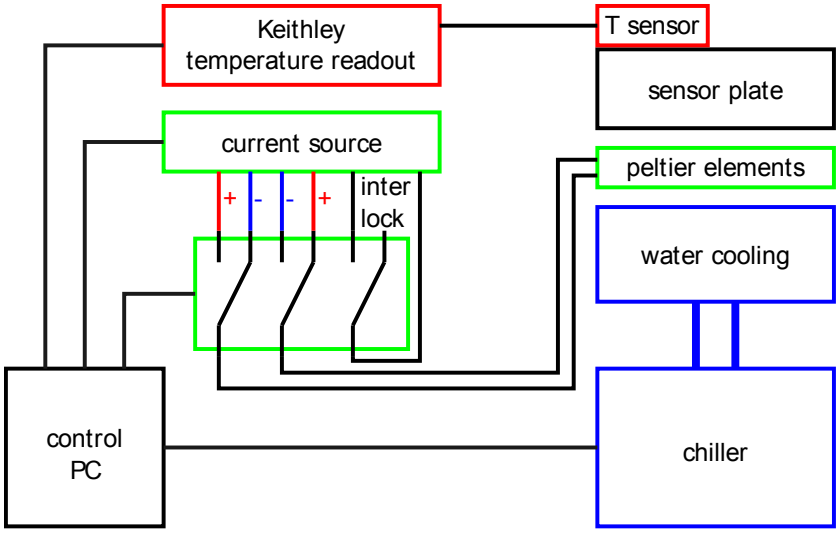

Figure 4.9: Electrical layout of the cooling system of the β test stand

In figure 4.7 shows a cut through the β-test stand. The source above the Device Under Test (DUT) generates β-particles flying through the sensor and the through hole in the cooling sys-

tem to the scintillator. To reduce the size of the spot where particles cross the sensor, 3 mm copper with a a hole of 0.7 mm diameter is used as a collimator. The particle looses energy in the scintillator and generates light, which is measured by the photo multiplier. The low energetic particles are stopped in the upper scintillator, the high energetic ones reach the second scintillator. To select only high energetic particles, a trigger signal is generated if both scintillators show a signal.
The measurement circuit including bias voltage supply, trigger chain and data acquisition is shown in figure 4.8. Special emphasis has to be put on the ribbon cable between the daughter board and the motherboard. It should be shielded with metal foil and as short as possible to minimize asymmetric crosstalk and noise.
The layout of the cooling system is shown in figure 4.9. Since the temperature of the DUT is the important one, the temperature sensor should be placed as near to the DUT as possible. The heat is then transferred from the DUT to a sink using peltier elements. This is very fast and can be easily controlled using a Proportional, Integral, Differential (PID) algorithm.

4.3.2 Beetle chip

The readout chip used by ALiBaVa is the beetle chip v1.5, developed for the tracker of the LHCb experiment.

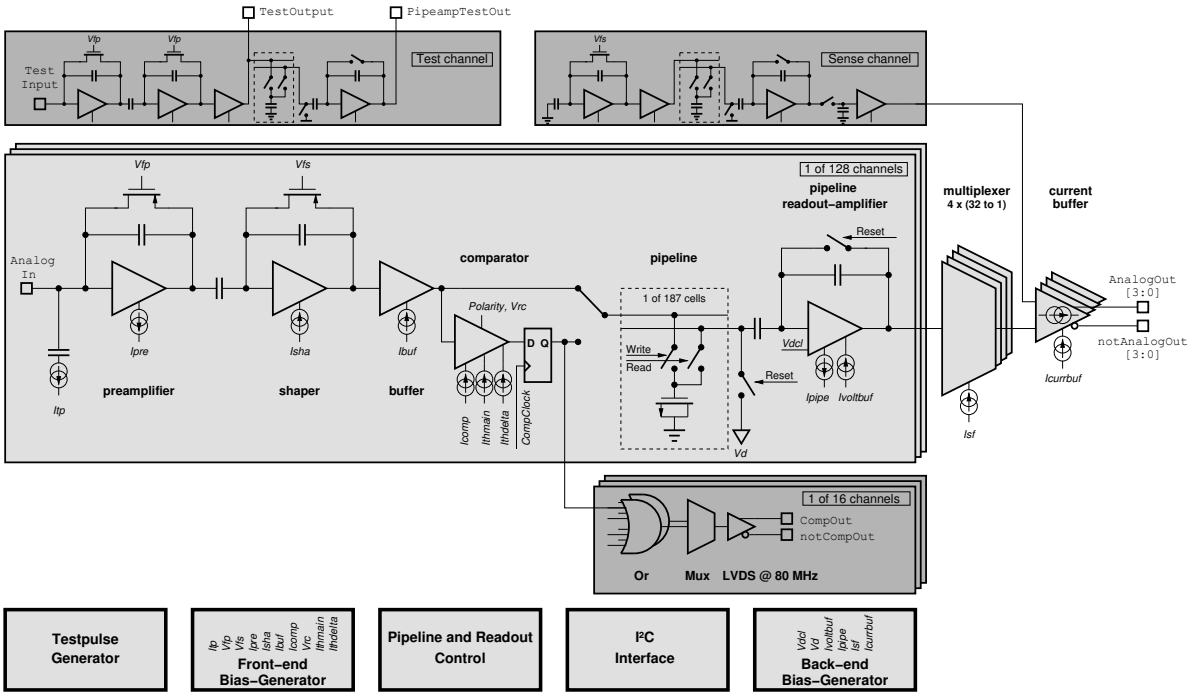

Figure 4.10: Block diagram of the beetle chip. Figure taken from [38].

A block diagram of the beetle chip is shown in figure 4.10. A signal coming from the sensor

is first amplified and shaped, then stored in a buffer. If a trigger requests this data it is shipped out as an analogue signal via a multiplexer. The digitization is done outside, in the case of ALiBaVa in the motherboard. That leads to a necessity of shielding the cable between daughter board and motherboard to reduce channel crosstalk and noise.

4.3.3 Pulse shape

Since the beetle chip is designed to work with a large variety of load capacitances (different strip length), several parameters of the pre-amplifier and the shaper can be adjusted to fit the used setup. One possible pulse-shape that is fast enough for the LHC running conditions is shown in figure 4.11. For more information see [38].

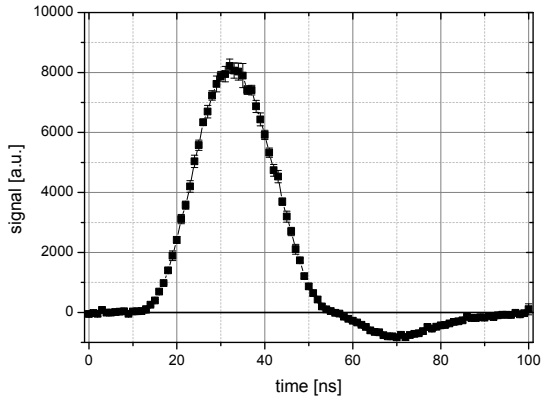

Figure 4.11: Beetle pulse shape with short peak region.

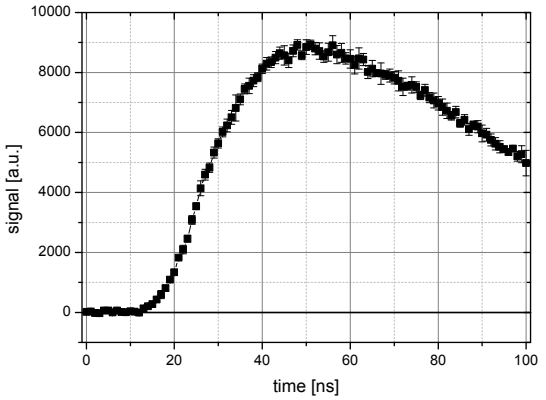

Figure 4.12: Beetle pulse shape with long peak region.

The problem of this pulse-shape is the very short peak region. In the case of ALiBaVa the particles are produced by a random β-decay instead of a synchronous collision in the LHC. That means that the particles and therefore the triggers are equally distributed over four consecutive time frames adding up to 100 ns, but only a time window of 5 to maximal 10 ns can be used, meaning that $90 - 95\%$ of the data has to be discarded.
To increase the amount of usable data, the parameters of the pre-amplifier and shaper can be changed to produce a longer peak region. A pulse-shape with a longer peak region and also increased signal to noise ratio is shown in figure 4.12. The only downside is a higher noise contribution of the dark current. That means that the signal to noise is worse than for the short pulse shape in the case of a high dark current.

4.3.4 Trigger selection

The scintillator system is designed in such a way that only high energetic particles of the ^{90}Sr spectrum (see figure 4.13) result in a trigger. This is important to mimic a so-called Minimum Ionizing Particle (MIP), which corresponds to a muon at a momentum of $P_\mu = 363.6$ MeV/c or

a $\beta\gamma = 3.44$ (see figure 2.5).
The β spectrum of ^{90}Sr decaying into ^{90}Y decaying into ^{90}Zr is shown in 4.13.

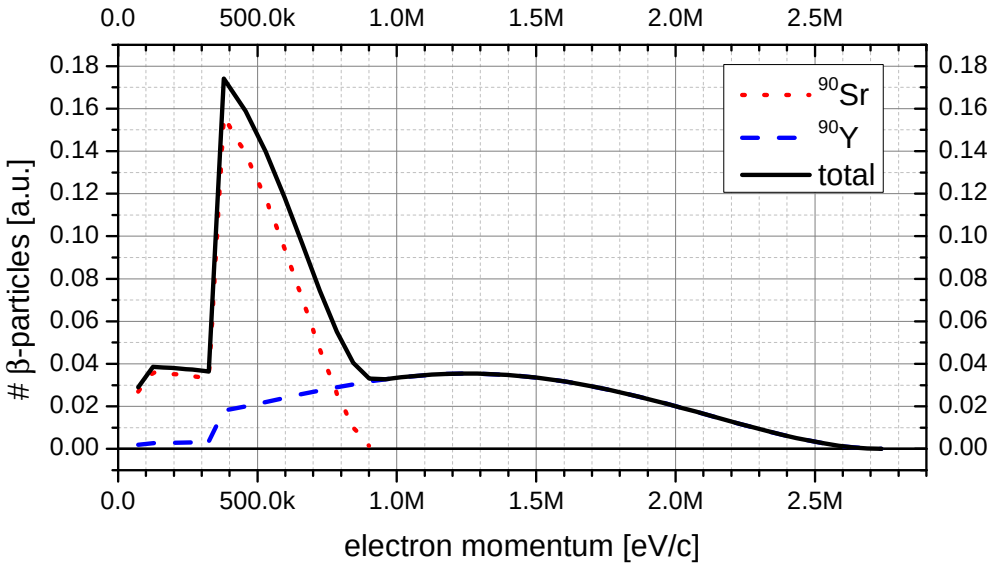

Figure 4.13: Strontium spectrum. For a typical encased ^{90}Sr source, the low energetic part is suppressed. (Data taken from [39])

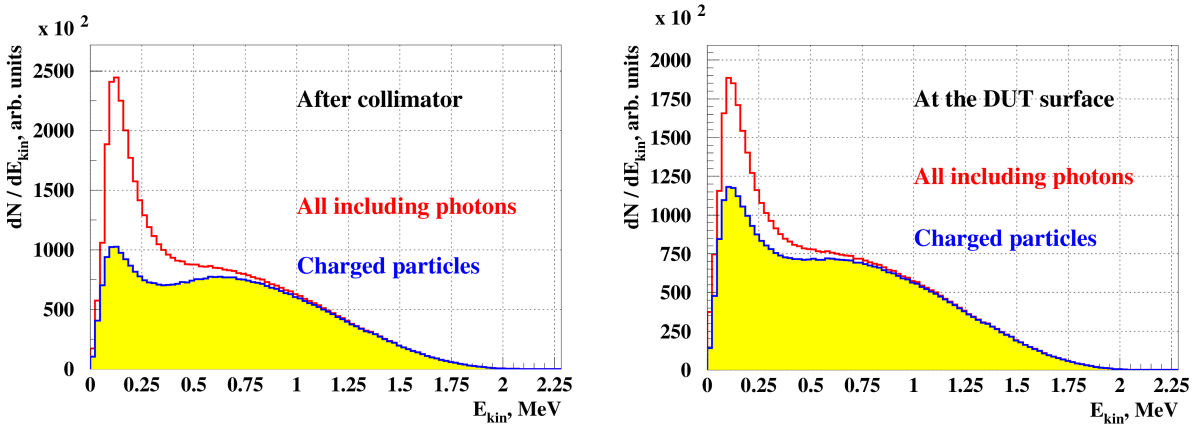

Figure 4.14: The simulated energy distribution of the particles leaving the collimator on the left and arriving at the surface of the DUT on the right. The red line shows the spectrum including the photons generated in the collimator, the blue line filled with yellow shows the spectrum of the charged particles only. The simulation was performed using GEANT3 by [40].

Using this β-spectrum and the stopping power of silicon shown in 2.5 it was estimated that the mean energy loss of β-particles in this system is $-1/\rho < dE/dx >= 1.54 \pm 0.05$ MeV

cm^2/g. Using this and the ionization energy given by [19] $E_i = 3.67\,eV$ per e-h pair, the mean energy deposition corresponds to a deposited charge of 19600 ± 450 electron hole pairs in 200 μm silicon. Using the factor between the mean and the MPV given by [26] to be 0.8, this corresponds to an MPV of 15700 ± 400 electron hole pairs.
In addition to the estimation of deposited charge above, a simulation was performed by Sergej

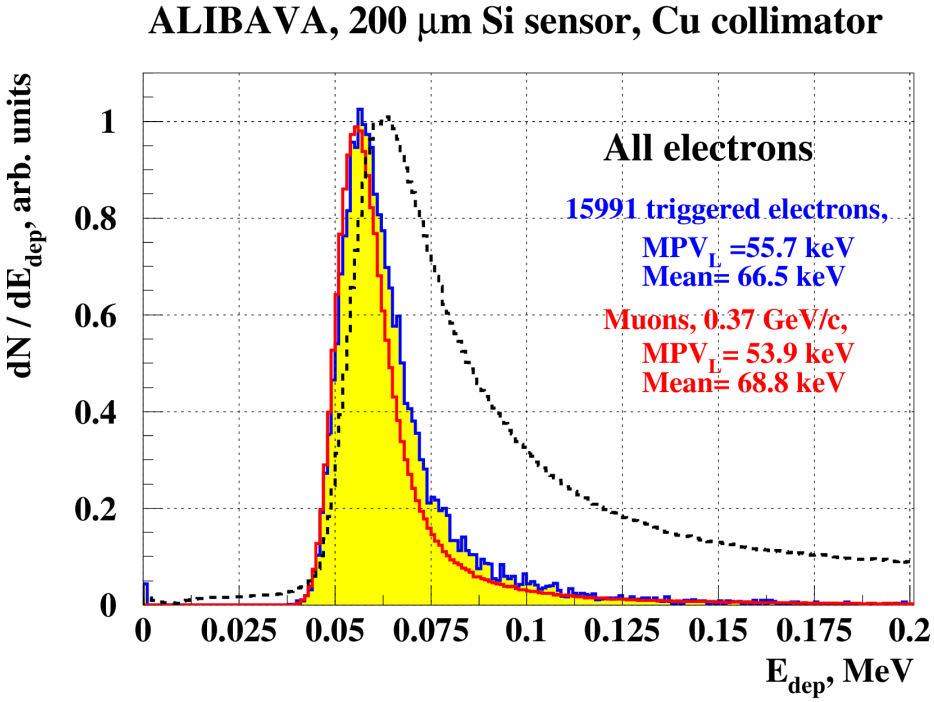

Figure 4.15: Deposited energy in 200 μm thick silicon of strontium β-particles. The dashed black line shows the energy deposition of all electrons, the blue filled histogram shows the energy deposited by the triggered electrons only and the red line shows the energy deposited of MIPs. The simulation was performed using GEANT3 by [40].

Schuwalow using the exact geometry of the used setup (see figure 4.15). The deposited energy of $55.69 \pm 0.09\,keV$ corresponds to 15175 ± 25 e-h pairs. Both results are not in perfect agreement, but still good enough to expect a collected charge of about 15250 e-h pairs for an undamaged sensor with a thickness of 200 μm.
The MPV of the deposited charge of a real MIP (a μ^- with a momentum of $P_\mu = 363.6\,MeV/c$) has been estimated to be 13700 ± 300 electron hole pairs using data from [19].
To ensure only high momentum electrons are selected, the trigger system consists of two separate plastic scintillators. The particles have to cross the upper scintillator to reach the lower one. As a result only those particles with a high enough energy produce a signal in both scintillators. The readout is performed with a four channel photo multiplier tube (PMT) from Hamamatsu Photonics. The output of the PMT is fed into the ALiBaVa daughter board and first discriminated with a level of -1 to 1V, adjustable in steps of 1mV. When the signals of both PMTs are

above the set threshold and are in a time coincidence, a trigger signal is generated. The trigger signal commands the beetle chip to ship out data and also starts a time to digital converter (TDC) to determine the time interval between the trigger signal and the internal clock.

4.3.5 Data analysis chain

Pedestals and common-mode noise

In figure 4.16 a raw event is shown, as measured by the ALiBaVa system. It can be divided in two regions. The unbonded region (channel 0 to 57 and 112 to 255) and the bonded region (channel 58 to 111). To improve the collected signal, four corrections are performed (in the given order):

1. Pedestal correction: In a separate measurement with random triggers (so that only the background is recorded) the mean of each channel over all recorded events is calculated. This value is subtracted for each channel and all events.

2. Polarity correction: To be able to use only one set of functions on n-type (p-type) sensors with positive (negative) signal, the polarity is corrected using the polarity of the bias voltage. The event with the applied corrections 1 and 2 is shown in figure 4.17.

3. Masking: If not all channels shall be used, the unused channels are set to 0 and marked as “not to use”.

4. Common mode correction:

   - The baseline of the remaining not masked channels can deviate from 0, due to noise that is picked up by all channels simultaneously. To correct the baseline it has to be made certain that no signal from a β-particle is included in the determination of the correction value. In a first step, the highest channel and one neighbor on each side as well as the lowest channel and one neighbor on each side are excluded.

   - In a second step all channels that deviated more than 3σ from the mean of remaing channels after step 1 are also excluded.

   - In the third step the mean of the remaining channels is calculated and subtracted from all channels.

The event with all corrections applied is shown in figure 4.18.

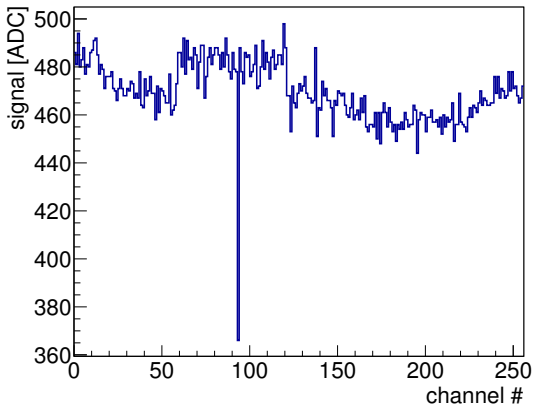

Figure 4.16: Single raw event. The next step is the pedestal correction that sets the baseline to 0 by subtracting the mean pedestal value for each channel. Also the signal polarity is inverted for negative bias voltages.

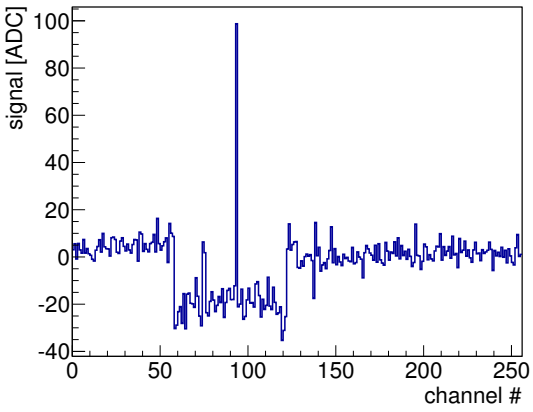

Figure 4.17: Single event after pedestal correction. The bonded region (strips 58 to 111) shows a common mode shift with respect to 0. A single strip hit occurred at strip 93.

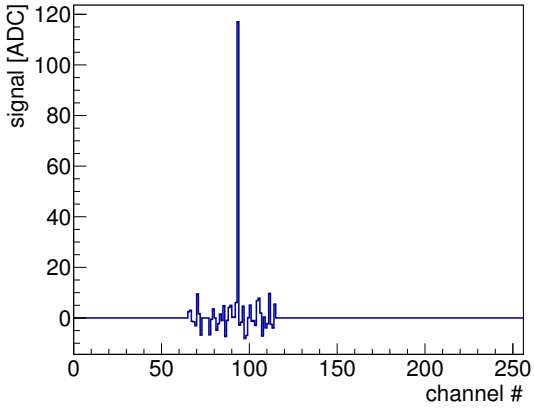

Figure 4.18: Single event after pedestal correction, common mode correction and masking of unused strips. The baseline is around 0.

Noise and crosstalk

The signal fluctuations after all corrections that are described in section 4.3.5 form the irreducible noise of this ALiBaVa system (see figure 4.18). It depends on the readout chip and its parameters but also on the connected sensor, mainly the capacitance and leakage current. The readout chip noise is given by [38] to be about $ENC \approx 540e^- + 50e^-/pF \cdot C_{in}$, with a slight variation for different beetle chip parameters.

A common noise distribution is shown in figure 4.19 as an example.

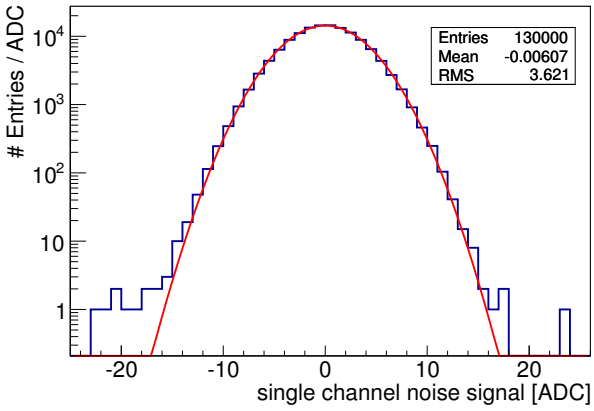

Figure 4.19: Distribution of all single channel signals of a random trigger run. It has a very gaussian behavior (red line), but still some deviation in the tails.

In addition an asymmetric cross talk can occur in the connection between the ALiBaVa daughter board and main board. During the submission of the analogue signals through the flat band cable, signals can couple to the neighboring channel, if no ground plane is present. The crosstalk is reduced by a metal foil which is glued on the flat band cable.

Signal calibration

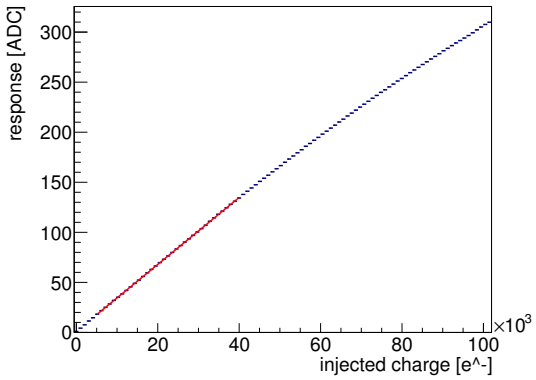

Figure 4.20: The profile of a single channel calibration measurement. Charge is injected on every channel, and the beetle chip reads out the signal. The slope of a linear fit from 5 to 30 ke^- is considered as gain.

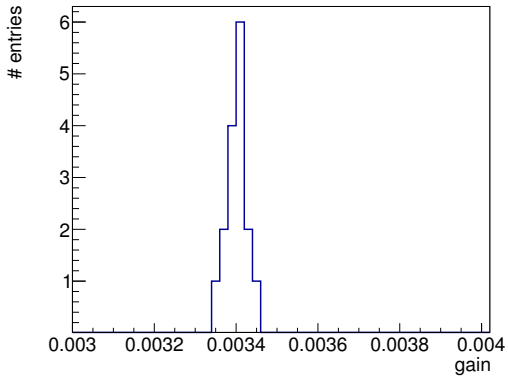

Figure 4.21: The single channel gains of the used channels in a histogram. It can clearly be seen that the gain is very similar for all active channels.

To convert the measured signal heights to a unit that is comparable with other measurements, the gain of the readout chip has to be measured. It is defined as the number of measured ADC counts per number of injected electrons. It depends strongly on:

- the parameter set of the readout chip,
- the temperature of the readout chip,
- the properties of the bonded sensor.

To determine the gain, a calibration measurement is performed. First a precise charge is induced in the input of the readout chip (I_{tp} in figure 4.10). After a delay that has to be chosen to give the maximum signal, the signal is read out.
This is repeated several times and the polarity is toggled for the channels and events. That way every channel is calibrated for negative and positive signals.
The mean and RMS of all signals of one channel and one amount of injected charge is displayed in a profile. Figure 4.20 shows an example. To get a gain value, a linear fit is performed in the region between 5 ke^- and 30 ke^-. The slope of this fit is taken as gain. Since the load of a connected sensor influences the gain, it has to be distinguished between the bonded channels and other regions.
All gains of used channels are shown in figure 4.21. For the measurements with one set of readout chip parameters, temperature and sensor properties as well as all corresponding gain measurements have been evaluated and only one gain value is used.

Cluster finding

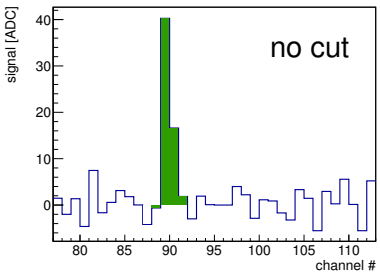

Figure 4.22: Event after pedestal and common mode corrections. The green marked strips form the cluster found by the "no cut" algorithm.

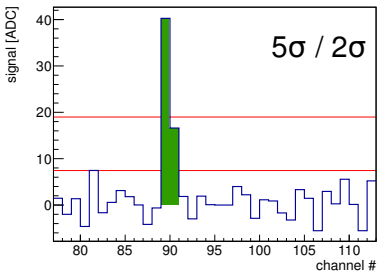

Figure 4.23: Event after pedestal and common mode corrections. The green marked strips form the cluster found by the "$5\sigma/2\sigma$ cut" algorithm. The upper red line marks the 5σ cut for the seed strip, the lower red line marks the 2σ neighbor strip cut in this case.

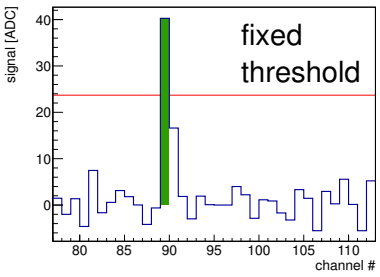

Figure 4.24: Event after pedestal and common mode corrections. The green marked strips form the cluster found by the "fixed threshold cut" algorithm. The red line marks the 1 fC cut for the strips.

To understand the charge collection in segmented sensors better, three different algorithms to find the deposited charge in each event are used. These algorithms are needed, because the charge often spreads over more than one strip, due to capacitive coupling of the charge, a tilted

angle of the particle creating the charge and diffusion. As a result, the channels that record the deposited charge vary from event to event.
In addition, the charge can be collected by a single channel or spread over two or more. In the following, the channel with the highest signal is called the "seed". Channels next to the seed are called neighbors and a group of the seed and neighboring channels is called "cluster".
The first step for all algorithms is to search for the highest signal in the event and take it as seed. If the seed is within two channels of a masked channel it is possible to have part of the cluster charge in the masked channel. To prevent this, such an event is excluded.

no cuts The main part of this algorithm is to add a predefined number of neighbors (eg. one or two) on each side of the seed (see figure 4.22) to form a cluster, independent of the charge in neighbors.
The plus of this algorithm is that it can give an accurate signal height distribution even if it is below the cuts of the other two algorithms.
The downside of this algorithm is that events that have no signal still contribute to the later analysis. Those events are caused by a β-particle arriving in the scintillators and creating a trigger without passing through the active region of the sensor. Their number can be reduced by carefully choosing the position of the ^{90}Sr source, but can often not be avoided completely. To reduce their influence, a correction method is applied.
From high bias voltage measurements the number of events that have no signal can be estimated. Their distribution can also be estimated from the high bias voltage measurements or by analyzing the events assuming a reversed polarity. Found clusters are excluded, if they correspond in signal height to the estimated distribution of no signal events, as long as the number of excluded clusters is lower than the estimated number of clusters to exclude.
This algorithm gives a minimally biased signal height distribution over a very large range. It is also best suited for comparison of charge collection measurements on pad sensors and segmented sensors.

$5\sigma/2\sigma$ **cut** First, the seed is compared to the single channel noise. Only if the seed signal is higher than five times the noise σ of the corresponding channel, it is accepted as seed.
Second, the neighbors on each side are added, until the signal height drops below two times the noise σ of the corresponding channel or it is masked.
Third, the cluster is accepted if it either consists of at least two channels or the seed signal is six times higher than the average noise σ of active channels.
Figure 4.23 shows an event with a cluster found by this algorithm. This algorithm can work without prior knowledge of the number of particles recorded and is very similar to what is used in the current CMS tracker. Results obtained by this algorithm can be compared with other measurements, since it is widely used.

fixed threshold cut The fixed threshold cut algorithm checks if the signal height of the seed exceeds 6250 electrons (1fC). This is a possible threshold of the CMS binary chip that will be used as readout chip in the CMS phase II tracker. If so, the neighbors are also compared to this fixed threshold. If they exceed it they will be added to the cluster. Figure 4.24 shows an

event with a cluster found by this algorithm. The signal height distributions of this algorithm show typically a smaller most probable value (MPV) than the ones found with one of the other algorithms, since it ignores neighboring channels if their charge is below the threshold. But it is important to understand how the sensors will perform in the CMS phase II tracker with a binary readout.

Extraction of the collected charge

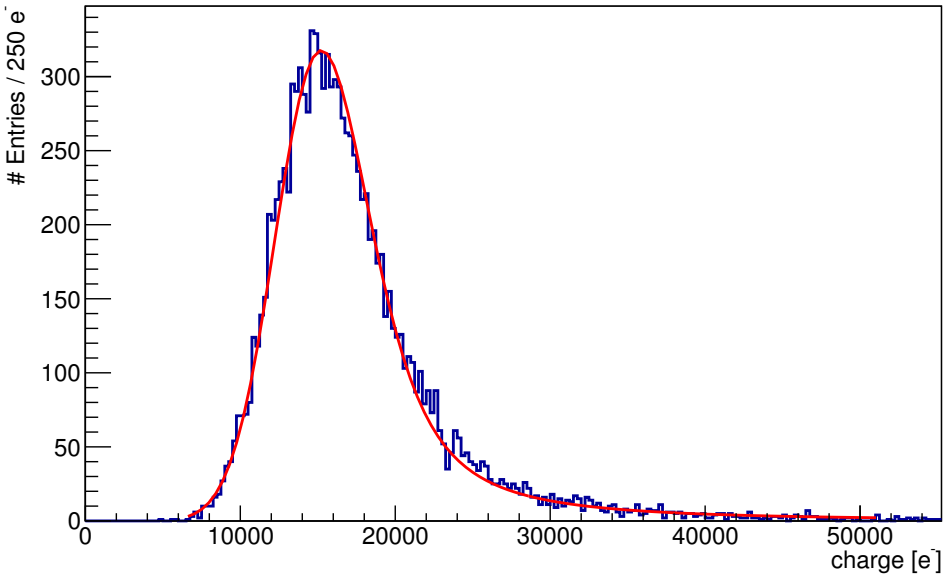

Figure 4.25: Signal heights distribution of β-particles from a ^{90}Sr source in 200μm thick silicon with fit of the landau distribution convoluted with the gauss distribution using the no cuts algorithm.

The charge of the clusters found by one of the algorithms described in section 4.3.5 is filled in a histogram. A typical histogram of a non-irradiated sensor filled using the “nocut” algorithm is shown in figure 4.25. To extract the ”Most Probable Value” (MPV) a fit is needed.
Landau developed the Landau distribution to fit the distribution of charge deposited by MIPs in thick absorbers. It is discussed by [41] that Landau neglects effects that lead to a broader distribution. In addition, there is a typically gaussian noise contribution that increases the broadening of the distribution. The easiest way to account for that with an adequate precision is to use a convolution of a gaussian and a landau distribution. A fit of such a convolution to data is shown by the red line in figure 4.25.
For further analysis the MPV value gained by this fit is used.

A measurement campaign to find the best silicon sensor material for the CMS tracker upgrade

The goal of this campaign is to find the best suited material and layout parameters for the coming phase II upgrade of the silicon tracker of the CMS detector. in order to achieve this goal a large variety of materials and test-structures were produced and tested.
To mimic the damage level of the silicon sensors after the full HL-LHC runtime the structures have been irradiated in three different facilities.

5.1 Materials

For the measurement campaign a large number of wafers have been produced by Hamamatsu Photonics (HPK) from a variety of materials with different dopings and production procedures.

5.1.1 Fabrication processes

The wafers have been produced using two main production technologies, the magnetic Czochralski method and the floating-zone method. For details see section 2.3. In table 5.1 the materials with their nominal thickness and their mean oxygen content are given. The measured oxygen profile is shown in figure 5.1. The thicknesses calculated from C/V measurements that were used for further calculations are given in table 5.2.

Material type	Short material name	Physical thickness [µm]	Nominal active thickness [µm]	Mean oxygen content [$10^{17}/cm^3$]
Deep diffused floating zone	dd-FZ220	320	220	3
Deep diffused floating zone	dd-FZ300	320	300	1
Thinned floating zone	FZ200	200	200	1
Magnetic Czochralski	MCZ200	200	200	4

Table 5.1: Wafer materials.

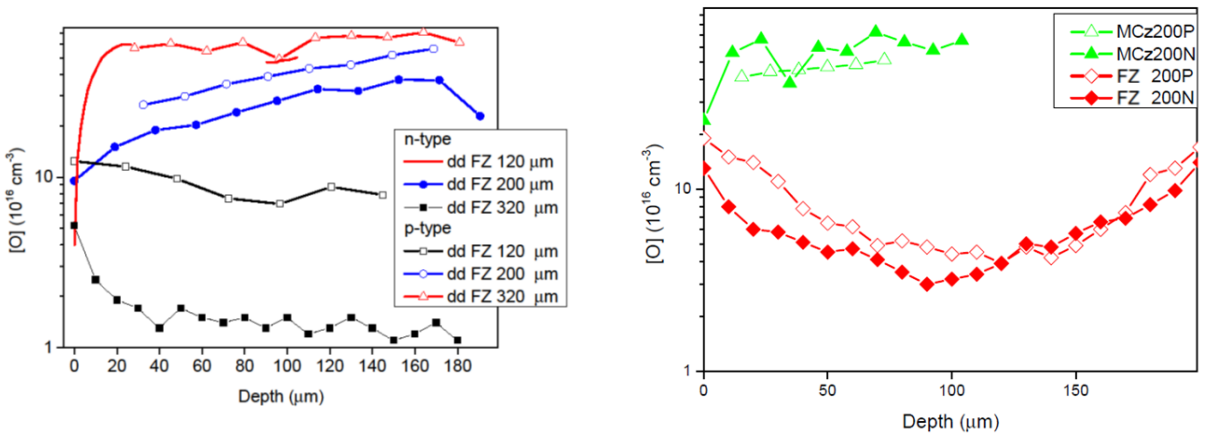

(a) dd-FZ materials

(b) FZ and MCz materials

Figure 5.1: Profile of the oxide concentration for the relevant materials. The secondary ion mass spectrometry (SIMS) measurements were performed by Adam Barcz from ITE [42].

Deep diffusion

The dd-FZ300 materials undergo the deep diffusion procedure only for a short time, resulting in a deep-diffusion thickness of 20 μm.
The dd-FZ220 materials undergo the deep diffusion procedure for a longer time, resulting in a deep-diffusion thickness of 100 μm.
The resulting rise of conductivity towards the back side is not as steep as for materials with standard backside implantation. In addition, more impurities and defects are introduced and a higher oxygen content of the dd-FZ220 is found, compared to the other floating-zone materials. For more details see [27]. Also the dd-FZ300 and the FZ200 have a higher oxygen content than standard floating-zone materials. It is similar to diffusion oxygenated floating-zone material (DOFZ) that was studied in the RD48 collaboration. For more details see [43].

5.1.2 Bulk doping

Wafers with n and p bulk doping have been produced. The sensors need then p^+ (n^+) implants with electron (hole) readout, on n (p) bulk material, to form a p-n junction. A problem that occurs in p bulk sensors with SiO_2 isolation is the accumulation layer. The SiO_2 isolation is charged positively and attracts electrons. The electrons are accumulated below the surface and form a conductive layer between the strips. To interrupt this layer two technologies are tested:

- **p-stop**: small p^+ wells surrounding the strips are implanted (see figure 5.4).
- **p-spray**: a homogeneous layer of p doping is introduced on the whole wafer surface.

To distinguish between the bulk doping and the surface isolation technology, the material name gets a suffix. For example, the FZ200 material becomes:

Short material name	Measured thickness
FZ200N	$202.2 \pm .6$
FZ200P	$205.1 \pm .4$
FZ200Y	$200.6 \pm 2.$
dd-FZ220N	$223.5 \pm 1.$
dd-FZ220P	$208.5 \pm 2.$
dd-FZ220Y	$209.3 \pm .8$
dd-FZ300N	$301.9 \pm 2.$
dd-FZ300P	$282.3 \pm 4.$
dd-FZ300Y	$285.3 \pm 2.$
MCZ200N	$197.2 \pm 1.$
MCZ200P	$199.4 \pm 2.$
MCZ200Y	$197.7 \pm 1.$

Table 5.2: Wafer thicknesses calculated from C/V measurements.

- FZ200**N**: n bulk material
- FZ200**P**: p bulk material with p-stop isolation
- FZ200**Y**: p bulk material with p-spray isolation

5.1.3 Structures

Wafer layout

To test different parameters of the materials and different sensor geometries, a wafer layout with several structures was designed in the campaign.
The main purpose is to find a suitable material for strip and pixel trackers. So important structures to produce are strip and pixel sensors. In addition to "standard" strip and pixel sensors, several special purpose structures have been produced. These include structures with different layouts to optimize the structure geometry, production test structures and the most simple fully functional particle detector layout, a pad diode sensor.
Figure 5.2 shows a view of the whole wafer, table 5.3 gives short information for all devices.

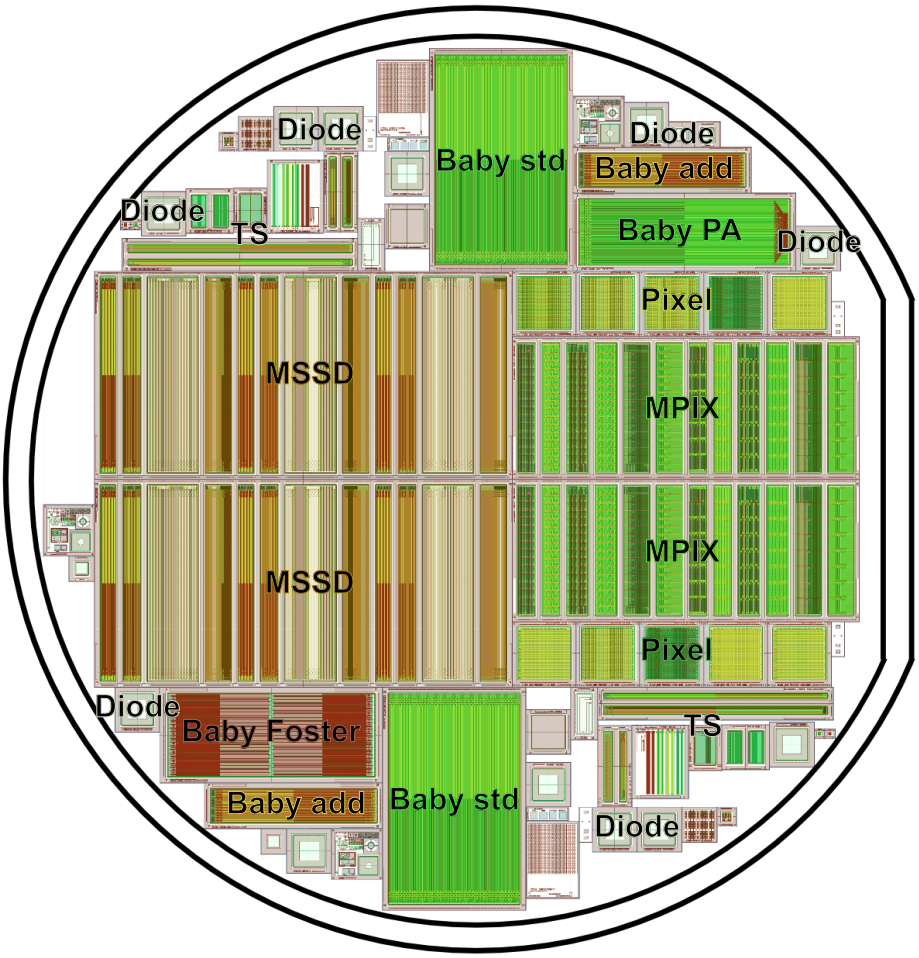

Figure 5.2: Picture of the wafer layout. The different structures shown are described in table 5.3. Figure created using the common layout file.

Structure name	structure type	description
Baby add	strip sensor	small standard layout strip sensor
Baby Foster	strip sensor	new layout strip sensor with four strips along the sensor
Baby PA	strip sensor	strip sensor with an integrated Pitch Adapter
Baby std	strip sensor	standard layout strip sensor
Diode	pad sensor	unsegmented pad sensor
MPix	pixel sensor	multi layout pixel sensor
MSSD	strip sensor	multi layout strip sensor
Pixel	pixel sensor	standard layout pixel sensor
TS	test structure	process test structure with multiple substructures

Table 5.3: Structures on the wafer shown in figure 5.2.

Standard strip sensors

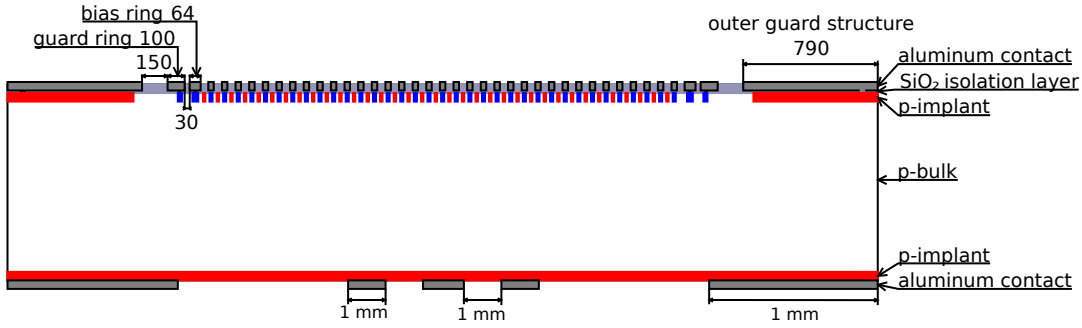

Figure 5.3: Baby strip sensor layout. The shown sensor is built with a n^+ implant in a p bulk with p-stop isolation. The surrounding outer guard structure shields the inner part from the influence of crystal damage at the cut line. The guard ring increases the breakdown voltage. The bias ring is connected to ground, the backside to the operating voltage. The strip layout is shown in figure 5.4. All numbers are given in µm. Figure not to scale.

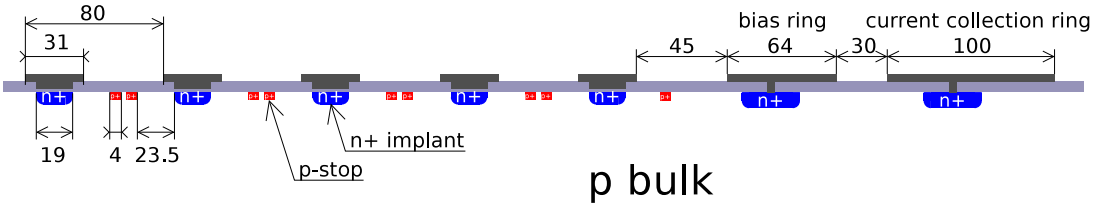

Figure 5.4: Baby strip sensor strip layout. The shown sensor is built with a n^+ implant in a p bulk with p-stop isolation. The metal contact is connected to the readout chip. The charge is collected by the implant. The signal is coupled via a capacitance to the metal readout strip. For p-bulk sensors the surface must be isolated. In the case of p-stop isolation this is achieved by implanting small p^+ wells on the surface of the bulk between the n^+ readout implants. All numbers are given in µm. Figure not to scale.

The standard strip sensors are used to measure the properties of segmented strip sensors after irradiation. The Baby std and Baby add sensors are designed with similar parameters as the sensors currently used in the CMS tracker.
As shown in figure 5.3 and 5.5, the strips are surrounded by three structures. The innermost one is the bias ring. The operating voltage is applied between the aluminum contacts on the backside and the bias ring. The strip implants are connected to the bias ring via polycrystalline silicon meanders that result in a few MΩ bias resistances. The second surrounding structure is the guard ring that is on a floating potential to reduce the potential difference towards the outer structure. The outer guard structure shields current generating defects at the cutting

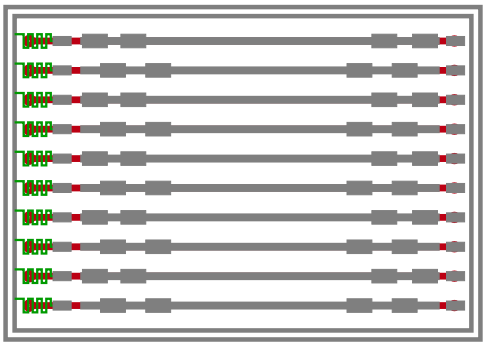

Figure 5.5: Baby strip sensor sketch. The surrounding rings are the guard ring (outer) and bias ring (inner). The guard ring increases the breakdown voltage. The bias ring is connected to ground and via bias resistors (shown in green) to the readout implants (shown in red). Through that connection the dark current and signal charge is transported off the implant. The signal is read out through the metal (shown in gray) that is placed on top of the implant. For the signal readout two contact pads (AC pads) are placed on each side of the strips. For testing purposes, one contact pad (DC pad) connected to the implant is also placed on each side. Figure not to scale.

edge. These defects are created by damaging the silicon lattice by cutting of the wafer into single structures with a diamond saw. Therefore a non-depleted zone is created in the cutting region by implanting with the same polarity as the bulk (see "outer guard structure" in figure 5.3). That way the high potential is also applied to the metal of the outer guard structure and the potential drops towards the guard and bias ring.
A detailed view of the strips is shown in figure 5.4. The strips have a pitch (the cell width) of 80 µm, an implant width of 18 µm and a readout metal width of 31 µm. That means that the metal is by 6.5 µm wider than the implant on each side. This is called metal overhang and should improve the electrical field near the strips and thus increase the breakdown voltage.
The strip sensor shown is the "p-stop" type. The "p-spray" type has a homogeneous p doping on the surface, instead of the implanted p-stops. The "n" type has reversed p and n dopings and no surface isolation.

Pad sensors

A pad sensor (as shown in figure 5.6) is the most simple fully functional silicon particle sensor. The outer structures are similar to those of the strip sensors. The outermost structure shields the inner volume from the influence of crystal damage due to the cutting edge. The next structure, the guard ring, is mostly used as a current collection ring. This means that it is connected to ground separately from the inner main structure. That way the volume that contributes to the capacitance, current or signal that is measured with the inner structure is well defined.
The inner structure consists only of one large implant, directly connected to an aluminum contact. The aluminum has a hole in the middle to allow a laser to generate a signal inside the sensor. The backside aluminum contact is produced as a grid to enable the signal deposition

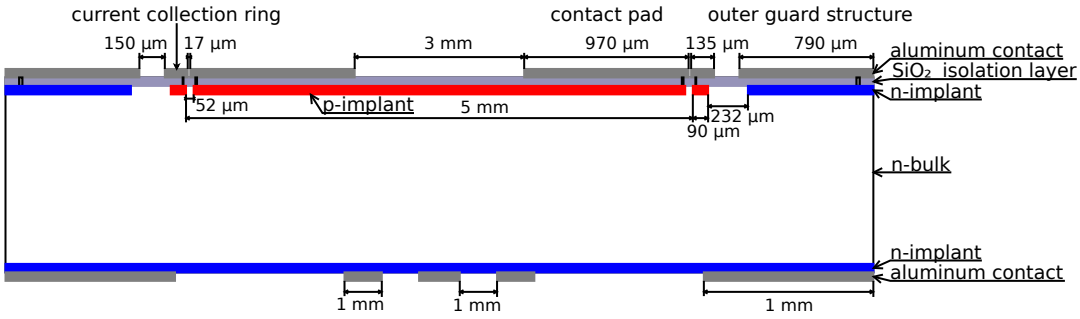

Figure 5.6: Pad diode sensor. Figure not to scale.

with lasers from the backside.
The simple geometrical layout makes it easier to understand the influence of the radiation damage to the bulk material, independently of surface effects that play a role in segmented sensors.

5.2 Irradiations

To test the different operation parameters of the test structures at the expected damage level after the full HL-LHC run time, the samples are irradiated at different facilities. Figure 5.7 shows the expected fluence at two different cuts through the CMS tracker. In table 5.4 the fluences used in this work are shown.
This plot, however, only shows the rough differentiation in neutral and charge hadrons. Figures 5.8 and 5.9 show the spectrum of the different energies for neutrons, protons and charged pions.

Radius cm	Proton fluence [1E14/cm^3]	Neutron fluence [1E14/cm^3]	total fluence [1E14/cm^3]
40	3	4	7
20	10	5	15
15	15	6	21
10	30	7	37

Table 5.4: Fluences used in the campaign

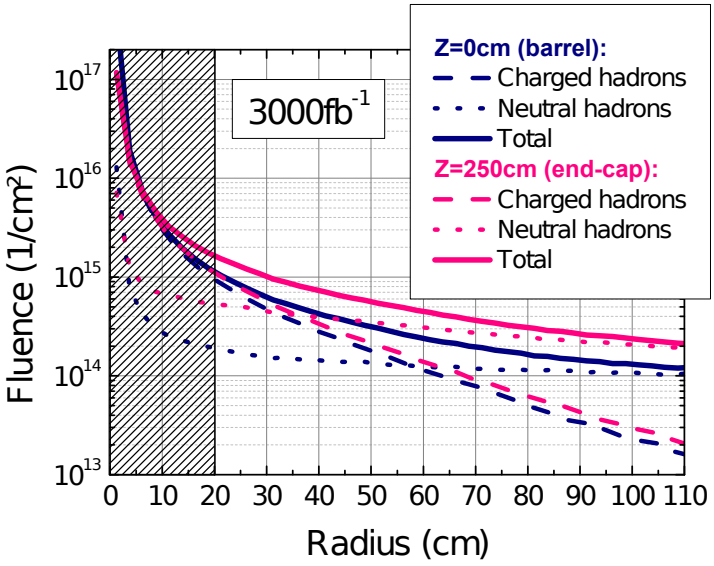

Figure 5.7: Expected total fluence after the HL-LHC run. The blue lines show a cut in the center, the pink lines in the end cap. The dashed lines show the contribution of charge hadrons, the dotted line of neutrons and the solid line shows the total fluence. The volume below a radius of 20 cm is expected to be equipped with pixel sensors, the volume above with strip or short strip sensors. Figure taken from [44], created by [45].

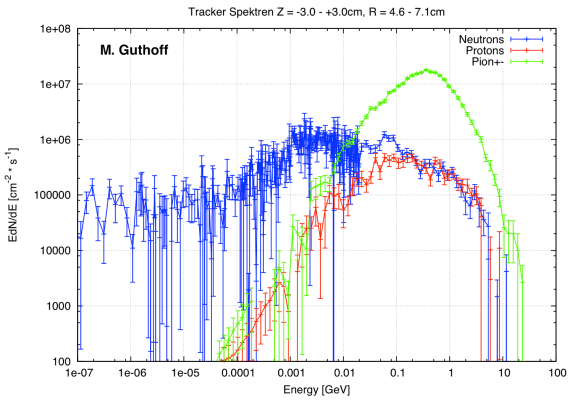

Figure 5.8: Spectrum of the hadron flux in the inner central region at about r≈ 6 cm from the interaction point. The blue line shows the contribution of neutrons, red of protons and green of charged pions. Figure taken from [45].

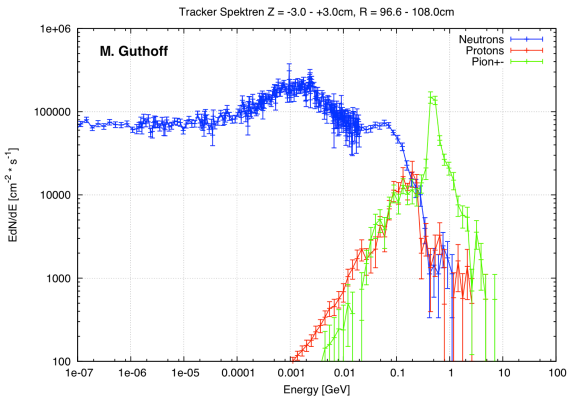

Figure 5.9: Spectrum of the hadron flux in the outer central region at about r≈ 1 m from the interaction point. The blue line shows the contribution of neutrons, red of protons and green of charged pions. Figure taken from [45].

To mimic the expected damage as precise as possible, three different irradiation facilities were used:

- **TRIGA reactor at JSI in Ljubljana:** The spectrum of the neutron facility is shown in figure 5.10. The spectrum is similar to the neutron spectrum expected at CMS. Since the main damage contribution comes from the neutrons with higher energies and the spectrum has a peak at ∼1 MeV, this neutron irradiation is referenced as **1 MeV neutrons** or **n**. For irradiation the samples are inserted in the core of the reactor. The fluence is determined by the reactor power and the time of the sample inside the reactor. The uncertainty is estimated as ≈ 10%. The temperature depends on the power by which the reactor runs and lies between room temperature and 40 °C for our irradiations. Since the irradiation takes only a few minutes, annealing is small compared to 10 minutes at 60 °C. For more information see [46].

- **PS at CERN in Geneva:** 1 to 3 spills of 23 GeV protons of the PS-beam are used to irradiate the samples and is referenced as **23 GeV protons** or $\mathbf{p}_G$. Since the proton flux varies with time, the flux is monitored online and for a more exact fluence measurement aluminum foils are irradiated in addition. The creation and decay of ^{24}Na or ^{22}Na is used to measure the fluence. The resulting uncertainty on the flux from the dosimetry of the aluminum samples is in the order of 7 to 8 %. Since the irradiation is performed in a non-cooled area and takes for several hours up to several weeks (depending on the targeted fluence), annealing during irradiation has to be taken into account as discussed in section 5.3. For more information about the PS irradiation facility see [47].

- **Cyclotron at KIT in Karlsruhe:** The 26 MeV proton beam is used to irradiate the samples. The energy of the protons is reduced by the time they arrive at the irradiation area to 23 MeV and are thus referenced as **23 MeV protons** or $\mathbf{p}_M$. The dosimetry is performed using Ni foils and measuring the ^{57}Ni activation. The uncertainty of the dosimetry is estimated as ≈ 10 %. In addition, a systematic uncertainty of the hardness factor of ≈ 15% has to be taken into account, but is not displayed in the following figures. Since the beam spot is very small, the samples are scanned by a X-Y-stage to irradiate the samples uniformly. That way it usually takes several hours to reach the targeted fluence. The irradiation area is cooled to avoid annealing during irradiation. For more information see [48] and [49].

5.3 Annealing

As discussed in sections 3.4.1 and 3.4.2, the operational parameters can change with time. To better understand the time dependence, the samples are repeatedly annealed and measured.

5.3.1 Annealing Procedure

The chosen annealing procedure is shown in table 5.5.
The two most common annealing temperatures used are 60 °C and 80 °C. The higher the tem-

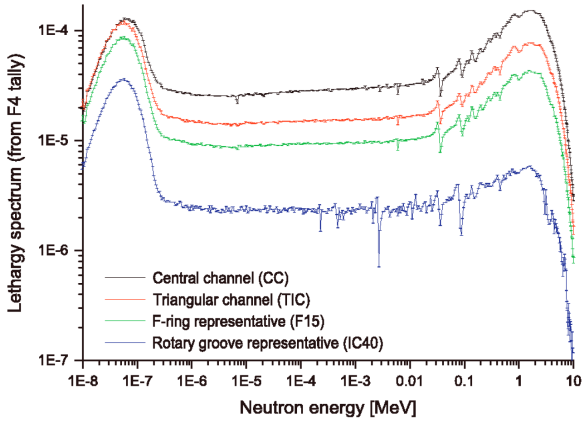

Figure 5.10: Neutron spectrum in the irradiation facility at JSI. Figure taken from [46].

perature, the faster the annealing process. Here a mixed procedure is used to reduce the time uncertainty for the first steps, which are performed at 60 °C. Staying with 60 °C would lead to very long annealing times for the last steps. To have reasonable annealing times the later steps are performed at 80 °C.

Step number	0	1	2	3	4	5	6	7
Time [minutes]	10	20	20	40	76	15	30	60
Temperature [°C]	60	60	60	60	60	80	80	80
Cumulated time (at 60°C)[minutes]	10	30	50	90	166	$\sim$ 360	$\sim$ 750	$\sim$ 1530
Measurements	a/b	a	a	a/b	a	a/b	a	a/b

Table 5.5: Annealing procedure. The annealing temperature is switched to 80°C for longer annealing to reduce the time. The time scaling given here is for the annealing of the dark current. The scaled annealing time of the full depletion voltage is lower by about 15 to 30 %. Measurements labeled "a" mean the current voltage and capacitance voltage characteristic, measurements labeled "b" mean the TCT measurements.

5.3.2 Annealing during PS irradiation

To take the annealing during irradiation of samples irradiated at the PS into account, the annealing is estimated using the expected dark current annealing discussed in section 3.4.2.
The difficulty here is that in contrast to the usual measurement procedure, where a sample is first irradiated, then measured and annealed, the samples already annealed during irradiation. This results in a superposition of defects created during the irradiation. It starts with defects created right in the beginning that annealed during the whole irradiation time and ends with the defects created in the last seconds of irradiation, that have nearly no annealing. Since the

annealing of defects contributing to the dark current is different from those contributing to the full depletion voltage, different annealing estimations should be used. However, the annealing curve of the full depletion voltage (as discussed in 3.4.1) leads to a superposition of curves that does not allow to estimate an "effective annealing" time, so only the current annealing curve is used.
Using equation 3.23, $\alpha_{irr}(t_{irr}, T_{irr})$ is given by:

$$\alpha_{irr}(t_{irr}, T_{irr}) = \frac{\sum_{i=0}^{n-1} \alpha(i \cdot \Delta t, T_{irr})}{n} \qquad \text{with} \qquad n \cdot \Delta t = t_{irr} \tag{5.25}$$

The effective annealing time can be determined by using the monotonic decreasing equation 3.23 and the resulting $\alpha_{irr}(t_{irr}, T_{irr})$ of equation 5.25.

Operational material characteristics

This chapter presents the material characteristics after irradiation. The silicon material used can have a large impact on the performance of the strip sensors. Three different properties of the silicon material are varied in this work:

1. Polarity and bulk doping: Depending on the bulk doping p-type (n-on-p) or n-type (p-on-n) either electrons or holes drift to the readout strips and give the main contribution to the signals induced by ionizing particles.

2. Thickness: The thickness influences all main properties of the sensor, the collected charge, the full depletion voltage, the leakage current and the spacial resolution. A thin sensor has a lower leakage current, a lower full depletion voltage and a better spacial resolution, but also a lower generated charge.

3. Impurities: Depending on the production method the concentration of impurities like oxygen varies. The irradiation damage depends on the impurities, enabling defect engineering.

The three main properties are discussed for the available materials, including different polarities, thicknesses and impurity levels.
Since it is most interesting whether the materials can survive the HL-LHC runtime, they were irradiated as discussed in section 5.2. The fluences are given as 1 MeV neutron euqivalent fluence (Φ_{eq}) in units of [$10^{14}\,\mathrm{cm}^{-2}$] and the particles used are referenced as $\mathbf{p}_G$ for **23 GeV protons**, $\mathbf{p}_M$ for **23 MeV protons**, and **n** for **neutrons**. So, for example, the irradiation with 23 MeV protons to a nominal fluence of $\Phi_{eq} = 3 \cdot 10^{14}\,\mathrm{cm}^{-2}$ is referenced as 3 p_M.

6.1 Reverse current

The reverse current normalized to the volume of the test device at a given annealing time is found by [32] to be proportional to the fluence and independent of the material (as discussed in section 3.4.2).
The uncertainty of the fluence is about 10 % (see section 5.2).

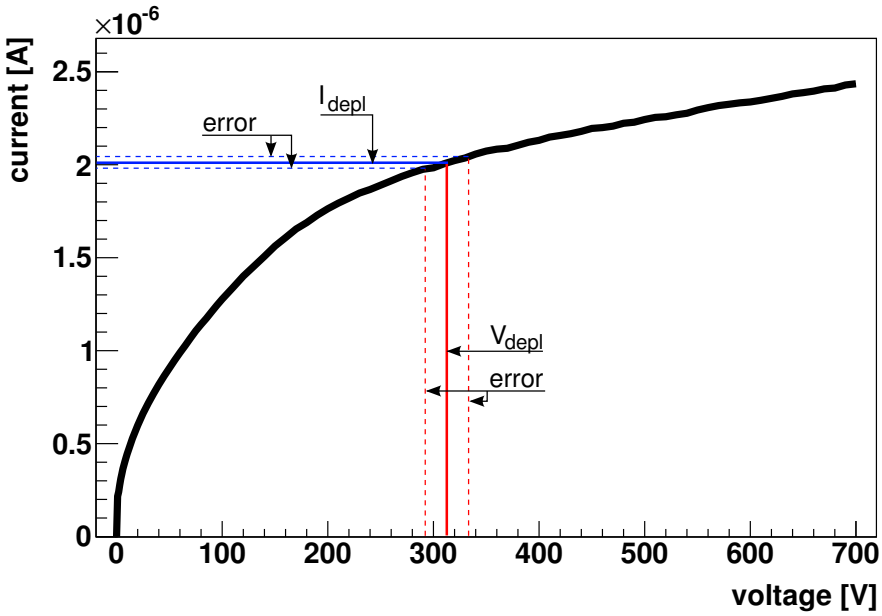

Figure 6.1: The reverse current of a FZ200P pad sensor irradiated with 3 p_G and 4n after 97 minutes annealing at 60 °C. The current does not saturate at the full depletion voltage. The current still increases linearly with the bias voltages, making it difficult to obtain the correct reverse current at the full depletion voltage.

The uncertainty of the current consists of a variety of uncertainties. The first part comes from the current itself, with a current measurement uncertainty that is estimated as 3 %. The used current $I_{V_{depl}}$ is read at the full depletion voltage, which is determined using the capacitance-voltage characteristic, as discussed in 2.2.2. The uncertainty of the full depletion voltage is estimated as 3 % of the full depletion voltage plus 10 V (See figure 6.1). The current value of the measurement shown in figure 6.1 is $I_{V_{depl}} = 2.03 \pm 0.06\,\mu A$ at a full depletion voltage of $V_{depl} = 313 \pm 19\,V$.
To have the reverse current comparable with older measurements that were performed at room temperature, the current is scaled to 20 °C using equation 2.9. In the scaling the error of $I_{V_{depl}}$ is used as well as the uncertainty in the measured temperature of 0.25 °C and an error of the generation energy of 0.4 % (see [18]) are used. The resulting value for the example is $I^{20\,°C}_{V_{depl}} = 119 \pm 4\,\mu A$.
The resulting reverse current at 20 °C is then normalized to the volume of the samples for better

comparison. For that an uncertainty of the sample area of 1 % and thicknesses and their uncertainties that are calculated from the C/V-measurements (given in table 5.2) are used. The resulting values as well as the uncertainties of the sample showing the highest current per fluence are shown in figure 6.2. The normalized value for the example is $I_{V_{depl}}^{20°C,norm} = 23.7 \pm 1.1\,\mathrm{mA\,cm^{-3}}$.

Figure 6.2 shows the reverse current at full depletion and an annealing of 80 minutes at 60 °C. In general, the current follows the expectation within the errors, although a significant spread within one irradiation can be observed at some higher fluences. This is caused by the different voltage at which the current is determined, due to different full depletion voltages. In addition to the saturation of the current as a function of voltage expected for a non-irradiated pad sensor, a linear term is found (see figure 6.1).
A dependence on the material apart of the full depletion voltage was not found.

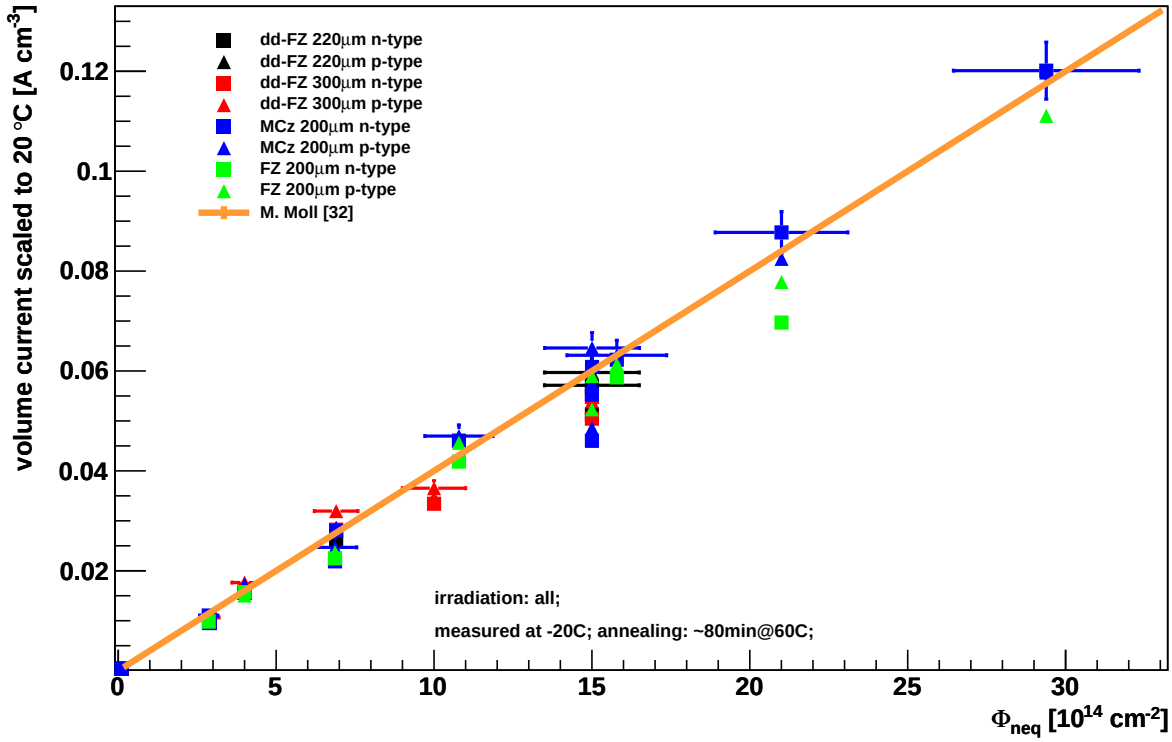

Figure 6.2: Reverse current of pad sensors normalized to their volume, irradiated to a variety of fluences, using all available irradiation facilities at a given annealing. The orange line represents the expectation according to [32].

6.1.1 Current fluence fit

The reverse current can be used to determine the fluence using the expectations of [32]. The fits were performed using equation 3.23 with the fluence as a free parameter and the annealing

as well as the volume fixed. The results of the fits are shown in tables 6.1 and 6.2. The given errors are only statistical. Most results are compatible with the dosimetry, only the additional neutron irradiation of p_G + n seems to be 10 to 20 % low. Nevertheless the dosimetry values are used further on because of the problems concerning the dependence of the reverse current on the full depletion voltage.

Φ_{eq}	3 p_M [10^{14} cm^{-2}]	3 p_M + 4 n [10^{14} cm^{-2}]	10 p_M [10^{14} cm^{-2}]	10 p_M + 5 n [10^{14} cm^{-2}]	15 p_M [10^{14} cm^{-2}]
dd-FZ220N	2.40 ± 0.04	6.55 ± 0.12	–	15.2 ± 0.28	13.0 ± 0.24
dd-FZ220P	2.40 ± 0.05	7.29 ± 0.14	9.04 ± 0.21	14.7 ± 0.28	14.3 ± 0.27
dd-FZ300N	2.63 ± 0.04	7.35 ± 0.12	8.85 ± 0.18	14.8 ± 0.24	12.8 ± 0.21
dd-FZ300P	2.65 ± 0.04	8.00 ± 0.14	9.32 ± 0.19	15.2 ± 0.28	14.0 ± 0.23
MCZ200N	2.40 ± 0.04	7.17 ± 0.14	–	14.8 ± 0.29	12.2 ± 0.24
MCZ200P	2.32 ± 0.05	7.11 ± 0.14	–	14.8 ± 0.29	12.3 ± 0.24
Mean	2.48 ± 0.02	7.21 ± 0.05	9.06 ± 0.11	14.9 ± 0.1	13.0 ± 0.1
Dosimetry	2.9 ± 0.3	6.9 ± 0.4	10 ± 1.0	15 ± 1.1	15 ± 1.5

Table 6.1: Measured fluences for p_M and p_M + n irradiations using the reverse current annealing.

Φ_{eq}	3 p_G [10^{14} cm^{-2}]	3 p_G + 4 n [10^{14} cm^{-2}]	10 p_G [10^{14} cm^{-2}]	10 p_G + 5 n [10^{14} cm^{-2}]	15 p_G [10^{14} cm^{-2}]	15 p_G + 6 n [10^{14} cm^{-2}]
FZ200N	2.59 ± 0.05	6.01 ± 0.10	9.65 ± 0.18	14.5 ± 0.24	–	19.3 ± 0.32
FZ200P	2.58 ± 0.05	6.41 ± 0.11	10.9 ± 0.21	15.7 ± 0.26	13.8 ± 0.27	19.5 ± 0.32
MCZ200N	2.91 ± 0.05	6.04 ± 0.10	10.6 ± 0.21	14.7 ± 0.25	14.2 ± 0.28	19.7 ± 0.33
MCZ200P	2.71 ± 0.05	6.54 ± 0.32	10.3 ± 0.20	14.9 ± 0.25	15.4 ± 0.30	19.5 ± 0.33
Mean	2.70 ± 0.03	6.15 ± 0.06	10.3 ± 0.1	14.9 ± 0.1	14.4 ± 0.2	19.5 ± 0.2
Dosimetry	$2.9 \pm .3$	6.9 ± 0.4	11 ± 1.1	16 ± 1.1	15 ± 1.5	21 ± 1.6

Table 6.2: Measured fluences for p_G and p_G + n irradiations using the reverse current annealing.

The uncertainties of the fluences from dosimetry are discussed in section 5.2. For the mixed irradiations the square root of the sum of the uncertainties for the single irradiations is used.

6.2 Full depletion voltage

6.2.1 General considerations

The C/V characteristic of an irradiated silicon diode depends strongly on the device temperature and measurement frequency, as shown in figures 6.3a and 6.3b. Therefore, the extracted full depletion voltage also exhibits such dependencies.

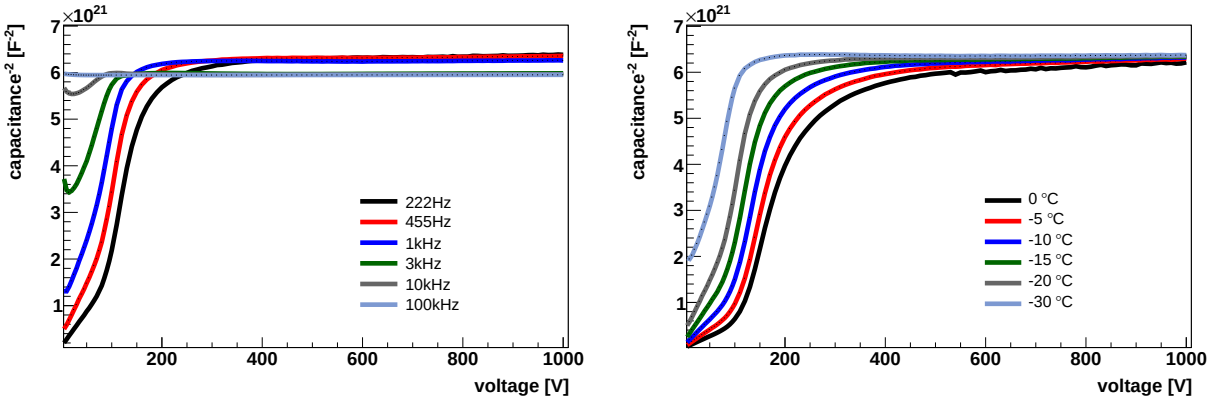

(a) Frequency dependence of C/V measurements at -20 °C.

(b) Temperature dependence of C/V measurements at 455 Hz.

Figure 6.3: Frequency and temperature dependence of C/V measurements of a MCz200P pad sensor irradiated with 10 p_G and annealing of 120 minutes at 80 °C.

This dependence of the C/V characteristics is caused by defects of the silicon bulk lattice that are charged and discharged by the AC voltage used for the measurement.
This charge and discharge is described by capture and emission of electrons and holes. The capture probabilities are $k_e \propto exp((E_{Fe} - E_i)/kt)$ for electrons and $k_h \propto exp((E_i - E_{Fh})/kt)$ for holes with the intrinsic carrier density E_i and the quasi-Fermi levels of electrons and holes. The emission probabilities are $g_e \propto exp\left((E_t - E_i)/kt\right)$ for electrons and $g_h \propto exp\left((E_i - E_t)/kt\right)$ for holes with the defect level E_t. The temperature dependency of the emission and capture probability are responsible for the temperature dependence of the C/V measurement (see [50]). The frequency dependence is different for high and low measurement frequencies. If $\omega\tau \gg 1$ with the measurement frequency ω and the time constant τ of a defect, the capacitance is independent of the bias voltage

$$C(V) \to \frac{\epsilon\epsilon_0}{d_{Si}} \cdot A$$

with the thickness d_{Si} and the area A of the sensor. For low measurement frequencies $\omega\tau \ll 1$ the capacitance is given by

$$C(V) \approx \frac{\epsilon\epsilon_0}{\sqrt{\frac{2\epsilon\epsilon_0}{N - N_t(\omega)}(\Phi_t - V)}} \cdot A$$

with the difference between the defect energy level and the Fermi level Φ_t, the doping concentration N and the defect concentration (see [51]):

$$N_t(\omega) = \frac{N_t}{1+\omega^2\tau^2}$$

The "standard" frequency and temperature used for C/V measurements in the past were 10 kHz and 20 °C. However, due to the high irradiation and the resulting high reverse current a measurement at this temperature is not possible.
The majority of measurements was performed at 0 °C with 1 kHz and at -20 °C with 455 Hz and 1 kHz. In this work the C/V measurements at -20 °C with 455 Hz are used, if not stated otherwise. The temperature is motivated by the fact that the planned operating temperature in the CMS tracker is -20 °C. And the choice of frequency is supported by the well matching full depletion voltage extracted from the 455 Hz C/V measurement and the saturation voltage of the trapping corrected CCE measurements at -20 °C, as shown in figure 6.5b.

Comparison of the saturation voltage of the charge collection with the full depletion voltage

As shown in figures 6.3a and 6.3b, the full depletion determined from the capacitance voltage characteristic depends strongly on the measurement frequency and temperature. The set of parameters for the measurements mainly used in this work is 455 Hz at -20 °C.
A way to determine the best parameter set for the C/V measurement with respect to the full depletion voltage is the comparison with the saturation voltage of the charge collection.
The comparison is shown in detail for one example in figure 6.4. The capacitance voltage and charge collection efficiency voltage characteristic show a visible difference in the kink where the full depletion voltage is reached and the charge collection "saturates". This increase of charge collection with voltage can be explained by reduction of trapping for higher voltages. This trapping can be corrected with different methods. The correction method used here is discussed in detail in [52]. A short summary is given here:

$$CCE_{corr} = \frac{CCE_{meas}}{\frac{\bar{\lambda}}{d}\left(1-e^{-\frac{d}{\bar{\lambda}}}\right)}$$

with the effective drift distance $\bar{\lambda}$, and the thickness of the sensor d. The effective drift distance $\bar{\lambda}$ is the distance in which the number of free charge carriers N is reduced to 1/e.

$$dN = -\frac{N}{\bar{\lambda}}dx$$

After the trapping correction is applied, the charge collection really saturates at the full depletion voltage and the saturation voltage is compatible with the full depletion voltage determined from the capacitance voltage characteristic.
The saturation voltage of the charge collection was compared to the full depletion voltage from the C/V measurement of the same pad sensor (see figure 6.5).
Figure 6.5a shows that the saturation voltage from the CCE measurements is higher than the

full depletion voltage from the C/V measurements.
The charge collection efficiency is reduced by trapping, which also shifts the saturation to a higher value. This trapping was corrected for figure 6.5b by assuming a linear drift distance with bias voltage that is fitted in a high bias voltage region (for more information on trapping see [34]). Unfortunately, the correction can fail which leads to a CCE > 1 at low voltages, making it impossible to determine the saturation voltage of the charge collection. Those measurements were discarded while producing the comparison shown in figure 6.5b.
The saturation voltage of the trapping corrected CCE measurements fit the full depletion voltage determined from CV measurements well.

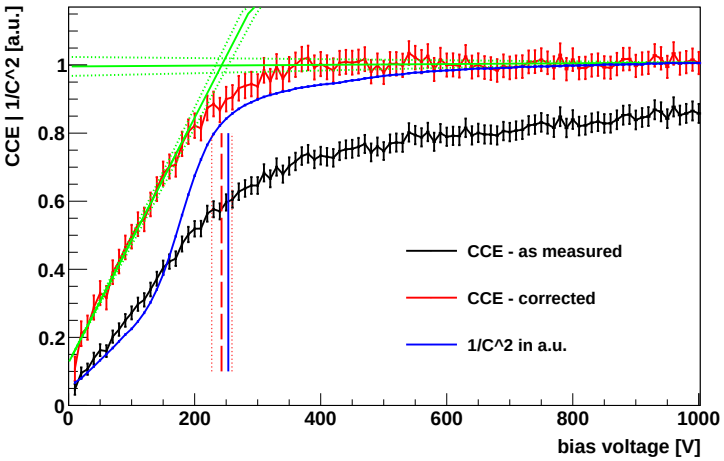

Figure 6.4: The raw CCE measurement is shown in black, the trapping corrected CCE in red and a scaled $1/C^2$ curve is shown in blue as a comparison. The shown measurements are performed on a FZ200N sample after 15 p_G irradiation and 10 minutes at 60 °C additional annealing. The vertical lines indicate the full depletion voltage (blue) and saturation voltage (red).

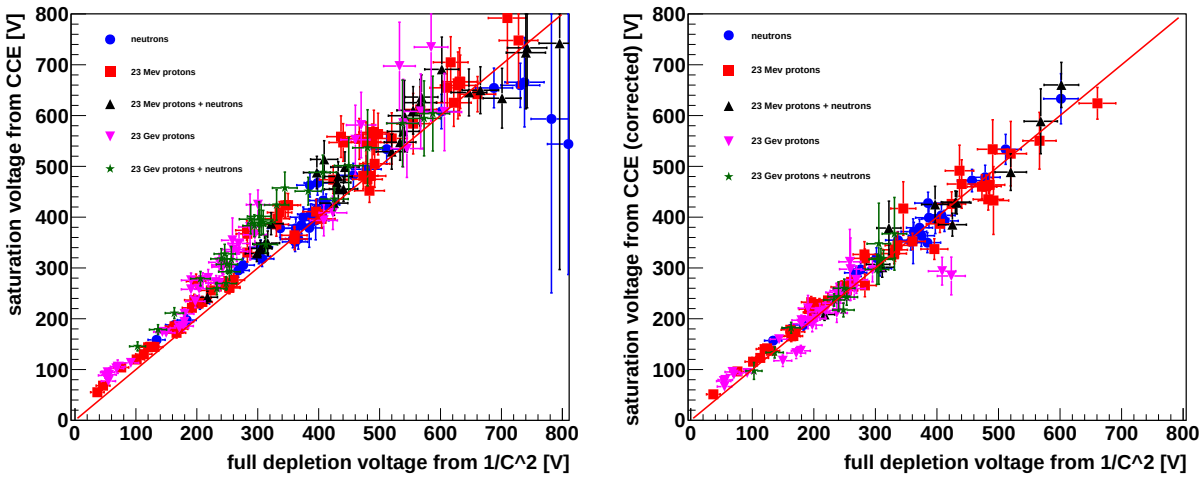

(a) CCE saturation vs. full depletion voltage from C/V

(b) Trapping corrected CCE saturation vs. full depletion voltage from C/V

Figure 6.5: Figure (a) shows a correlation between the saturation voltage from the charge collection efficiency measurement and the full depletion voltage from the capacitance voltage characteristics of the same pad sensors. Figure (b) shows the same correlation using a trapping corrected charge collection efficiency. The line indicates the same values for both methods.

Expectation of the development of the full depletion voltage with irradiation

Before the development of the full depletion voltage due to changes to the effective space charge caused by irradiation will be discussed, a short summary of the expectations is given. As discussed in the thesis of A. Junkes [27], different defects that act as acceptors or donors are created in silicon during irradiation.
For most materials and irradiations, the dominantly produced defects are acceptor-like and lead to a negative space charge. However, in irradiations of oxygen rich silicon with high energetic charged particles, donors are dominantly produced.

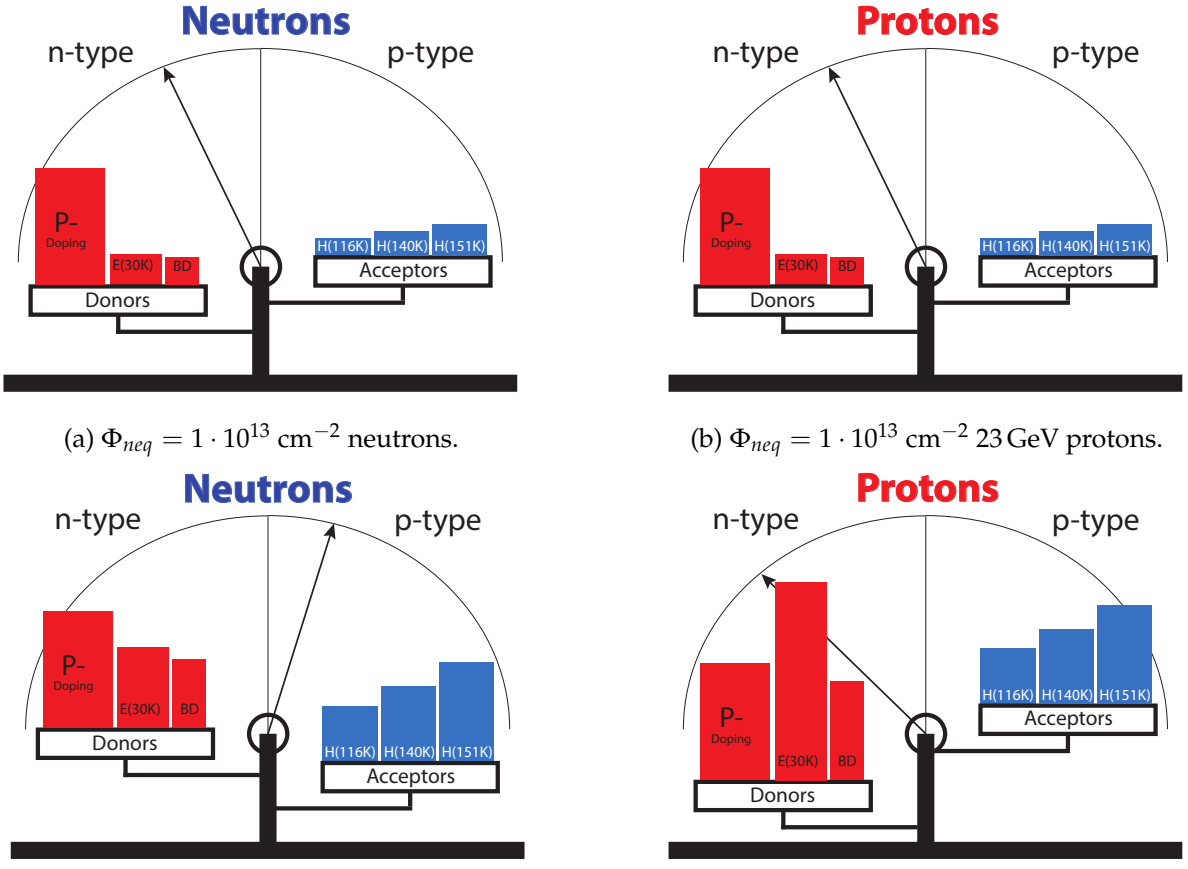

(a) $\Phi_{neq} = 1 \cdot 10^{13}$ cm^{-2} neutrons.

(b) $\Phi_{neq} = 1 \cdot 10^{13}$ cm^{-2} 23 GeV protons.

(c) $\Phi_{neq} = 2 \cdot 10^{15}$ cm^{-2} neutrons.

(d) $\Phi_{neq} = 2 \cdot 10^{15}$ cm^{-2} 23 GeV protons.

Figure 6.6: Acceptor and donor development in oxygen rich MCz material with irradiation of neutrons and 23 GeV protons. Figure taken from [27].

In figure 6.6 a qualitative picture of the irradiation of oxygen rich MCz n-bulk silicon material with neutrons and 23 GeV protons is shown. While the acceptor-like defects change the space charge sign to negative after neutron irradiation, it stays positive for 23 GeV proton irradiation. In table 6.3 the produced effective space charge sign is summarized for the oxygen lean float-

ing zone and the oxygen rich magnetic czochralski materials by the irradiation with different particles.

Material	neutrons	23 MeV protons	23 GeV protons
FZ	–	–	–
MCz	–	–	+

Table 6.3: Creation of space charge by irradiation with different particles.

6.2.2 Dependence of the full depletion voltage on fluence

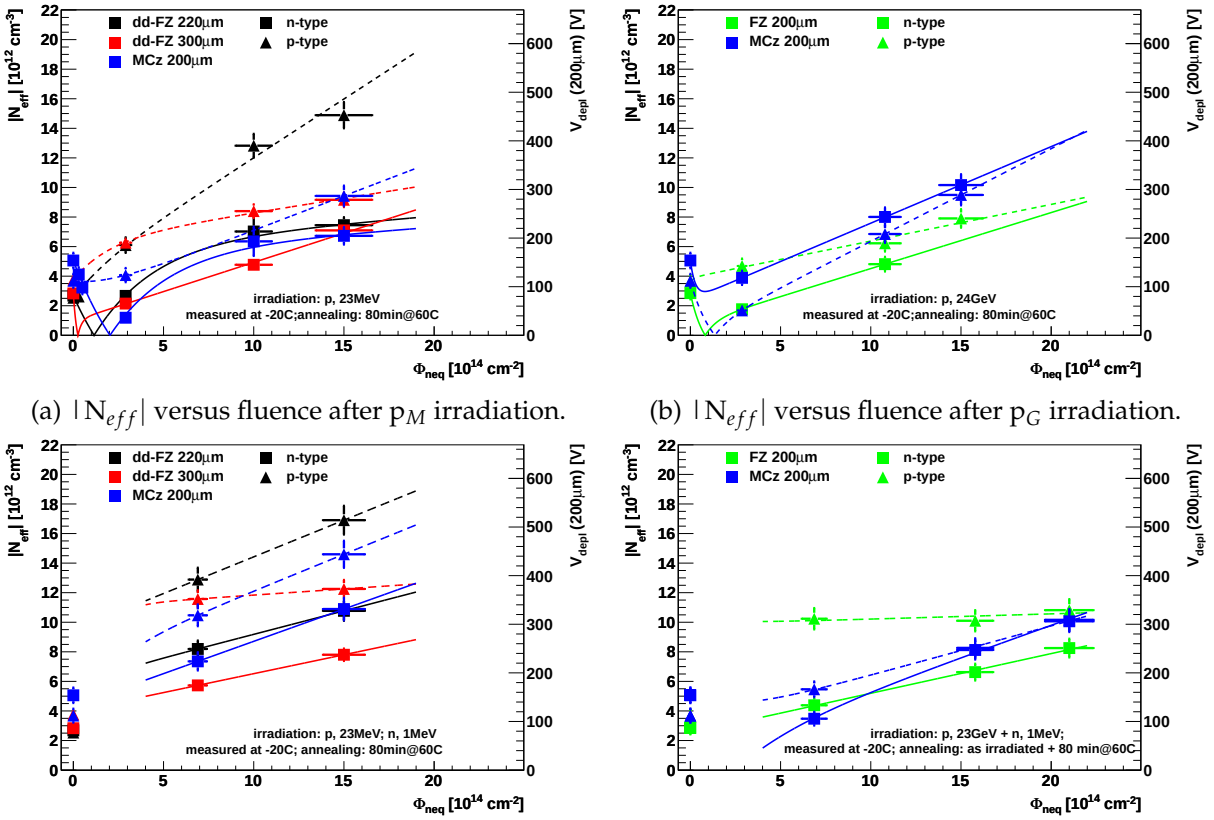

(a) $|N_{eff}|$ versus fluence after p_M irradiation.

(b) $|N_{eff}|$ versus fluence after p_G irradiation.

(c) $|N_{eff}|$ versus fluence after p_M + n irradiation.

(d) $|N_{eff}|$ versus fluence after p_G + n irradiation.

Figure 6.7: The full depletion voltage development with fluence for different materials at a fixed annealing of $\approx$ 80 minutes at 60 °C, which corresponds to the minimum (p-type) / maximum (n-type) value for the full depletion voltage as function of annealing time. Lines in figures (c) and (d) are used to guide the eye.

The irradiation leads to a change of the full depletion voltage by deactivating the original doping and introducing new defects that change the space charge of the depletion region (see [32]). This will not only result in the change of the voltage needed to operate the sensor, but can also affect the shape of the electric field in the sensor bulk. One important effect is the so-called space charge sign inversion (SCSI), described in section 3.4.1. The full depletion voltage is reduced in the low fluence range, then the sign of the space charge changes and the full depletion voltage increases with increasing fluence. This effect occurs if the created space charge has the opposite sign of the original dopants.
Figure 6.7 shows the development of the full depletion voltage. For a better comparison of the different materials the full depletion voltage is scaled to a thickness of 200 µm, using equation 2.1. The lines are fits with the Hamburg model, which is reasonable for the single irradiations (figures 6.7a) and (6.7b), but not anymore for the mixed irradiations (figures 6.7c) and (6.7d), where it is used to guide the eye. A full description is given in sections 6.2.4 and 6.2.5.
The 23 MeV proton irradiation (figure 6.7a) leads to a space charge sign inversion (SCSI) of all n-bulk materials and none of the p-bulk materials.
The 23 GeV proton irradiation (figure 6.7b) leads to a SCSI of FZ200N and MCz200P. The SCSI of MCz200P is caused by the oxygen dependent creation of donors at irradiation with high energetic protons.
The additional neutron irradiation after the 23 MeV proton irradiation (figure 6.7c) does not change the SCSI of any of the materials. The full depletion voltage of all materials is increased with respect to the single proton irradiation. The increase of the full depletion voltage with fluence of the dd-FZ300P material, however, seems to be low, which should result in a steep increase of full depletion voltage at very low fluences, due to the high neutron fraction there.
The additional neutron irradiation after the 23 GeV proton irradiation (figure 6.7d) changes the space charge sign from positive to negative of both MCz materials (n- and p-type) due to a strong acceptor creation. The donors that were dominantly created by 23 GeV proton irradiation in oxygen rich silicon (MCz) are compensated by the acceptors that are dominantly created by neutron irradiation leading to a reduction in full depletion voltage. This is referred to as the "compensation effect".
A more detailed description can be found in section 6.2.3. The FZ200P material shows a very high full depletion voltage already at low fluences but no increase with fluence is observed in the studied samples.

The full depletion voltage of the dd-FZ300 material after 23 MeV proton and neutron irradiation and the FZ200 material 23 GeV proton and neutron irradiation with similar oxygen concentrations is shown in figure 6.8a. The dd-FZ300 after 23 MeV proton and neutron irradiation shows a higher full depletion voltage at low fluences compared to FZ200 n- and p-type irradiated with 23 GeV protons and neutrons, but the increase with fluence is similar.
The comparison of the full depletion voltage of MCz materials after mixed irradiations using 23 MeV protons and neutrons and 23 GeV protons and neutrons is shown in figure 6.8b. After the 23 GeV proton and neutron irradiation the compensation of the acceptors by the higher concentration of donors after 23 GeV proton irradiation compared to 23 MeV proton irradiation leads to a lower full depletion voltage after 23 GeV proton and neutron irradiation. The increase with fluence at higher fluences, however, is similar for both irradiation types.

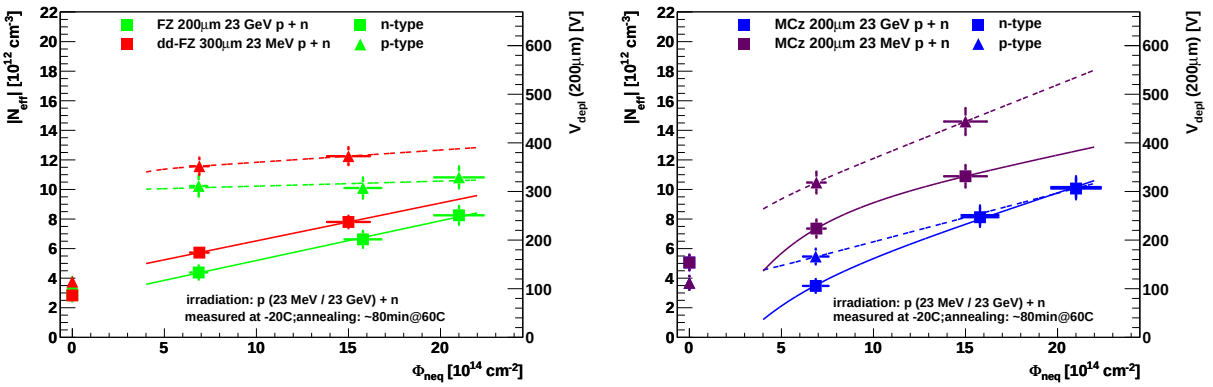

(a) FZ material (b) MCz material

Figure 6.8: Comparison of the full depletion voltage after 23 GeV proton and neutron irradiation and 23 MeV proton and neutron irradiation.

A more detailed description of the stable damage after the different irradiations is given in section 6.2.4 for the 23 MeV proton (and neutron) irradiation and in section 6.2.5 for the 23 GeV proton (and neutron) irradiation.

6.2.3 Compensation of space charge after proton and neutron irradiation

It was seen (e.g. by [53]) that the irradiation with two different particles (like protons and neutrons) can have an effect that the full depletion voltage is different from the sum of the two single irradiations. This can be explained by the different defect creation, depending on the particle type, energy and the oxygen content of the silicon sample. This compensation effect will be discussed in this section.

Development of the full depletion voltage after single 23 GeV proton and mixed 23 GeV proton and 1 MeV neutron irradiation

The development of N_{eff} after 23 GeV proton only and mixed irradiation measured in this campaign is shown in figure 6.9. Figure 6.9a shows the fluence dependence of the full depletion voltage for the medium oxygen material FZ200 and figure 6.9b for the oxygen rich material MCz200.

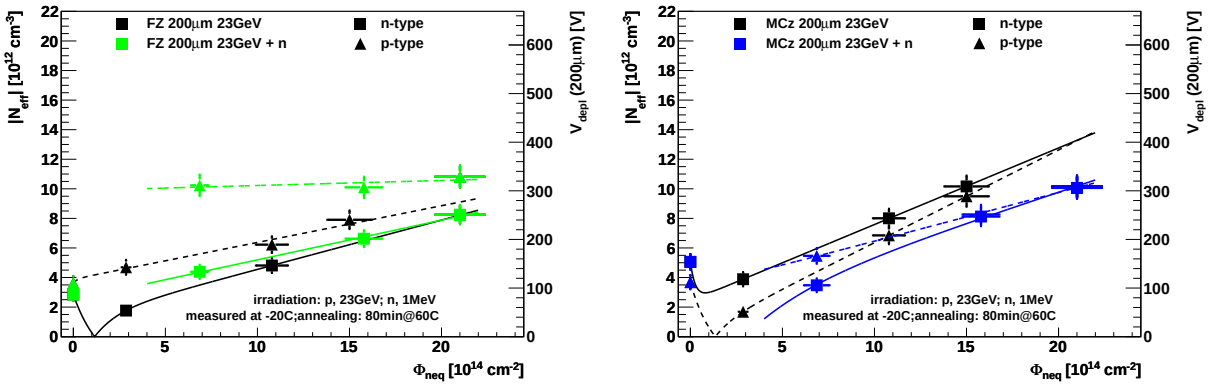

(a) FZ200 material

(b) MCz200 material

Figure 6.9: Development of the full depletion voltage after single p_G irradiation in comparison to mixed p_G + n irradiation. In the case of mixed irradiation the lines are to guide the eye only.

For the FZ200N material the change of the full depletion voltage after 23 GeV proton and neutron irradiation is, as far as it is possible to tell with less data points, similar with respect to the one of the single 23 GeV proton irradiation. The FZ200P material shows a very high N_{eff} after 23 GeV proton and neutron irradiation for low fluences, but the increase with fluence is very small. At increasing fluences the fraction of neutrons decreases, so that both curves are expected to converge at high fluences.
The full depletion voltage of the MCz200 material after 23 GeV proton irradiation is lower for p-bulk material compared to n-bulk material, due to a space charge sign inversion (SCSI) of the MCz200P material. The increase with fluence is higher for the p-bulk than for n-bulk material, so that at high fluences ($> 2 \cdot 10^{15}$ cm^{-3}) n-bulk material is expected to show a lower full depletion voltage. After the additional neutron irradiation the picture is reversed, so at low fluences the full depletion voltage of n-bulk material is reduced. This can be explained by

the dominant donor creation of 23 GeV proton irradiation in oxygen rich silicon material that is overcompensated by the dominant acceptor creation of neutron irradiation (see also [53]). The so-called compensation effect, that the full depletion voltage is smaller for a given fluence after mixed irradiation than that for 23 GeV proton irradiation only, is clearly visible for the n-bulk MCz200 material at all fluences. For high fluences this effect is also observed for the p-bulk MCz200.

Annealing of single and mixed irradiated sensors

As shown before, the mixed irradiation can have beneficial effects on N_{eff}. In this section the annealing of N_{eff} of single and mixed irradiations is discussed for 23 GeV and 23 MeV protons and additional neutrons at the lowest fluence used in this campaign.

23 MeV proton and neutron irradiation The two single irradiations with $3 \cdot 10^{14}\,\mathrm{cm}^{-2}$ 23 MeV protons (figure 6.10a) and $4 \cdot 10^{14}\,\mathrm{cm}^{-2}$ neutrons (figure 6.10b) show both the annealing behavior that is typical for p-bulk material (acceptor reduction in the short term and creation in the long term annealing). This is a strong hint that all originally n-bulk materials underwent a space charge sign inversion, whereas the space charge sign stayed the same for all p-bulk materials. This can be explained by a strong donor removal reducing the positive space charge for the n-bulk materials and an acceptor generation, increasing the negative space charge for all materials.

The curves in figures 6.10a and 6.10b show fits with the Hamburg model, described in 3.4.1. In figure 6.10c the data shows the mixed irradiation with $3 \cdot 10^{14}\,\mathrm{cm}^{-2}$ 23 MeV protons and $4 \cdot 10^{14}\,\mathrm{cm}^{-2}$ neutrons. The dotted lines show the fit with a summation of the ΔN_{eff} fitted in figures 6.10a and 6.10b:

$$N_{eff} = \Delta N^{p}_{eff}(\Phi^{p}_{eq}, t^{p}, T^{p}_{a}) + \Delta N^{n}_{eff}(\Phi^{n}_{eq}, t^{n}, T^{n}_{a}) - \Delta N^{p}_{donor\ removal}(\Phi^{p}_{eq}) + N^{0}_{eff} \tag{6.26}$$

The absolute height of the annealing curve that is given by the stable damage is corrected for the double counting of the donor removal with the $N^{p}_{donor\ removal}(\Phi^{p}_{eq})$ term that is determined by fits on the stable damage (see section 6.2.4). The donor removal after proton irradiation can be less strong than after neutron irradiation, according to [32], thus the donor removal of the proton irradiation is used for correction.
The dd-FZ300 materials both show a short term annealing that is very similar to the summation of both single irradiations. The oxygen rich materials dd-FZ200 and MCz200 show a stronger short term and a weaker long term annealing than expected from the single irradiation summation.
The resulting parameters for these fits are summarized in tables 1a to 1c.

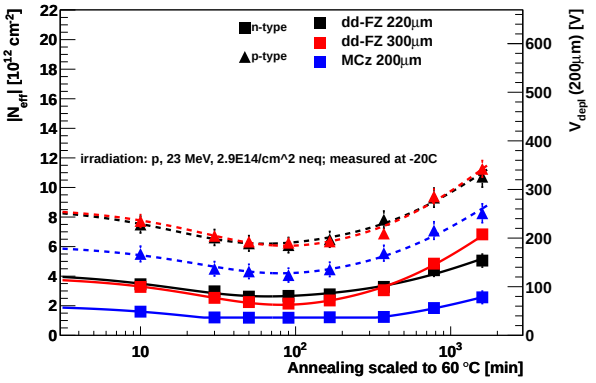

(a) 3 p_M irradiation.

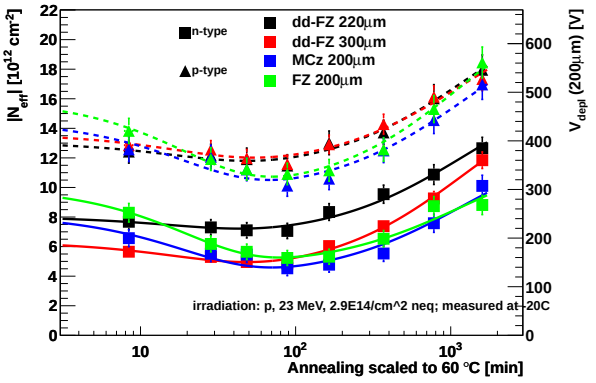

(b) 4 n irradiation.

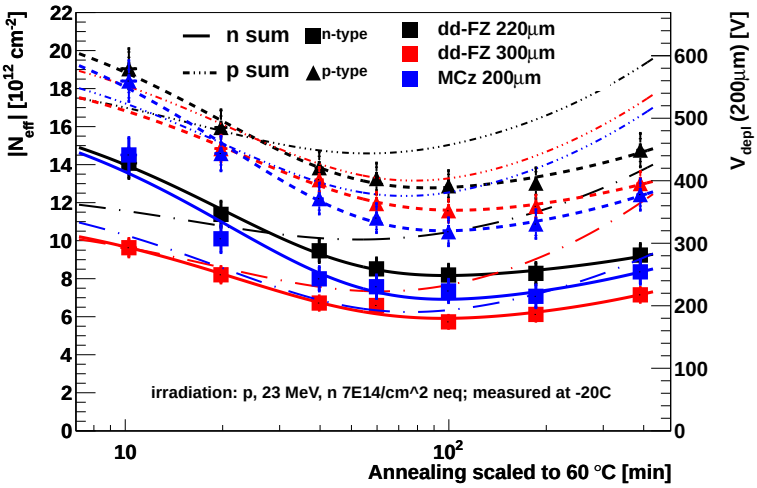

(c) 3 p_M + 4 n irradiation.

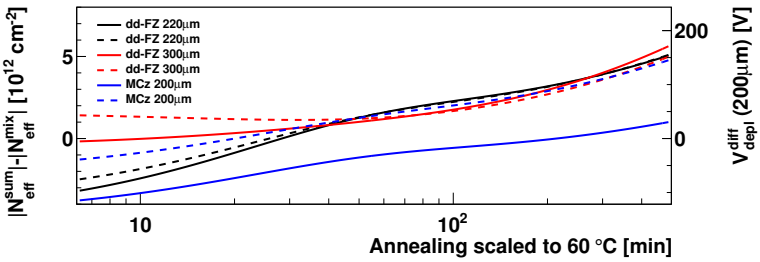

(d) 3 p_M + 4 n irradiation difference.

Figure 6.10: Annealing of full depletion voltage after 3 p_M, 4n and 3 p_M + 4 n irradiation. The solid and dashed lines show the (for mixed irradiations adjusted) Hamburg model, the dashed-dotted lines in the figure c show the summation according to equation 6.26 of the two fitted curves of the single irradiations. The model parameters of the performed fits are given in section 1 of the appendix.

23 GeV proton and neutron irradiation The annealing of N_{eff} after mixed 23 GeV proton and neutron irradiation is shown in figure 6.11c. As a comparison, the single irradiation with 23 GeV protons is shown in figure 6.11a and the neutron irradiation is shown again in figure 6.11b.
After the single irradiation with 23 GeV protons (figure 6.11a), the FZ materials show the typical annealing behavior of p-bulk material. This indicates that the n-bulk FZ underwent a space charge sign inversion resulting in a lower N_{eff}. This agrees with the expected dominant creation of acceptors in addition to the donor removal in medium oxygen material (see [32]).
The oxygen rich MCz material shows a different behavior. The full depletion voltage of n-bulk MCz shows the typical annealing of n-bulk material with a maximum of positive space charge at about 80 minutes at 60 °C annealing. The p-bulk MCz shows a nearly constant N_{eff} at a relatively low level over the full annealing time. This indicates, that it is on the edge of a space charge sign inversion. This can be explained by an increased creation of donors, in addition to the acceptors created in all materials (see [54]). These two defect types balance each other resulting in a smaller change of the full depletion voltage.
The annealing of the FZ200 materials after the additional neutron irradiation follows the expectation from the single irradiations, however, with a fixed offset.
The short term annealing of the MCz200 materials also follows the expectation, but the long term annealing is not as pronounced as expected.
The resulting parameters for these fits are summarized in tables 1a to 1c.

Summary The predicted absolute height of the N_{eff} does not fit the measured values. This might either be caused by compensation of the proton and neutron irradiation, but might also be an effect of the irradiations not taking place at the same time. During the irradiation a very fast annealing might take place of defects that can interact with newly created defects. These are already annealed out, when the irradiations take place with weeks or month in between, even at low temperatures.
The short term annealing of the 23 MeV proton and neutron irradiated dd-FZ300 samples and 23 GeV proton and neutron irradiated FZ200 and MCz200 samples can be described by the summation of the single irradiations. The long term annealing is weaker than expected from the summation of the single irradiations for all materials, except the FZ200 material after 23 GeV proton and neutron irradiation. This is summarized in table 6.4.

Material	short term	long term
FZ200	✓	✓
MCz200	✓	weak

(a) 23 GeV proton and neutron irradiation

Material	short term	long term
dd-FZ220	strong	weak
dd-FZ300	✓	weak
MCz200	strong	weak

(b) 23 MeV proton and neutron irradiation

Table 6.4: Measured compared to expected annealing curve after mixed proton and neutron irradiation. "✓" means as expected, "weak" means weaker than expected and "strong" means stronger than expected.

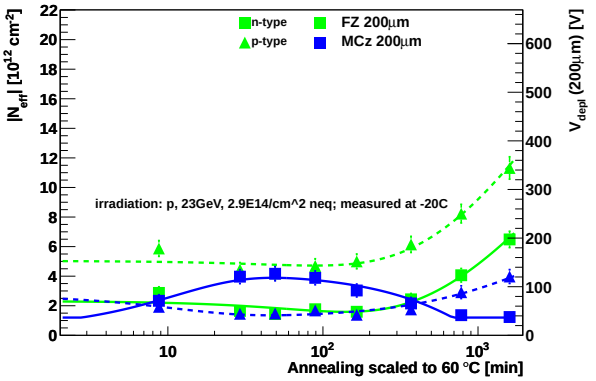

(a) 3 p_G irradiation.

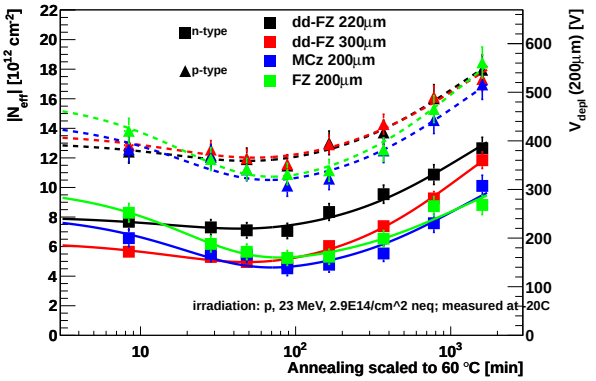

(b) 4 n irradiation. Same figure as 6.10b for comparison.

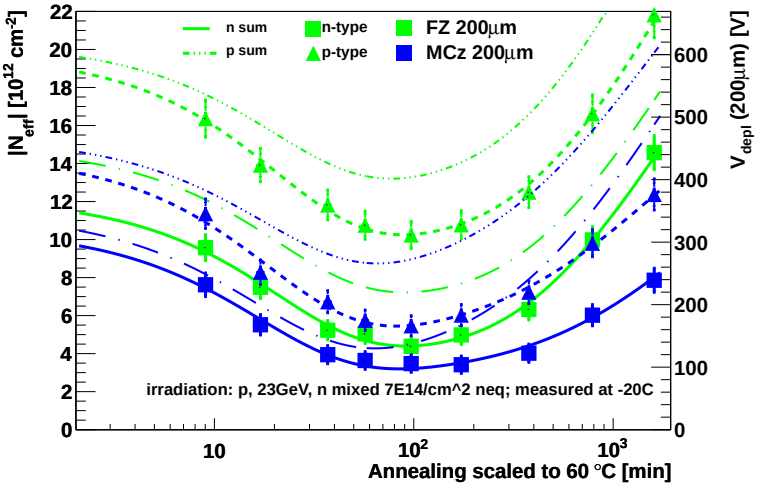

(c) 3 p_G + 4 n irradiation.

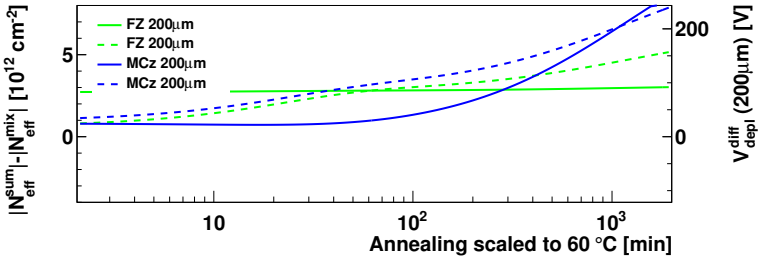

(d) 3 p_G + 4 n irradiation difference.

Figure 6.11: Annealing of full depletion voltage after 3 p_M, 4n and 3 p_M + 4 n irradiation. The solid and dashed lines show the (for mixed irradiations adjusted) Hamburg model, the dashed-dotted lines in the figure c show the summation according to equation 6.26 of the two fitted curves of the single irradiations. The model parameters of the performed fits are given in section 1 of the appendix.

Comparison to measurements by other groups

It was seen by [53] that for oxygen rich n-type material the 23 GeV proton and 1 MeV neutron irradiation can compensate their change of the full depletion voltage at fluences of a few $10^{14} cm^{-2}$ neutron equivalent (see figure 6.12 and 6.13). For all materials the full depletion voltage after 23 GeV proton and 1 MeV neutron irradiation is given by the sum of the ΔN_{eff} of the first irradiation and the dominant introduction of acceptors of the second irradiation. For the oxygen rich MCz n-type the introduction of defects in the first 23 GeV proton irradiation is dominated by donors. The change of full depletion voltage by the second (neutron) irradiation

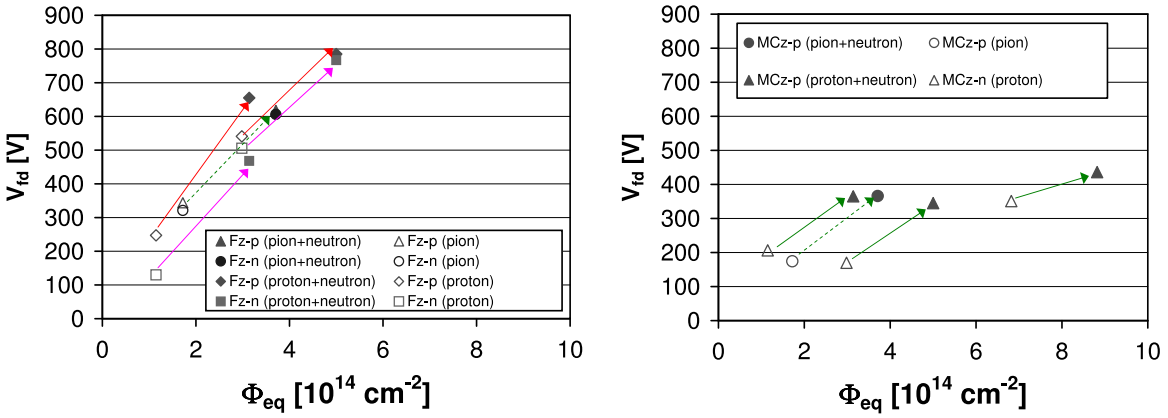

(a) FZ n- and p-type material

(b) MCz p-type material

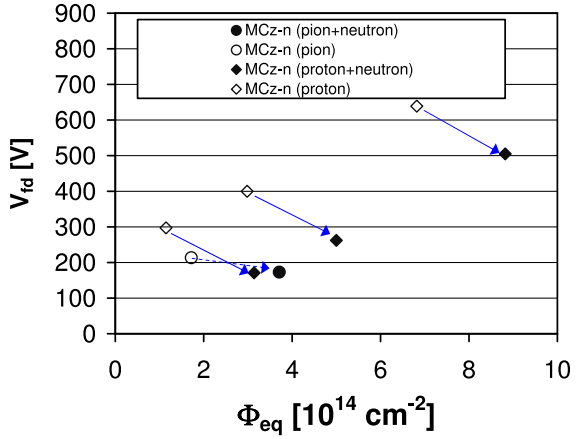

(c) MCz n-type material

Figure 6.12: Annealing of the full depletion voltage after different mixed p_G + n irradiation of ATLAS FZ (a) and MCz (b and c) materials. The arrows indicate the change of the full depletion voltage due to the second irradiation. Figures taken from [53].

as seen by [53] is shown in figure 6.12. It can clearly be seen that the full depletion voltage is increased for FZ and MCz p-type materials after an additional neutron irradiation after an irradiation with high energetic protons or pions while it is decreased for MCz n-type materials.

This is true for our materials at low fluences as well, while at high fluences both MCz materials profit from the neutron irradiation. This can well be explained by the SCSI of the MCz p-type material after high energetic proton irradiation only, leading to a full depletion voltage that is lower for the single irradiation than the mixed irradiation at fluences $< 10 \cdot 10^{14}\,\mathrm{cm}^{-2}$.

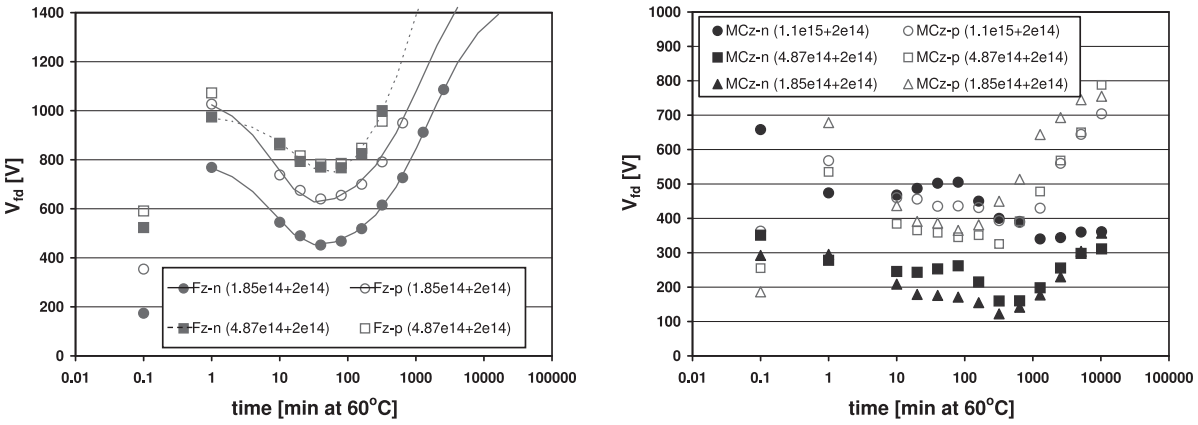

(a) FZ material

(b) MCz material

Figure 6.13: Annealing of the full depletion voltage after different mixed p_G + n irradiation of ATLAS FZ (a) and MCz (b) materials. The values at an annealing time of 0.1 minutes indicate the values of the pure proton irradiation. Figures taken from [53].

The annealing of the samples after mixed irradiation (see figure 6.13) shows a strong long term annealing for all materials except the MCz n-type which is showing a very weak long term annealing. Both MCz materials, however, show similar full depletion voltages after very high annealing times, independent of the fluence, but a difference between the n- and p-bulk MCz materials is visible.

6.2.4 Annealing of the full depletion voltage and development of the stable damage with 23 MeV proton and neutron irradiation

Annealing of the full depletion voltage after single 23 MeV proton irradiation

The annealing of the samples irradiated with 23 MeV protons with different fluences (figure 6.14) shows the typical time dependence of the p-type annealing, indicating that all n-bulk materials underwent space charge sign inversion after fluences $\Phi_{neq} \geq 3 \cdot 10^{14}\,\mathrm{cm}^{-2}$, as shown in table 6.5. The short term annealing is similar for all tested materials. However, the long term annealing of the oxygen rich materials is weak compared to the materials with a lower oxygen content.
The annealing of the n-bulk materials shows a lower full depletion voltage for all fluences, due to the original donor doping. The initial doping is partly deactivated at low fluences, however, a part remains active. The acceptors, that are dominantly created by irradiation with 23 MeV protons are partly balanced by remaining donors.

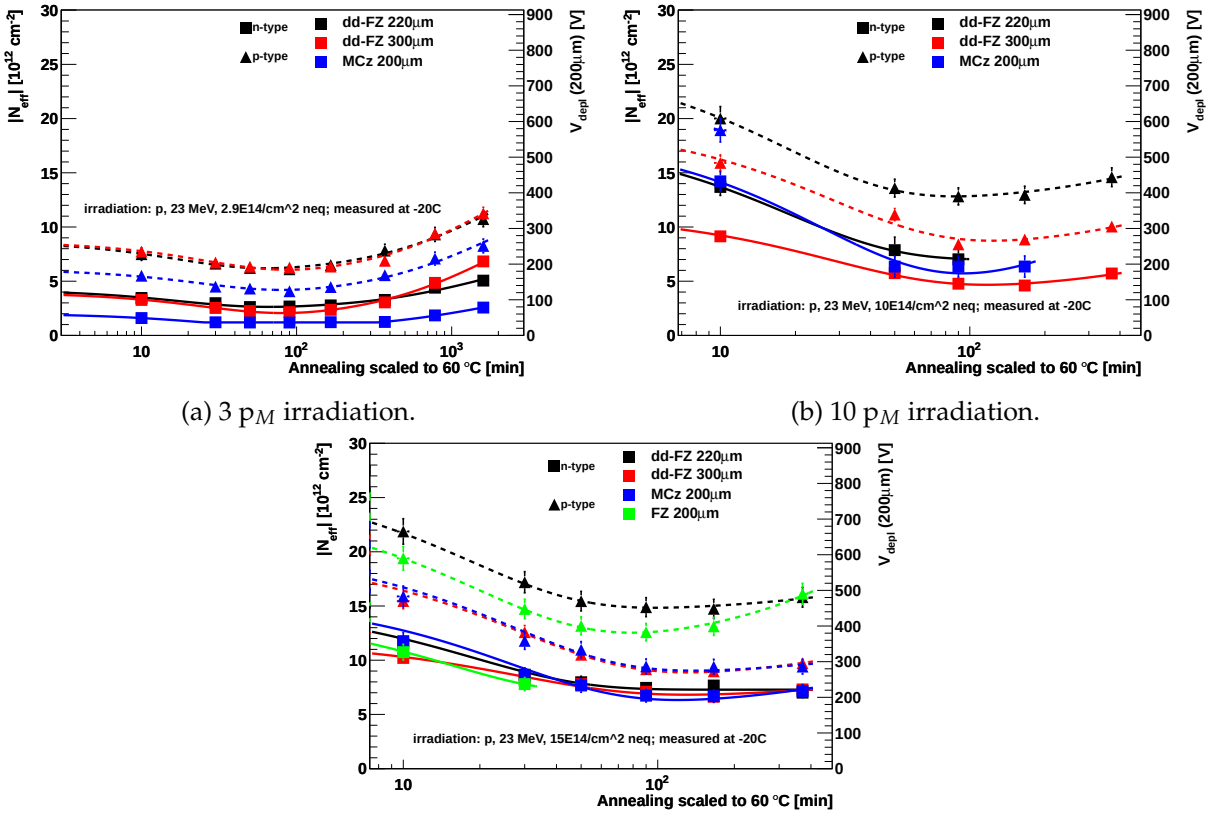

(a) 3 p_M irradiation.

(b) 10 p_M irradiation.

(c) 15 p_M irradiation.

Figure 6.14: Annealing of the full depletion voltage after single p_M irradiation, with 3 p_M (a), 10 p_M (b) and 15p $_M$ (c). The model parameters of the performed fits are given in section 2 of the appendix.

The data in figure 6.14 is described using the Hamburg model, discussed in section 3.4.1. The parameters for the short term and long term annealing introduction rates and the stable damage are free parameters, the time constants, however, are fixed, due to the small number of data points. The long term annealing time constant after 23 MeV proton irradiation was estimated from the time constants after neutron and 23 GeV proton irradiation for the oxygenated float zone from data found in [55] to be about $\tau_y = 150$ minutes at 80 °C, which corresponds to about $\tau_y = 2100$ minutes at 60 °C.
The short term annealing time constants were determined using global fits over all dd-FZ220, dd-FZ300 and MCz200 samples (six of each). The time constant at 60 °C for the used dd-FZ220 samples was found to be $\tau_a = 19$ minutes, the time constant for the used dd-FZ300 samples was found to be $\tau_a = 30$ minutes and the time constant for the used MCz samples was found to be $\tau_a = 28$ minutes.

Annealing of the full depletion voltage after mixed 23 MeV proton and neutron irradiation

The annealing of the samples irradiated with 23 MeV protons and neutrons (figure 6.15) also shows the typical annealing behavior of p-bulk material, indicating that the neutron irradiation predominantly creates acceptors. This indicates that the space charge sign is not changed by the additional neutron irradiation, as shown in table 6.5.

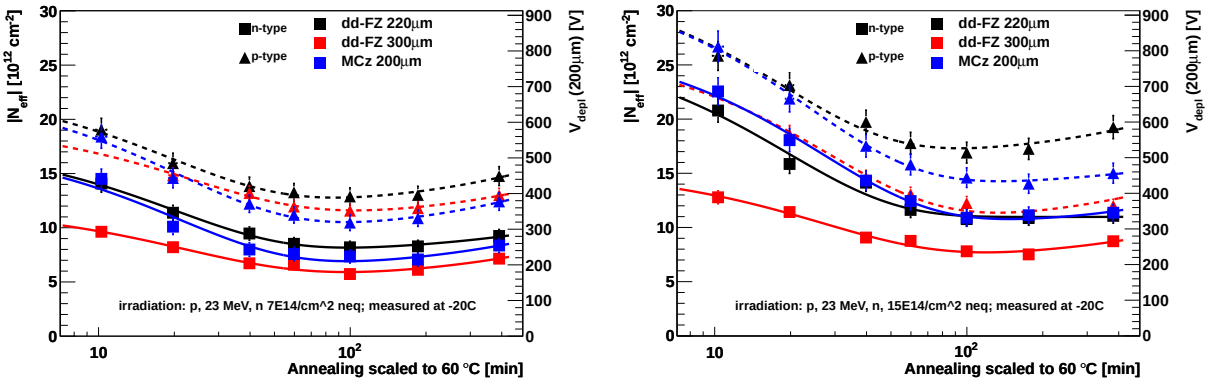

(a) 3 p_M + 4 n irradiation.

(b) 10 p_M + 5 n irradiation.

Figure 6.15: Annealing of the full depletion voltage after mixed p_M + n irradiation. The model parameters of the performed fits are given in section 2 of the appendix.

The short term annealing of the more oxygen rich MCz and dd-FZ220 material and the dd-FZ300P material are similar, while it is weaker than for dd-FZ300 n-bulk material. The long term annealing of the all materials is weak, similar to that of the 23 MeV proton irradiation only.

Development of the stable damage with fluence after 23 MeV proton and neutrons irradiation

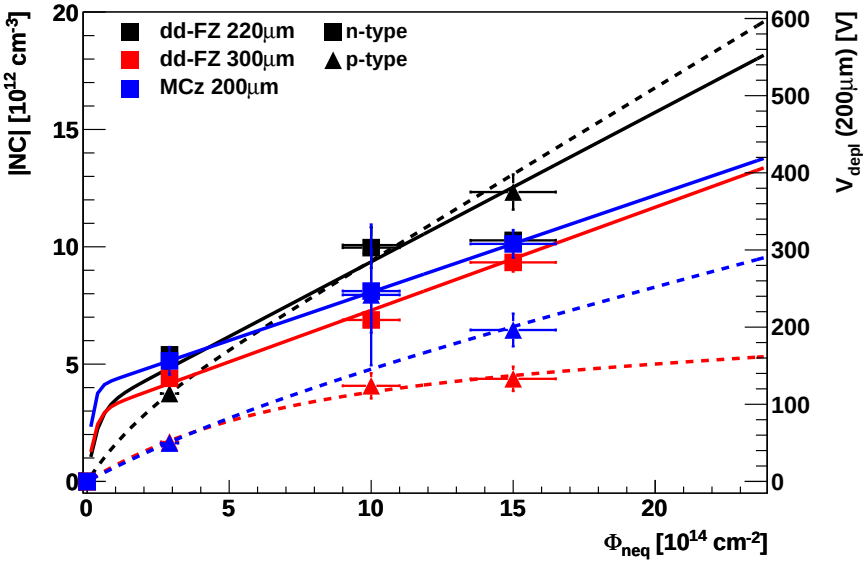

Figure 6.16: $|N_C|$ versus fluence showing only p_M irradiations.

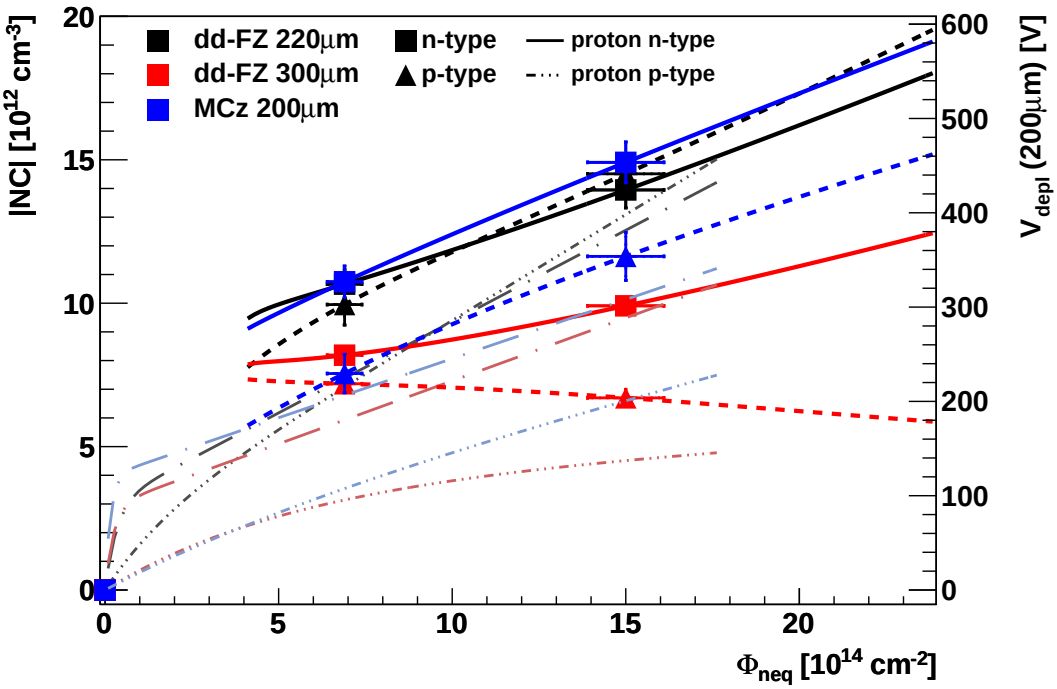

Figure 6.17: $|N_C|$ versus fluence showing p_M + n irradiations. The solid and dashed lines show the fits with the Hamburg model of the mixed irradiation, the dashed-dotted lines show the model of only p_M irradiation. The model parameters of the performed fits are given in section 2 of the appendix.

The stable damage, the part of the damage that is not affected by annealing (see equation 3.21), of the different materials after 23 MeV proton irradiation, is shown in figure 6.16 while the stable damage after mixed 23 MeV proton and neutron irradiation is shown in figure 6.17.
The fits show the stable damage component of the Hamburg model, as described in section 3.4.1. The equation is:

$$N_C = N_{C0}(1 - exp(-c\Phi_{eq})) + g_c\Phi_e q$$

With the damage parameter N_{C0} (describing the final value of the "incomplete donor removal"), the donor removal constant c and the acceptor introduction rate g_c.

The stable damage after 23 MeV proton irradiation After 23 MeV proton irradiation, all n-bulk materials show a strong donor removal, resulting in a steep rise at low fluences and the space charge sign inversion and show a similar acceptor generation.
The p-bulk materials show a strong creation of acceptors in the low fluence range and a reduced acceptor creation in the high fluence region. So either an addition acceptor generation takes place at low fluences (as assumed by the Hamburg model, since it was developed to describe the "donor removal" in n-bulk silicon) or the acceptor creation saturates at higher fluences.
The SCSI is mainly determined via the annealing behavior and sometimes also by TCT measurements. The short term annealing is dominated by the decrease of negative space charge and the long term annealing by the increase of negative space charge. The resulting curve shows first a reduction of $|N_{eff}|$ in the short term and an increase of $|N_{eff}|$ in the long term for p-bulk material and n-bulk material after a SCSI.

The stable damage after 23 MeV proton and neutron irradiation After the mixed 23 MeV proton and neutron irradiation, all n- and p-type materials show a very steep increase at low fluences. At higher fluences the acceptor creation is reduced, probably only due to the reduced neutron fraction so that at very high fluences ($> 25 \cdot 10^{14}\, cm^{-2}$) with a dominant proton part of the irradiation no difference between single proton and mixed irradiation is expected. This effect is the strongest in the dd-FZ300 p-type material, which even shows a reduction of the stable damage towards an increased proton ratio, while after the proton irradiation the damage seemed to nearly saturate.

SCSI	n-bulk	p-bulk
dd-FZ220	✓	–
dd-FZ300	✓	–
MCz200	✓	–

(a) 23 MeV proton irradiation

SCSI	n-bulk	p-bulk
dd-FZ220	✓	–
dd-FZ300	✓	–
MCz200	✓	–

(b) 23 MeV proton and neutron irradiation

Table 6.5: Space charge sign inversion after p_M and p_M + n irradiation.

6.2.5 Annealing of the full depletion voltage and development of the stable damage with 23 GeV proton and neutron irradiation

Annealing of the full depletion voltage after 23 GeV proton irradiation

The FZ200 materials with a medium oxygen concentration show a clear p-bulk annealing behavior with a strong reverse annealing. This leads to the assumption that the FZ200N underwent a space charge sign inversion.
The oxygen rich MCz200 materials show typical n-bulk annealing behavior. This indicates that they did not undergo space charge sign inversion after 23 GeV proton irradiation. The MCz200P material shows a reduced full depletion voltage already after a fluence of $\Phi_{neq} = 3 \cdot 10^{14}\,\mathrm{cm}^{-2}$. With increasing fluences it shows an increasing full depletion voltage with a typical n-bulk annealing behavior, meaning that the introduction of donors is dominant, which leads to a space charge sign inversion. A summary of the SCSI is given in table 6.6.
The short term and long term annealing of the MCz200 materials are less strong than those of the FZ200 materials. The data in figure 6.18 is described using the Hamburg model, discussed

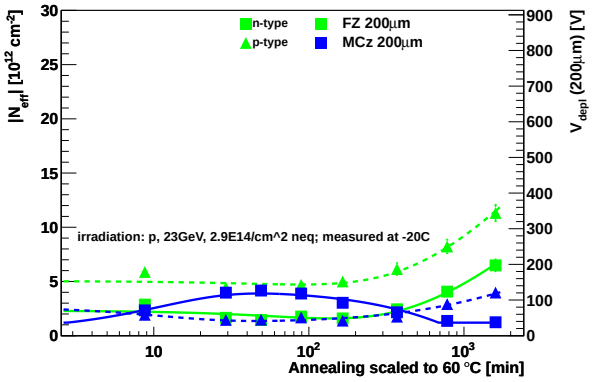

(a) 3 p_G irradiation. Same figure as 6.11a for comparison.

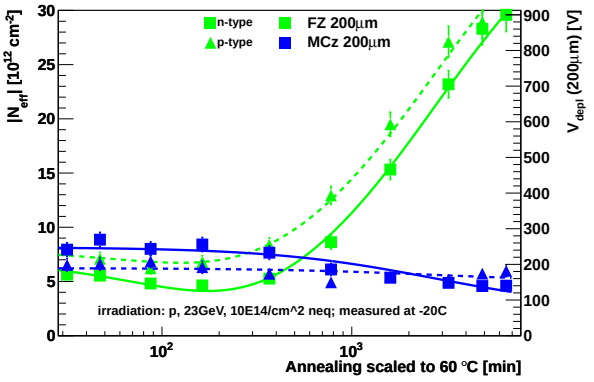

(b) 10 p_G irradiation.

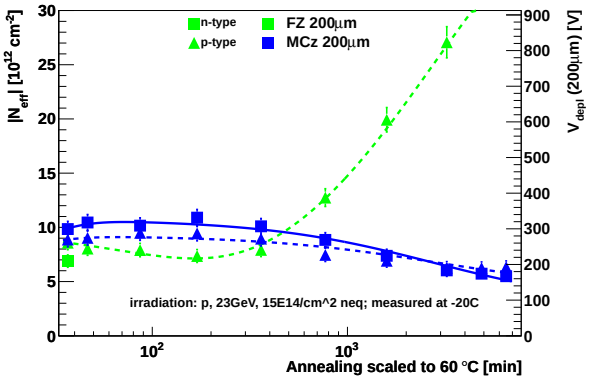

(c) 15 p_G irradiation.

Figure 6.18: Annealing of the full depletion voltage after p_G irradiation. The model parameters of the performed fits are given in section 3 of the appendix.

in section 3.4.1. The parameters for the short term and long term annealing introduction rates and the stable damage are free parameters, the time constants, however, are fixed, due to the small number of data points. The long term annealing time constant after 23 GeV proton irradiation can be found in [55] and [56] for the oxygenated float zone and magnetic Czochralski silicon to be about $\tau_y = 200$ minutes at 80 °C, which corresponds to about $\tau_y = 2740$ minutes at 60 °C. The short term annealing time constants were determined using global fits over all FZ (5) and MCz (6) samples and taking the annealing during irradiation into account. The time constant at 60 °C for the used FZ samples was found to be $\tau_a = 113$ minutes, the time constant for the used MCz samples was found to be $\tau_a = 11.1$ minutes.
The annealing behavior of the materials irradiated with 23 GeV protons is not as clear as that of the 23 MeV proton irradiated materials. This can be explained by the annealing during irradiation at the CERN PS, as described in section 5.2. The irradiation to the highest fluence ($\Phi_{neq} = 15 \cdot 10^{14}\,\mathrm{cm}^{-2}$) took about 6 days and 6 hours at a temperature of about 30 °C. This leads to a superposition of annealing states (see section 5.3.2). The defects which are created in the beginning of the irradiation anneal during the whole irradiation. Those created at the end of the irradiation time do not anneal during irradiation. A superposition of annealing functions was used to describe the annealing of each sample. In figure 6.19 the procedure is shown for only 5 steps, instead of $\mathcal{O}(100)$. Figure 6.19a shows the single annealing curves with a fifth of the total fluence starting at different times, figure 6.19b shows the superpositions of one to all five annealing curves.

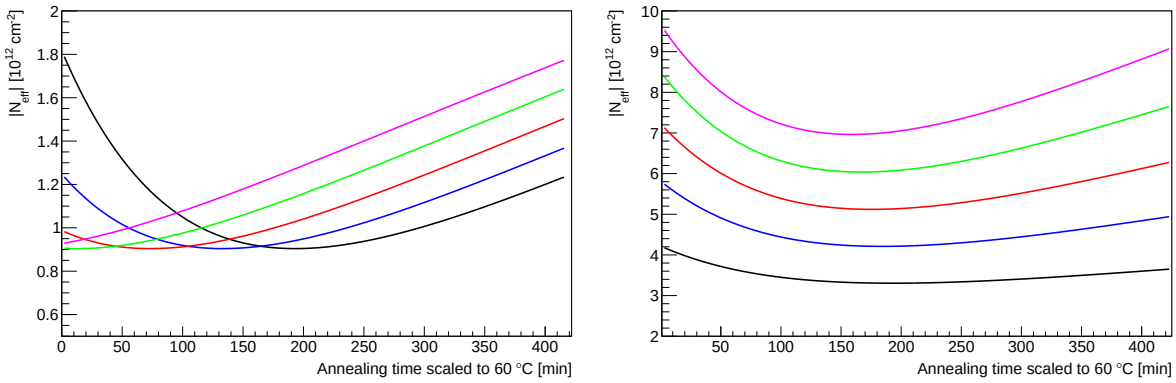

(a) Single curves

(b) Superposition

Figure 6.19: Superposition of single annealing curves due to annealing during the irradiation for the case of the FZ200P sample after 15p$_G$ irradiation.

Annealing of the full depletion voltage after mixed 23 GeV proton and neutron irradiation

The annealing of the full depletion voltage after mixed 23 GeV proton and neutron irradiation is shown in figure 6.20.
The short term annealing of the full depletion voltage after mixed 23 GeV proton and neutron

irradiation shows a p-bulk behavior for the FZ200 and MCz200P materials. The MCz200N, which did not undergo a space charge sign inversion after the single 23 GeV proton irradiation, shows a fluence dependent annealing behavior. After an irradiation with $3{\cdot}10^{14}\,\mathrm{cm}^{-2}$ protons and $4{\cdot}10^{14}\,\mathrm{cm}^{-2}$ neutrons, where the neutron irradiation dominates, the MCz200N material shows a clear p-bulk annealing behavior. At higher fluences with higher proton to neutron ratios, the picture is not as clear.
The long term annealing of the FZ200 material shows the expected increase of the full depletion voltage.
The long term annealing of the MCz200 materials show a stable full depletion voltage at higher fluences instead of the expected increase. This indicates a balancing of acceptors and donors created in different amount in the proton and neutron irradiation. In addition the difference of the full depletion voltage between the MCz200 n-bulk and p-bulk material is very small after the short term annealing. A summary of the SCSI is given in table 6.6.
The small changes in the full depletion voltage after long annealing times for MCz200 materials are beneficial for the operation of the tracking detector, since the needed operating voltage of the sensors is not increasing during long maintenance periods.

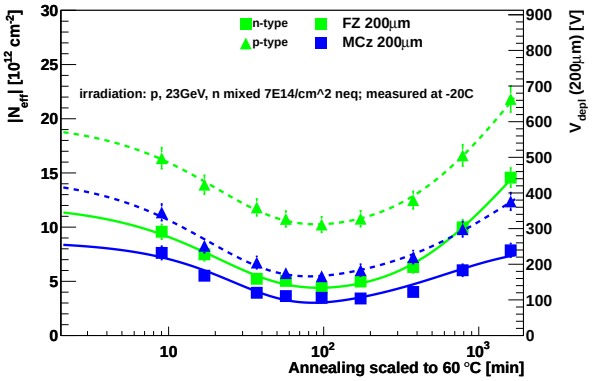

(a) 3 p_G + 4 n irradiation. Same figure as 6.11c for comparison.

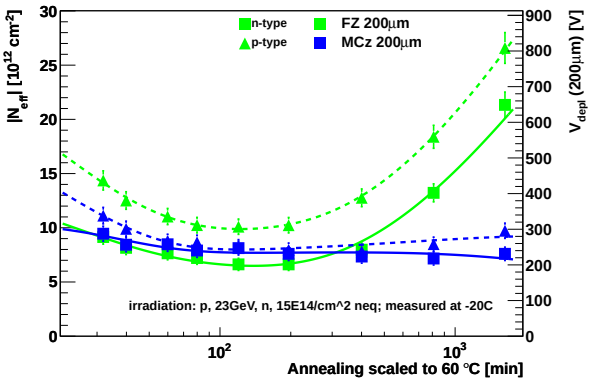

(b) 10 p_G + 5 n irradiation.

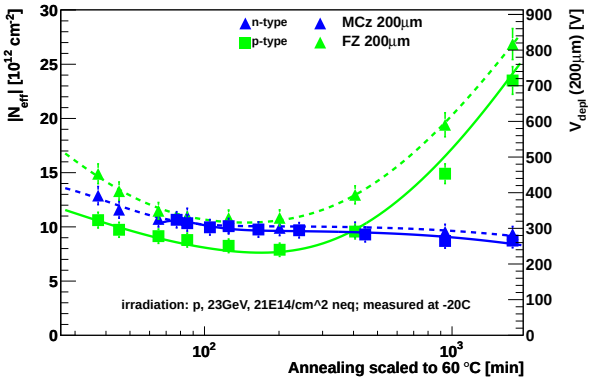

(c) 15 p_G + 6 n irradiation.

Figure 6.20: Annealing of the full depletion voltage after p_G + n irradiation. The model parameters of the performed fits are given in section 3 of the appendix.

Development of the stable damage after 23 GeV proton and neutron irradiation with fluence

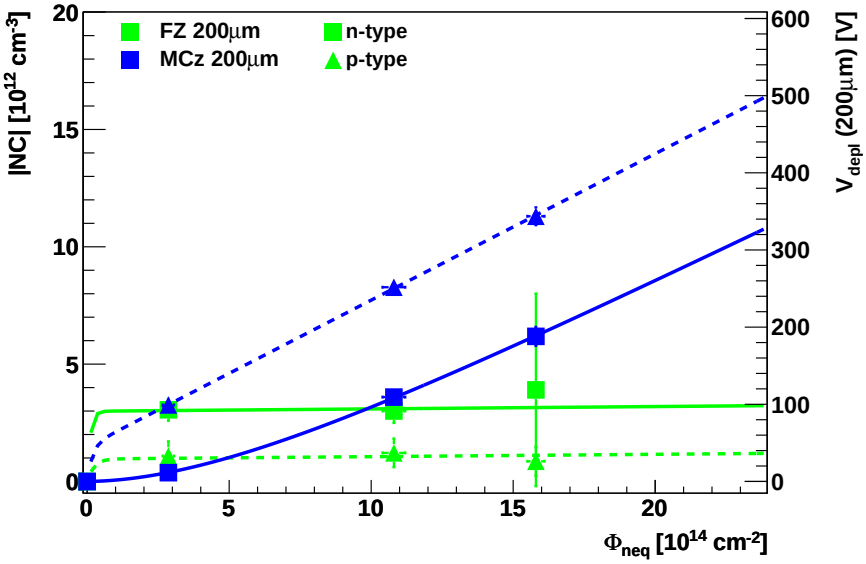

Figure 6.21: $|N_C|$ versus fluence showing only p_G irradiations.

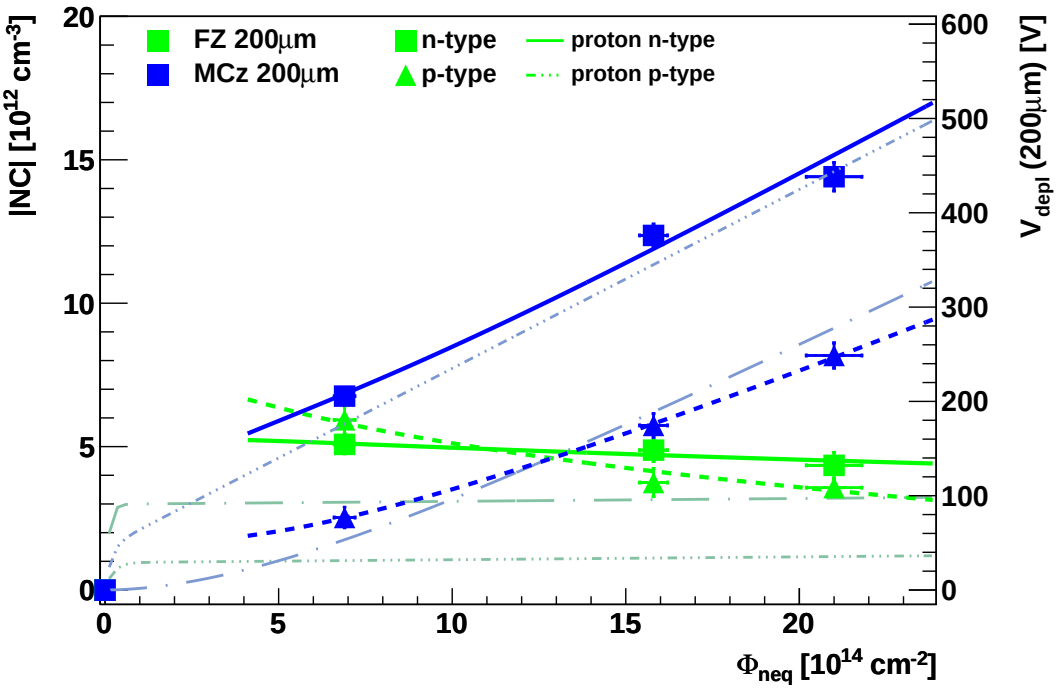

Figure 6.22: $|N_C|$ versus fluence showing p_G + n irradiations. The solid and dashed lines show the fitted Hamburg model of the mixed irradiation, the dashed-dotted lines show the model of only p_G irradiation. The model parameters of the performed fits are given in section 3 of the appendix.

The stable damage after 23 GeV proton irradiation The development of the stable damage N_C with fluence is shown in figure 6.21 for 23 GeV proton irradiation. The FZ200N shows a strong donor removal at low fluences (up to the first measurement point at $\Phi_{neq} = 3 \cdot 10^{14}\,\mathrm{cm}^{-2}$) and no change of stable damage within the errors, once the donor removal is completed. The very steep rise at the low fluence is a result of the fit because it has no handle on the exact rise, since the donor removal is already complete at the first fluence point. The FZ200P is compatible with no change at all, over the full fluence range, also the fit suggests a small acceptor removal at low fluences and a negative slope for higher fluences. This indicates that the oxygen content of the FZ200 material is such, that the creation of donors and acceptors is balanced. This is, however, only true for the stable damage, as the long term annealing is very strong.
The effective creation of donors is the same for the n-type and p-type MCz200 material.

The stable damage after 23 GeV proton and neutron irradiation The development of the stable damage N_C with fluence is shown in figure 6.22 for 23 GeV proton and neutron irradiation. After the additional neutron irradiation the stable damage of both FZ200 materials are increased with respect to the single 23 GeV proton irradiation. The creation of acceptors and donors is not balanced anymore, due to the very strong acceptor creation of neutron irradiation. At very high fluences ($\Phi_{neq} \gg 25 \cdot 10^{14}\,\mathrm{cm}^{-2}$) with a dominant proton part of the irradiation no difference between single proton and mixed irradiation is expected.
The MCz200 materials show the expected compensation of the created donor and acceptor like defects from the proton and neutron irradiations resulting in a reduced full depletion voltage after mixed irradiation with 23 GeV protons and neutrons. The stable damage, however, does not reflect this so much, since the annealing of the mixed irradiation is very weak, which results in a higher stable damage.

SCSI	n-bulk	p-bulk
FZ200	✓	–
MCz200	–	✓

(a) 23 GeV proton irradiation

SCSI	n-bulk	p-bulk
FZ200	✓	–
MCz200	(✓)	(–)

(b) 23 GeV proton and neutron irradiation

Table 6.6: Space charge sign inversion after 23 GeV proton and neutron irradiation, determined from the annealing behavior. The status of MCz200 is unclear for mixed fluences $\geq 1.5 \cdot 10^{15}\,cm^{-2}$.

6.2.6 Summary

In FZ material a similar behavior after 23 MeV and 23 GeV proton irradiation (SCSI for n-bulk materials, a strong long term annealing and nearly constant stable damage with fluence) was observed, while the oxygen rich MCz materials show differences. We conclude that the influence of the proton energy is only relevant for oxygen rich material. A dependence of the materials with a medium or low oxygen content on the energy of the protons could not be found. The proton irradiations in this work use energies on the lower and upper limit of the CMS spectrum (see section 5.2). This has to be kept in mind for the results of the oxygen rich MCz200 materials.

The FZ200 and dd-FZ300 materials with a medium oxygen content in general show a slightly lower increase of full depletion voltage with fluence than the MCz200 materials with a higher oxygen content after single proton irradiation (23 MeV and 23 GeV). At low fluences ($\Phi_{neq} \approx 3 \cdot 10^{14}\,\mathrm{cm}^{-2}$) the n-bulk FZ200 and dd-FZ300 materials do all undergo a space charge sign inversion (SCSI), leading to a lower full depletion voltage of the n-bulk materials than those of the p-type materials.
The behavior of the MCz200 materials differs after irradiations with the different proton energies. After an irradiation with the 23 MeV protons, the n-bulk material undergoes a SCSI, after an irradiation with 23 GeV protons it does not. The behavior of the p-bulk material is reversed (see table 6.7).

SCSI	MCz200 n-bulk	MCz200 p-bulk
23 MeV protons	✓	–
23 GeV protons	–	✓

Table 6.7: Space charge sign inversion of the MCz200 material after proton irradiation.

After the additional neutron irradiation, the FZ200 and dd-FZ300 materials show a strong (p-bulk) or slight (n-bulk) increase of the full depletion voltage at low fluences and a slight increase of the full depletion voltage at higher fluences (with a decreasing neutron ratio).
The MCz200 materials show a similar behavior to the FZ200 and dd-FZ300 materials after a mixed 23 MeV proton and neutron irradiation. After the mixed 23 GeV proton and neutron irradiation, the MCz200 materials show a compensation of changes in the full depletion voltage in the low fluence range. This can be explained by a dominant introduction of positive space charge in proton irradiation that is compensating the dominant negative space charge introduction in neutron irradiation. After the short term annealing, that is similar for all irradiation types and materials, the long term annealing of the FZ200 and dd-FZ300 materials is very strong. The long term annealing of the MCz200 materials after 23 GeV proton and neutron irradiation reduces the full depletion voltage, which is very beneficial for the operation of the CMS tracker.

Charge collection in pad and strip sensors

7.1 Charge collection in pad sensors

Charge collection in pad sensors is different than charge collection in segmented sensors. Pad sensors are good structures to study bulk effects without the influence of the field distortion due to strips or pixels. In the thesis of T. Pöhlsen [34], the charge collection of pad sensors after single proton and neutron irradiation and first measurements of mixed irradiation using 23 MeV protons and neutrons was discussed. All pad sensor measurements were performed using the TCT with charge induced with an infrared laser. In figures 7.1 and 7.2 important results of this discussion are shown.

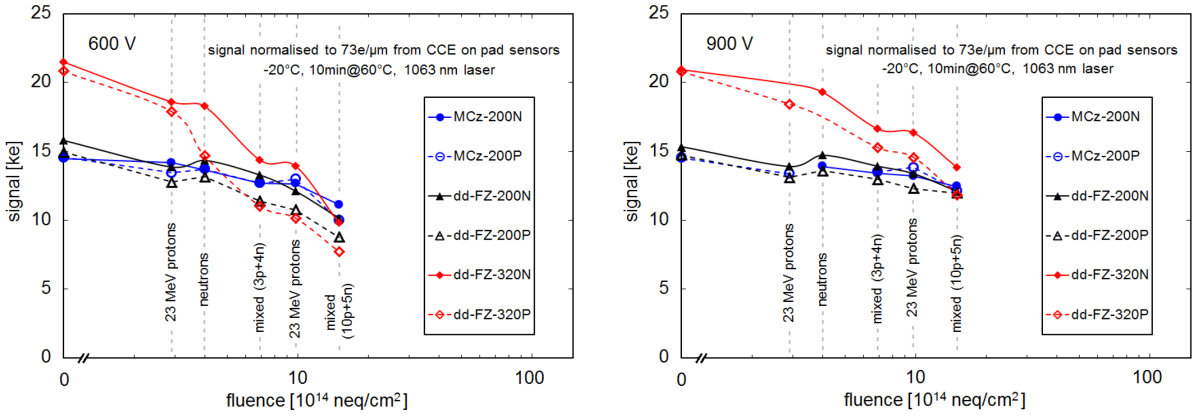

(a) p_M, n and p_M + n irradiation, 600 V.

(b) p_M, n and p_M + n irradiation, 900 V.

Figure 7.1: The charge collection of pad sensors after 23 MeV proton, neutron and mixed irradiations after an annealing of 10 minutes at 60 °C, for two different voltages. The charge collection is calculated from the charge collection efficiency measured with TCT using a charge of 73 electrons per µm for CCE = 1. Figure taken from [34].

An important statement was that the bulk material only contributes to the changes in CCE via the electric field, not via the trapping: At a bias voltage below the full depletion voltage, the collected charge is a strong function of bias voltage and the CCE is different for p- and n-type doped sensors as well as for FZ and MCz. In contrast, at bias voltages above the full depletion voltage the CCE is similar for all materials and for p- and n-type.
The thickness of the sensors has a big influence on the signals, since more charge is produced in a thicker sensor, but higher bias voltages are needed to fully deplete it and the trapping probability of charge carriers is increased. This leads to a higher charge for thicker sensors at

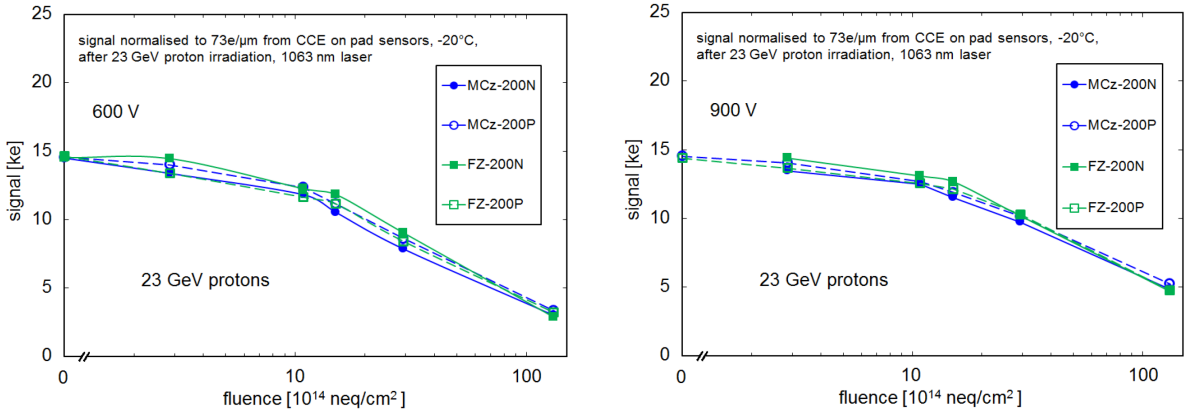

(a) p_G irradiation, 600 V. (b) p_G irradiation, 900 V.

Figure 7.2: The charge collection of pad sensors after 23 GeV proton irradiations with no additional annealing, for two different voltages. The charge collection is calculated from the charge collection efficiency measured with TCT using a charge of 73 electrons per µm for CCE $= 1$. Figure taken from [34].

low fluences. At higher fluences, howerever, when the thick sensors have a high full depletion voltage, the collected charge is reduced if the sensor is under-depleted.

7.1.1 Charge collection after irradiation with 23 MeV protons and neutrons

Figure 7.3 shows the collected charge of samples irradiated with 23 MeV protons and neutrons, the same as shown in figure 7.1, but now after 90 minutes annealing at 60 °C. This annealing time is at either the approximate maximum or minimum of the annealing curve and a common annealing time to compare values.
The annealing reduces the full depletion voltage which leads to a higher charge collection compared to the one shown in figure 7.1, especially for the dd-FZ300 materials at a bias voltage of 600 V.

7.1.2 Charge collection after irradiation with 23 GeV protons and neutrons

The collected charge after 23 GeV proton and neutron irradiation and 90 minutes at 60 °C is shown in figure 7.4. The picture is similar to the situation after 10 minutes at 60 °C which was discussed in [34] and is shown in figure 7.2. The bulk doping and material only contribute via the full depletion voltage to the charge collection.

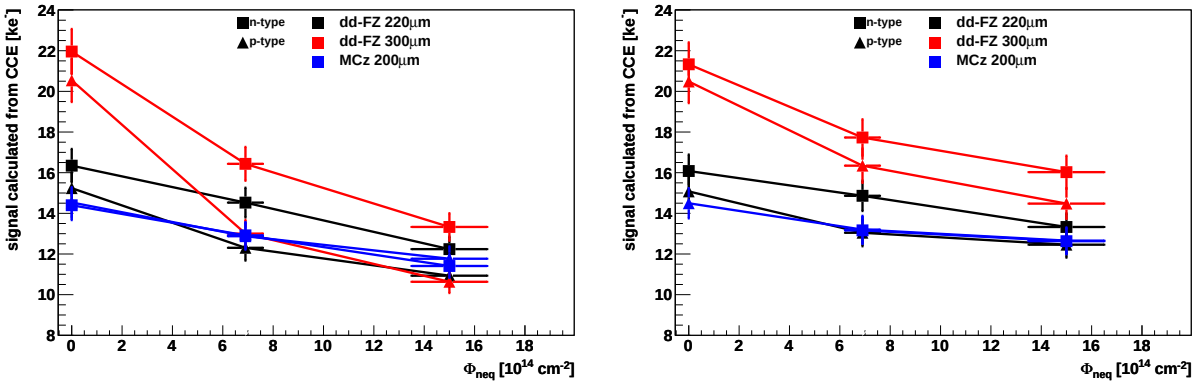

(a) Bias voltage of 600 V. (b) Bias voltage of 900 V.

Figure 7.3: Charge collection of pad sensor versus fluence after p_M + n irradiation and 90 minutes annealing at 60 °C after the second irradiation. The charge collection is calculated from the charge collection efficiency measured with TCT using a charge of 73 electrons per µm.

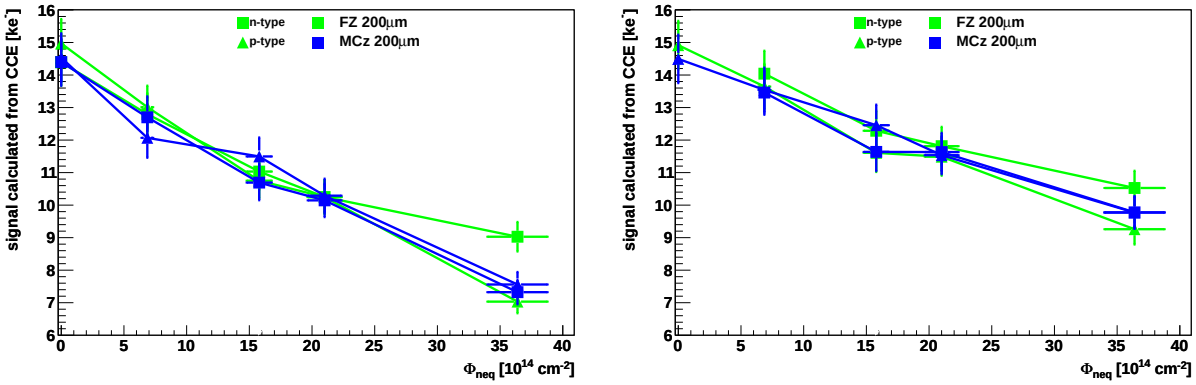

(a) Bias voltage of 600 V. (b) Bias voltage of 900 V.

Figure 7.4: Charge collection of pad sensor versus fluence after p_G + n irradiation and 90 minutes annealing at 60 °C after the second irradiation. The charge collection is calculated from the charge collection efficiency measured with TCT using a charge of 73 electrons per µm.

At fluences $\Phi_{neq} \leq 2.1 \cdot 10^{15}\,\mathrm{cm}^{-2}$ all materials show similar charge collection efficiencies within the uncertainties. At the highest fluence of $\Phi_{neq} = 3.6 \cdot 10^{15}\,\mathrm{cm}^{-2}$ the higher full depletion voltage of the MCz200 materials compared to the FZ200 materials is clearly visible, especially in the charge collection at 600 V. The full depletion voltages after 30 p_G and 7 n irradiation determined from C/V measurements are 450 V for the FZ200N, 540 V for the FZ200P and about 600 for both MCz200 materials. See also figure 7.6 where the voltage dependence of the CCE is shown.

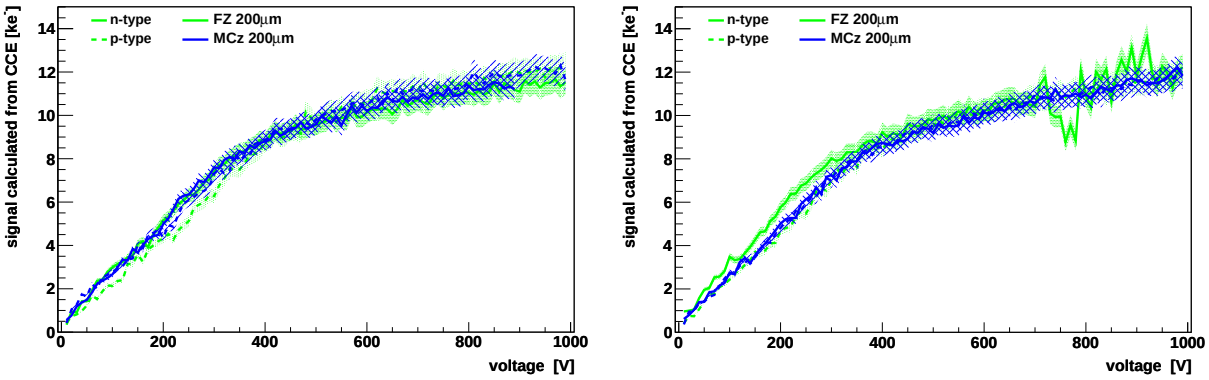

(a) Annealing of 10 minutes at 60 °C.

(b) Annealing of 90 minutes at 60 °C.

Figure 7.5: Charge collection of pad sensor versus voltage after 15 p_G + 6 n irradiation. The given annealing times start after the second irradiation. The charge collection is calculated from the charge collection efficiency measured with TCT using a charge of 73 electrons per µm.

Charge collection versus voltage

In figure 7.5, the charge collection of pad sensors versus voltage after an irradiation with $\Phi_{neq} = 1.5 \cdot 10^{15}\,\mathrm{cm}^{-2}$ 23 GeV protons and $6 \cdot 10^{14}\,\mathrm{cm}^{-2}$ neutrons is shown for an annealing of 10 minutes and 90 minutes at 60 °C after the second irradiation. The kink at about the full depletion voltage is clearly visible at ≈ 350 V. Below full depletion voltage, the effective thickness of the sensor increases with an increase of the bias voltage. At voltages above the full depletion voltage the amount of collectable charges stays constant, however, a part is trapped and does not fully contribute to the signal. The trapping probability can be reduced by increasing the bias voltage, since the trapping probability depends on the electrical field.
Therefore it is recommended to use a bias voltage that is at least equal to the full depletion value.
In figure 7.6, the charge collection of pad sensors versus voltage after an irradiation with $3 \cdot 10^{15}\,\mathrm{cm}^{-2}$ 23 GeV protons and $7 \cdot 10^{14}\,\mathrm{cm}^{-2}$ neutrons is shown for an annealing of 10 minutes and 90 minutes at 60 °C after the second irradiation. As already visible in figure 7.5 after 90 minutes annealing at 60 °C, the full depletion voltage of the FZ200N is lower than that of the other materials. This result is also reflected in figure 7.4.

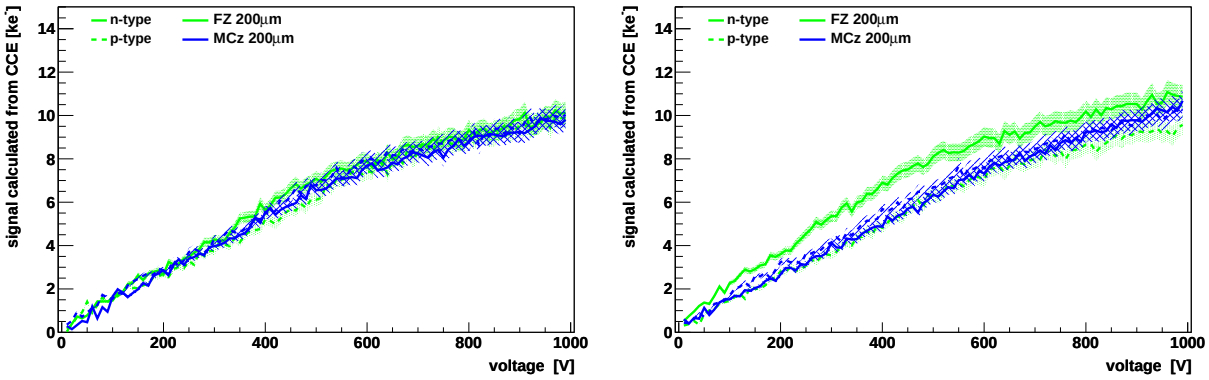

(a) Annealing of 10 minutes at 60 °C.

(b) Annealing of 90 minutes at 60 °C.

Figure 7.6: Charge collection of pad sensor versus voltage after 30 p_G + 7 n irradiation. The given annealing times start after the second irradiation. The charge collection is calculated from the charge collection efficiency measured with TCT using a charge of 73 electrons per µm.

7.2 Comparison of the charge collection in pad and strip sensors

The pad sensor with its simple structure and its approximation of one dimensional electric and weighting potentials is a good sample to study bulk properties of silicon. A comparison of measurements in pad sensors and strip sensors is useful to disentangle effects due to the segmentation from effects of the bulk.
The segmentation changes the shape of the electric and weighting potentials, so that the one dimensional approximation of the potentials is not valid anymore and thus can have an impact on the charge collection. A typical weighting potential of a strip sensor is shown in figure 7.7. The weighting potential gives the coupling of a given test charge to the readout strip. It can be used to calculate the induced current at the readout. According to [57] and [58] it is given by:

$$i = E_w \cdot q \cdot v$$

with the induced current i, the weighting field E_w in direction of the movement v of the charge q. This results in an induced charge at the given readout of:

$$Q_i = q(\Phi_w(e) - \Phi_w(s))$$

with the induced charge Q_i, the moving charge q and the weighting potentials Φ_w at the start position s and the end position e.
Since the induced charge typically distributes over several strips, only a fraction of the signal is seen if only some strips are read out, while in a pad sensor the whole charge is measured. We expect that the pad sensor signal is the upper limit to the strip signal, at least in conditions where no charge multiplication in high field regions takes place and no strips contribute with significant negative signals, which was observed only in one case. It is assumed that it is possible to reach the pad sensor signal if enough strips contribute to the signal.

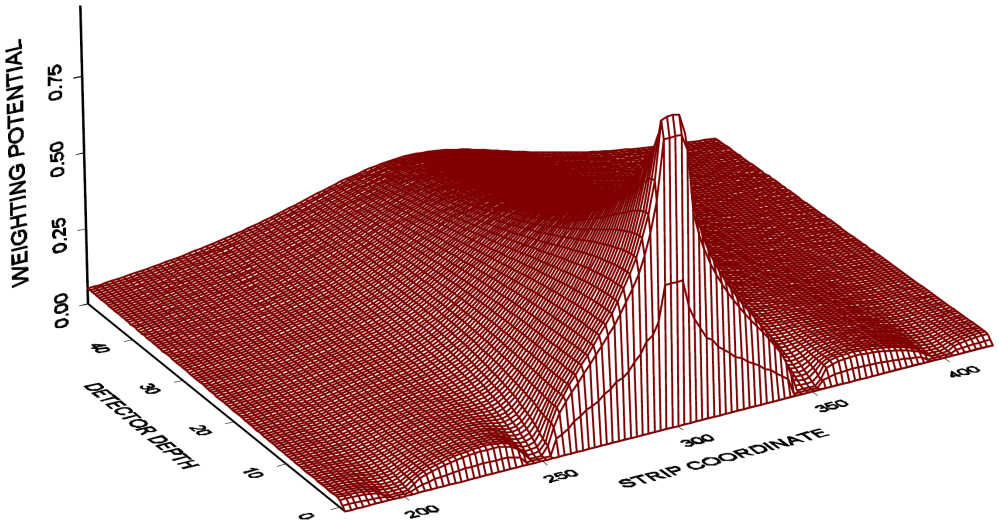

Figure 7.7: Weighting potential of a strip sensor with a thickness of 300 µm and a strip pitch of 50 µm. The read-out strip is at the coordinate 300. Figure taken from [59].

7.2.1 Charge collection and clusterfinding efficiencies versus voltage for irradiated and non-irradiated samples

Clusterfinding algorithms

The data shown in the following is based on different cluster finding algorithms, discussed in detail in section 4.3.5. A short reminder is given here:

- **"no cut"**: builds a cluster around the strip with the highest signal of a defined width (typically 1 to 5 strips). The aim is to find the considered events (without events where the timing was wrong or the particle did not pass through the sensitive part). It works without artificial cuts on the signal height and thus collects the full signal when given enough used strips, e.g. four. It is also to used determine the signal that is collected by the seed with a clustersize set to one strip.

- **"5σ/2σ cut"**: uses a 5σ cut on the seed signal and 2σ cuts on the neighbors. The aim is to make the comparison to older data possible, since it is a widely used cluster cut for analogue readout. It is able to collect nearly the full signal if the noise is low enough, since only one strip has to be above a high threshold and neighbors are accepted more easily.

- **"fixed threshold cut"**: uses a fixed threshold to determine an estimation of the found clusters in the future binary readout of CMS. Here a threshold of 6000 e^- is used. However, thresholds ranging from 4000 to 8000 e^- are under discussion right now.

Calibration

The ALiBaVa system is calibrated using an internal calibration pulse, as described in section 4.3.5. This procedure could not be validated with an precise external calibration measurement. However, the obtained signal height is compatible with the expected value of $15700 \pm 400\,e^-$ for non-irradiated sensors of 200 µm thickness.
It is assumed, that the scale of the measurements has an uncertainty of $\pm 500\,e^-$, while the uncertainty within the measurements of one sample is smaller ($\mathcal{O}(50\,e^-)$). In the figures only the statistical error is given.

Collected charge

All strip sensor measurements were performed using ALiBaVa and charge induce by β-particles. The collected charge and efficiency of finding clusters for an irradiated and non-irradiated sensor are shown in figure 7.10. For a better comparison with existing data, the most probable value (MPV) of a Landau function that is convoluted with a Gaussian is shown. This function describes the pulse height distribution well, if the full signal is collected (see figure 4.25).
In the topp row of figure 7.10, the collected charge of non-irradiated samples (7.10a) and irra-

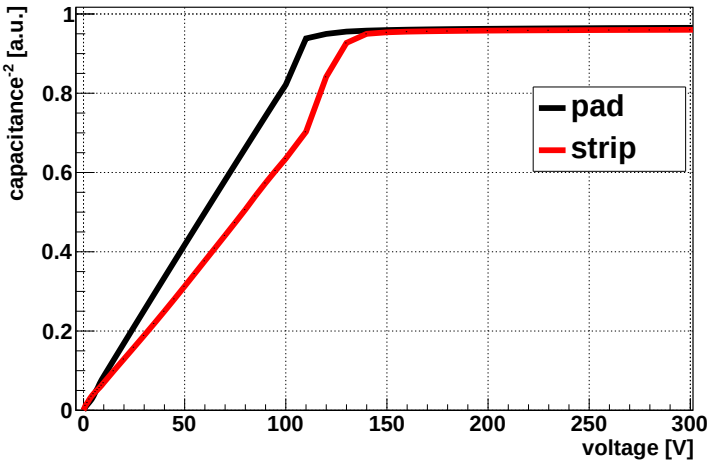

Figure 7.8: Capacitance vs. voltage characteristic for a FZ200P strip and pad sensor.

diated samples (7.10d) is shown. The charge collected by the "no cut" cluster finding algorithm is similar to the charge collected by a pad sensor. However, slightly higher voltages are needed to obtain the same signal, which means that the full depletion voltage is increased (see figure 7.8). This is caused by the segmentation: a higher bias voltage is needed to also deplete the region between the strips.
The "$5\sigma/2\sigma$ cut" shows a slightly reduced signal, which is expected due to small signals ($< 2\sigma$) on neighboring strips that are not included in the cluster and thus do not contribute to the signal.
The "fixed threshold cut" shows a significantly reduced signal, since it mostly consists only of the seed and sometimes the seed and a high neighbor.

Finally the seed only of the "no cut" algorithm shows the lowest signal, since only one strip is taken into account and any charge shared with other strips is lost.
So in this case, the signal collected by the pad sensor is similar to the signal of the "no cut" four strip cluster and the other algorithms show a lower signal.
In figure 7.9, charge distributions obtained with the different algorithms are shown for 75 V (below full depletion voltage) and 150 V (above full depletion voltage). All distributions show a Landau-like distribution convoluted with a Gaussian. However, the distributions above full depletion are broadened and have a higher MPV, compared to those below full depletion. The "fixed threshold cut" algorithm shows an abrupt drop of entries in the case below full depletion voltage. This is caused by the used threshold of 6000 e^-.

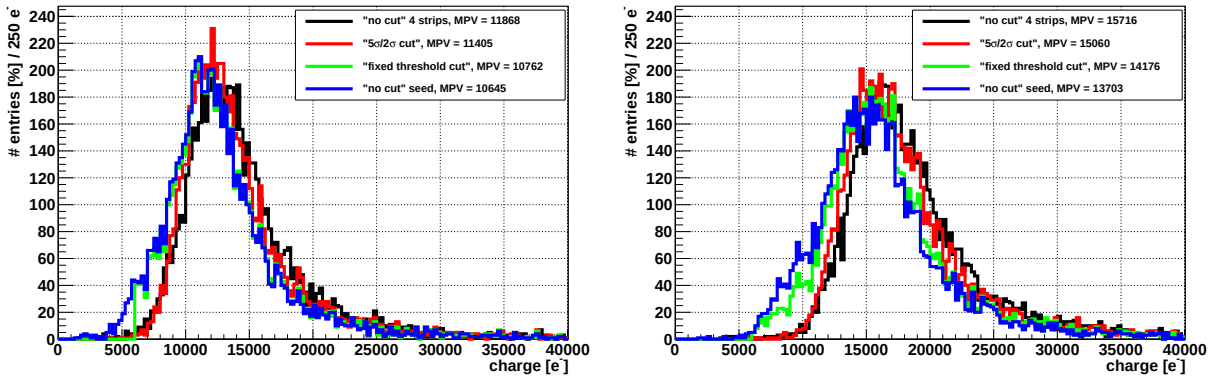

(a) Bias voltage of 75 V.

(b) Bias voltage of 150 V.

Figure 7.9: Charge distribution created using different cluster finding algorithms. Figure (a) shows the distributions below full depletion voltage and figure (b) above the full depletion voltage of the non-irradiated FZ200Y strip sensor also shown in figure 7.10.

Cluster finding efficiency

The cluster finding efficiency is determined by dividing the number of clusters found by a given algorithm by the number of expected clusters. This expectation is stable for a given geometrical configuration (source position, number and position of used readout strips) and is determined once at a voltage high enough to separate noise and signal events.
Since the "no cut" algorithm depends on this estimation, its cluster finding efficiency is 100 % by definition.

The efficiency of cluster finding by both the "$5\sigma/2\sigma$ cut" and "fixed threshold cut" algorithms is shown for the non-irradiated and the irradiated case in figure 7.10b and 7.10e respectively. In the non-irradiated case the efficiency reaches > 97 % already at 100 V which is below the full depletion voltage, corresponding to a collected charge of 9 ke^- for the "$5\sigma/2\sigma$ cut" and 11 ke^- for the "fixed threshold cut". Since the cluster is found if a seed strip reaches 5 times the noise

(about 4 ke^-) by the "$5\sigma/2\sigma$ cut" algorithm, it is expected to find more clusters at lower signals than the "fixed threshold cut" with a threshold of 6 ke^-. In the irradiated case the efficiency is drastically reduced at low voltages. However, at higher voltages the "$5\sigma/2\sigma$ cut" reaches $> 97\,\%$ at $\approx 600\,V$ and a signal of $\approx 11\,ke^-$, while for the "fixed threshold cut" 1000 V are needed to reach $\approx 96\,\%$ with a signal of $\approx 10.5\,ke^-$.
We conclude that the cluster finding efficiency depends strongly on the used threshold and the charge that is collected by the seed.
The seed signal is reduced compared to the deposited charge for two reasons: the total charge collected is reduced due to trapping and the sharing of the charge between the strips. While the total charge that can be collected can be determined with pad sensors, the charge sharing depends on a variety on factors, among which are the following:

- coupling and inter strip capacitances,
- angle of the passing particle,
- Lorentz angle (drifting charges are diverted by a magnetic field),
- accumulation and inversion layers between the strips.

In the used β-test stand the angle of the passing particles is symmetric around 0°, varying between -7° and $+7^\circ$. In our measurements, though, the Lorentz angle effect can be neglected, since no external magnetic field is applied.
The dependence of the cluster finding efficiency on the used threshold is shown in figure 7.10c for the non-irradiated and figure 7.10f for the irradiated case at a fixed bias voltage of 600 V. In the non-irradiated case with a signal of $\approx 14.5\,ke^-$, the efficiency is stable up to a threshold of $\approx 6.5\,ke^-$ before it starts to drop slowly. This is caused by the broad distribution (see figure 7.9), with entries starting at values well below the MPV. In the irradiated case with a signal of $\approx 8.5\,ke^-$ the efficiency is stable up to a threshold of $\approx 3\,ke^-$ before it starts to drop.

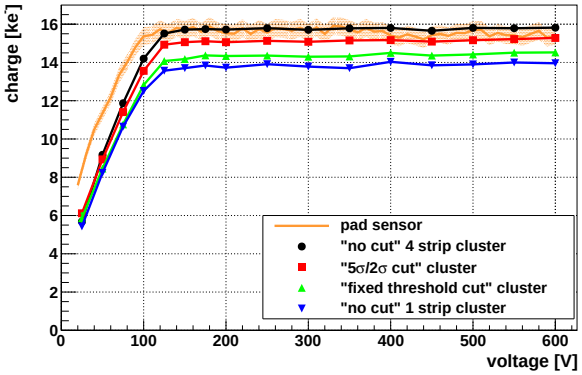

(a) Collected charge, non-irradiated

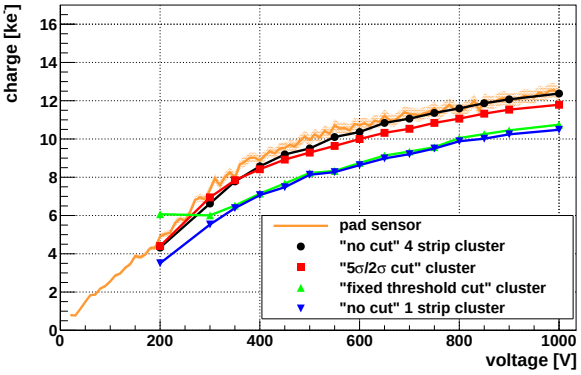

(d) Collected charge, irradiated

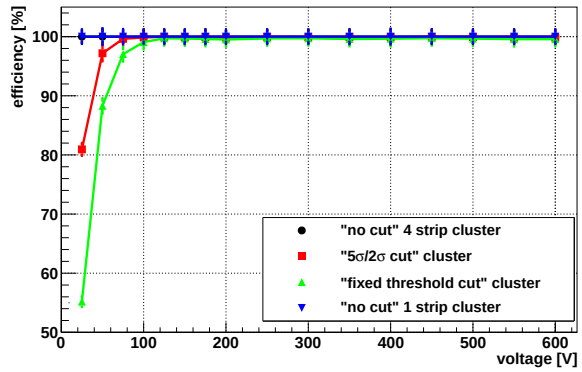

(b) Cluster finding efficiency, non-irradiated

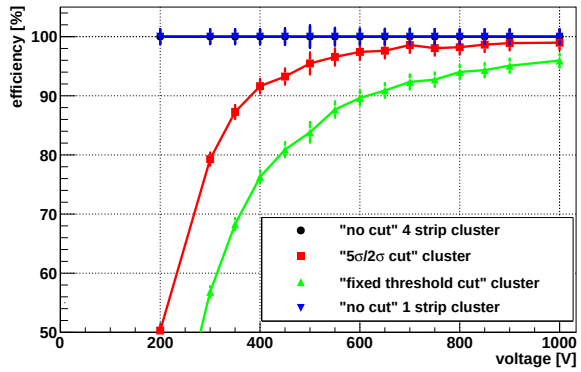

(e) Cluster finding efficiency, irradiated

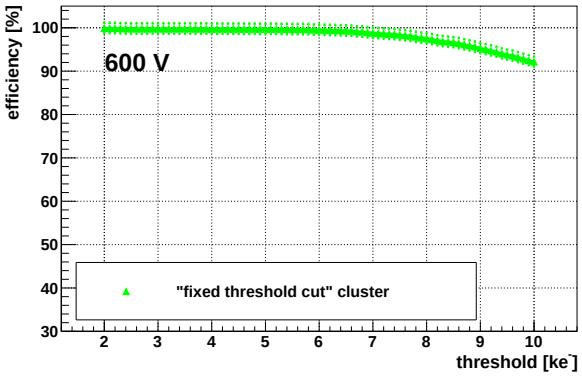

(c) Cluster finding efficiency - threshold scan at 600 V, non-irradiated

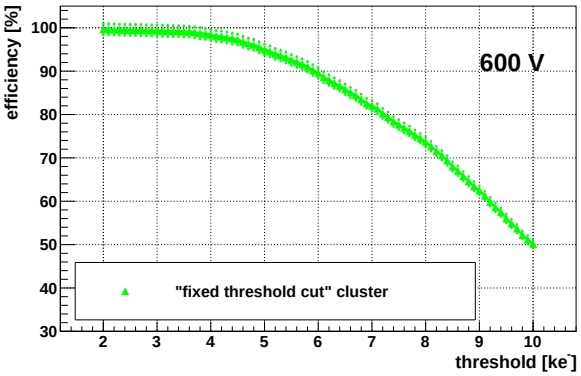

(f) Cluster finding efficiency - threshold scan at 600 V, irradiated

Figure 7.10: Charge collection and cluster finding efficiency with different cluster finding algorithms with voltage and a threshold scan for the "fixed threshold cut" cluster algorithm for a non-irradiated FZ200Y strip sensor (figures (a) to (c)) and after 15 p_G + 6 n irradiation (figures (d) to (f)).

7.2.2 Comparison of strip and pad sensor signals at two different annealing times

A comparison of pad sensor signals and strip sensor signals for a high and a low annealing time is shown in figure 7.11. In the case of the low annealing time (10 minutes at 60 °C) the four strip cluster signal is always higher than the seed signal of the strip sensor, but below the signal of the pad sensor. This difference is very pronounced for higher voltages, but at low voltages the four strip cluster signal still stays higher than the seed signal.

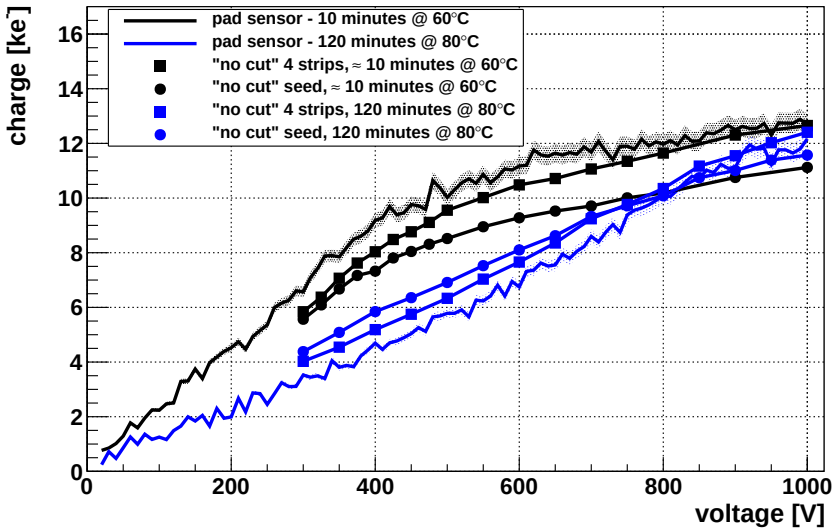

Figure 7.11: Comparison between strip and pad signal after a low and high annealing time for FZ200P sensors after 15 p_G and 6 n irradiation. The charge collection is calculated from the charge collection efficiency measured with TCT using a charge of 73 electrons per µm.

In the case of the high annealing time (120 minutes at 80 °C) the four strip cluster signal is below the seed signal at lower voltages but above the pad sensor signal. At high voltages ($\geq$ 800 V) the four strip signal is comparable to the pad signal and the seed drops below the four strip cluster signal.

In both cases the four strip cluster signal is located between the pad and the seed signal (at least for voltages below $\leq$ 800 V). This indicates that the signal of the segmented sensor can be reached if enough strips contribute to the cluster.
However, in the second case (120 minutes at 80 °C) at lower voltages a high number of strips (>1) is not beneficial. The reduced signal of the four strip cluster compared to the seed, which is only observed at relatively low voltages below the full depletion for the measurement after 120 minutes annealing at 80 °C, can be explained by a low field region in the bulk. While the electrons are collected at the seed and inducing a negative signal there, they induce a positive signal in the neighboring strips. This is usually balanced by a negative signal of the holes drifting towards the backside. But if the holes are trapped on their way to the backside, due to

a region with a low electric field, the charge induced by the holes is reduced. This leads then to a reduced signal in a cluster of four strips compared to the seed only signal. At higher voltages ($\geq 800\,\mathrm{V}$) this trapping of holes is reduced and the neighboring strips start to contribute to the cluster signal in the right direction.

7.2.3 Annealing of the charge collection of irradiated strip sensors

The collected charge of the full cluster and the seed only, as well as the cluster finding efficiency at different thresholds is shown in figure 7.12. The left column (figures (a) to (c)) shows data of a FZ200Y sensor and right column (figures (d) to (f)) shows data of a FZ200P sensor. Both sensors are irradiated to a fluence of $1.5 \cdot 10^{15}\,\mathrm{cm}^{-2}$ 23 GeV protons and $6 \cdot 10^{14}\,\mathrm{cm}^{-2}$ neutrons.

The collected charge of a four strip cluster is shown in the top row. For the FZ200Y sensor (figure (a)) the full depletion voltage voltage is shifted to lower values with annealing, which is also observed for the pad sensor measurements (see section 6.2.5) for the shown annealing times. However, the annealing effect of the strip sensor is stronger than that of the corresponding pad sensor. The annealing is also visible for the FZ200P sensor (figure (d)), where only the measurement directly after irradiation and high annealing times are available (note that 156 minutes at 60 °C corresponds to 15 minutes at 80 °C). The strong increase of the saturation voltage with high annealing times is similar to that of the corresponding pad sensors with a full depletion voltage of $\approx 820\,\mathrm{V}$ after 120 minutes annealing at 80 °C.

In the middle row the collected charge of the seed only is shown. The measurements of the FZ200Y sensor (b) show a band of many measurements with different annealing times and a reduced signal for the first two measurements, similar to the four strip cluster shown in (a).

In figure (e), only the first two measurements (as irradiated and 20 minutes annealing at 80 °C) of the FZ200P sensor show the same behavior as the FZ200Y sensor (at low annealing times). The measurement after 30 minutes annealing at 80 °C shows an increased seed signal for the first measurement points, up to 700 V and then drops to the level of the measurement after 20 minutes annealing at 80 °C. The measurements at higher annealing times both show a higher seed signal than usual, the one after 120 minutes annealing at 80 °C has got an even higher seed signal than the full cluster. This will be discussed in more detail in the following chapter.

The bottom row shows the efficiency of cluster finding at 600 V for both sensors. They both reflect the spread of the seed signal and show an efficiency of $> 97\,\%$ for a threshold of $4\,\mathrm{ke}^-$, but only 65 % to 80 % for a threshold of $8\,\mathrm{ke}^-$. In order to be able to run at a maximum voltage of 600 V, a threshold in the order of $4\,\mathrm{ke}^-$ would be needed. In addition particles, passing at higher angles and a magnetic field will increase the charge sharing and also reduce the efficiency further.

The influence of the Lorentz angle and higher angles of passing particles are also studied in this campaign (See [60]).

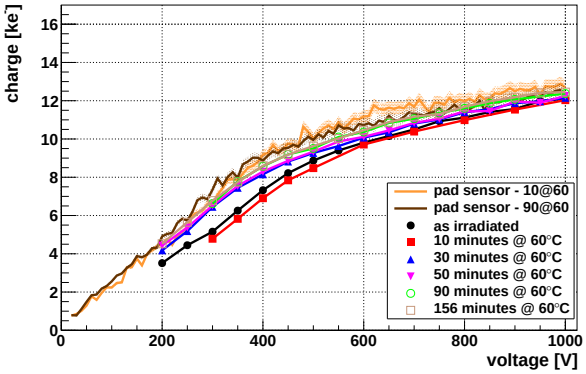

(a) Four strip cluster charge of a FZ200Y sensor

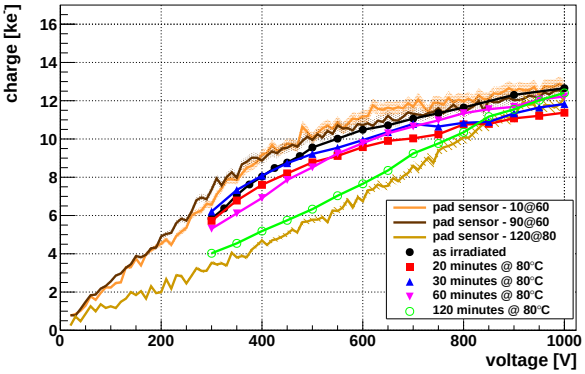

(d) Four strip cluster charge of a FZ200P sensor

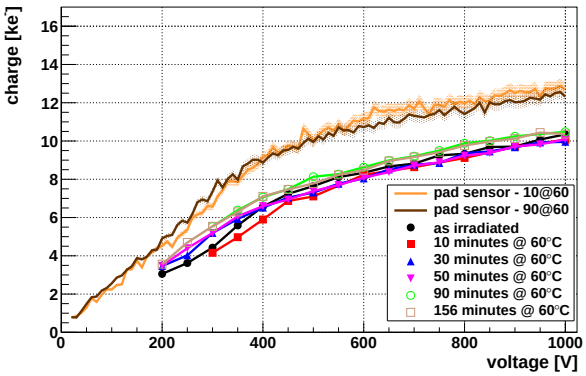

(b) Seed cluster charge of a FZ200Y sensor

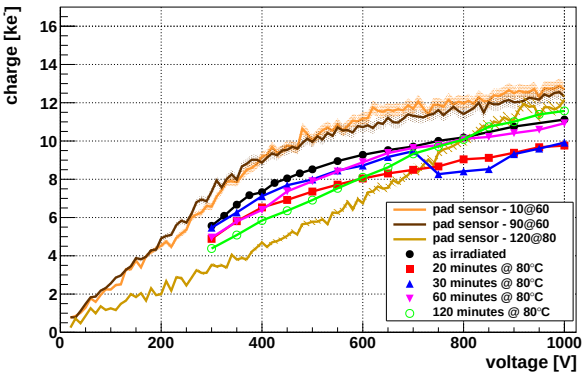

(e) Seed cluster charge of a FZ200P sensor

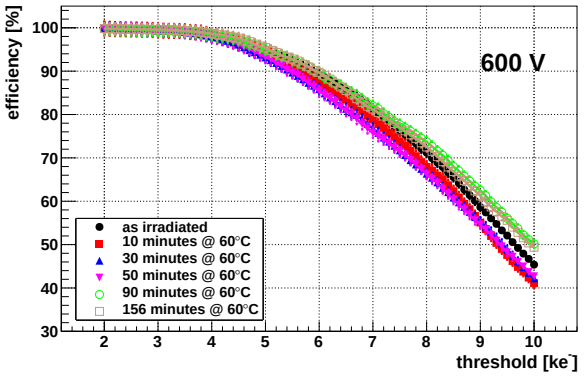

(c) Cluster finding efficiency - threshold scan at 600 V of a FZ200Y sensor

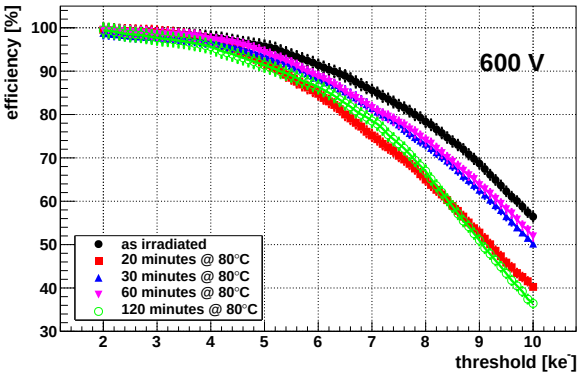

(f) Cluster finding efficiency - threshold scan at 600 V of a FZ200P sensor

Figure 7.12: Charge collection of clusters found with the "no cut" algorithm using four strips (top row) and seed only (middle row) of irradiated strip sensors versus voltage at different annealing times. The pad sensor signal is only shown for comparison. The bottom row shows threshold scans for the "fixed threshold cut" cluster algorithm. Figures on the left show a FZ200Y sensor (figures (a) to (c)) and on the right show a FZ200P sensor (figures (d) to (f)). The sensors are irradiated with 15 p_G + 6 n.

Charge distributions

The signal distributions of the FZ200P sensor are shown in figure 7.13 at 600 V and 800 V for different annealing times. The voltages were chosen in such way, that the lower one is below the signal drop of the measurement after 30 minutes at 80 °C and the higher is above the signal drop.
The charge distributions of the four strip cluster are shown in the top row. All show the expected distribution that follows a Landau convoluted with a Gaussian distribution with different MPVs, depending on the annealing and therefore on the full depletion voltage. The Landau-Gauss fits are omitted for better readability of the figures.
The charge distributions of the seed only are shown in the middle row. At 600 V the measurement as irradiated, after 30 minutes annealing at 80 °C and after 120 minutes annealing at 80 °C show a similar distribution, only with a shifted MPV. The measurement after 20 minutes annealing at 80 °C, however, shows a slightly broadened distribution.
At 800 V, only the measurements as irradiated and after 120 minutes annealing at 80 °C show the usual slim distribution. The two intermediate measurements show a slightly broadened distribution after 20 minutes and a stronger broadened distribution after 30 minutes of annealing at 80 °C.
This change in distribution of the measurement after 30 minutes annealing at 80 °C coincides with the jump of the MPV of the measurement after 30 minutes annealing at 80 °C at 750 V in figure 7.12e.
The distributions in the bottom row show the corresponding η distributions. η is defined in [61] as

$$\eta = \frac{PH(R)}{PH(R) + PH(L)}$$

with $PH(R)$ the signal (pulse height) of the right strip and $PH(L)$ the signal of the left strip where the two strip cluster consists of the seed and the highest neighbor. The η distribution gives a measure of the charge sharing, the crosstalk and the noise of a strip sensor.

The broadening of the seed distributions is reflected in the η distributions by an increase of entries in the center of the distribution ($0.2 < \eta < 0.8$) . The change of the measurement after 30 minutes annealing at 80 °C between 600 V and 800 V is reflected strongly in the increase of entries in the center of the η distribution. This means that the charge sharing is strongly increased and therefore a part of the seed strips collects less signal while a neighbor collects more ($\eta \approx 0.5$) compared to a lower voltage.
This can be explained by a change of the surface conditions during the measurement by the used ^{90}Sr source and annealing out afterwards. A detailed discussion of this effect can be found in chapter 8.1.

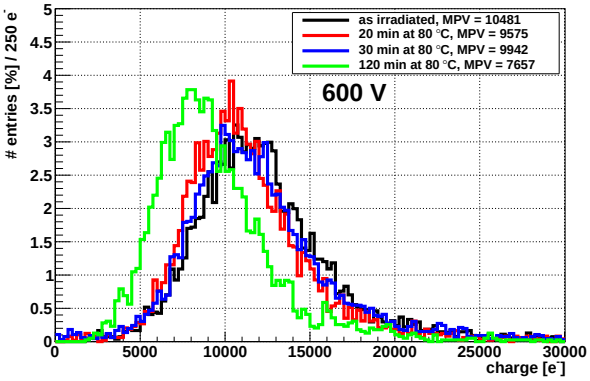

(a) Four strip cluster charge distribution at 600 V

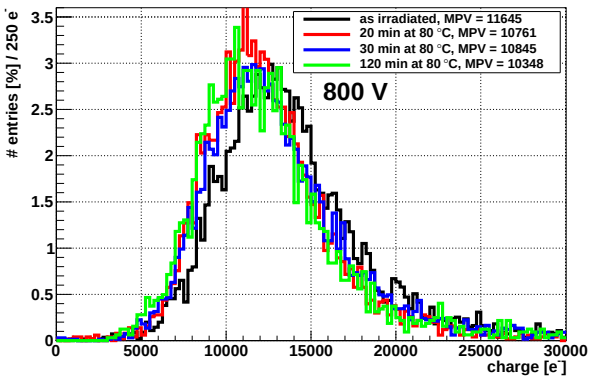

(d) Four strip cluster charge distribution at 800 V

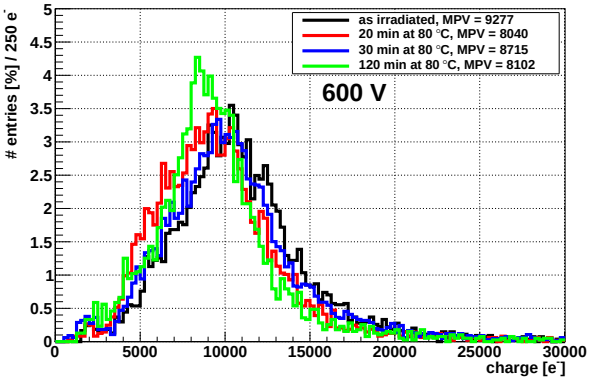

(b) Seed cluster charge distribution at 600 V

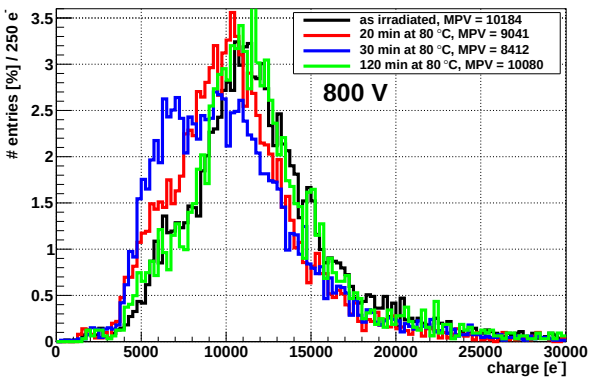

(e) Seed cluster charge distribution at 800 V

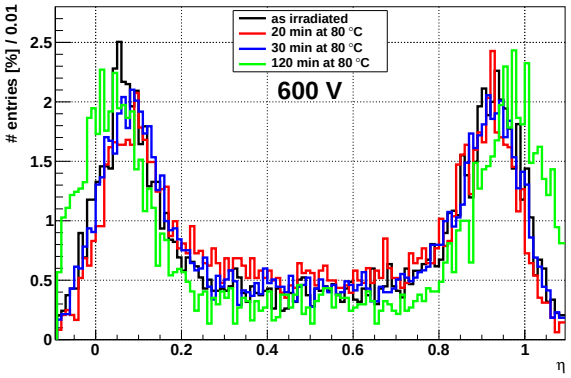

(c) η-distribution at 600 V

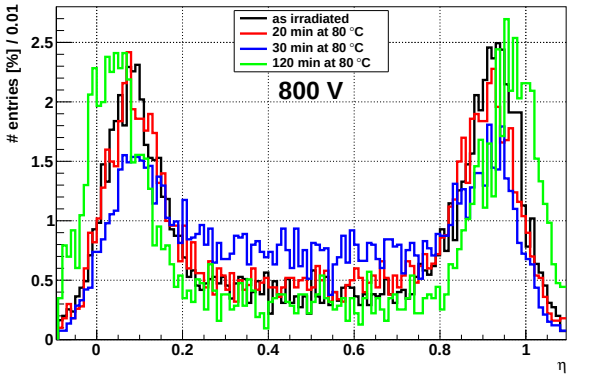

(f) η-distribution at 800 V

Figure 7.13: Charge distributions of clusters found with the "no cut" algorithm with clusters consisting of four strips (top row) and seed only (middle row) and η-distributions (bottom row) of an irradiated FZ200P sensor at different annealing times at 600 V (figures (a) to (c)) and 800 V (figures (d) to (f)).

Influence of the sensor surface on charge collection and noise

8.1 Signal loss of p-bulk strip sensors with time

It was found that the signal height changes with time inside the measurement setup. In this chapter a phenomenological, as well as a qualitative description using simulations will be given.

8.1.1 Experimental conditions

The charge collection of a non-irradiated MCz200P strip sensor (see figure 8.2) was measured repeatedly over several days under constant environmental conditions:

- 600 V bias voltage
- low humidity ($< 1\%$)
- fixed ^{90}Sr source position

Surface layout of the investigated sensor

The geometry of the segmentation of the silicon sensors has a big influence on the performance of the sensors. This segmentation has to be optimized in several aspects:

- position resolution,
- interstrip and coupling capacitance (influencing charge sharing and noise),
- breakdown voltage (to make a high operation voltage possible),
- isolation of the channels.

The pitch and implant width are two important parameters influencing the interstrip capacitance, the position resolution and the breakdown voltage.
Depending on the type of readout, these parameters have to be optimized in different ways. For the binary readout of the future CMS tracker, a low charge sharing as well as a small pitch are beneficial.
A high breakdown voltage is always beneficial, so is a good isolation of the channels.
The layout of the surface of the used sensors was already shown in section 5.1.3. However, for the understanding of the surface induced charge loss discussed in this section, a more detailed

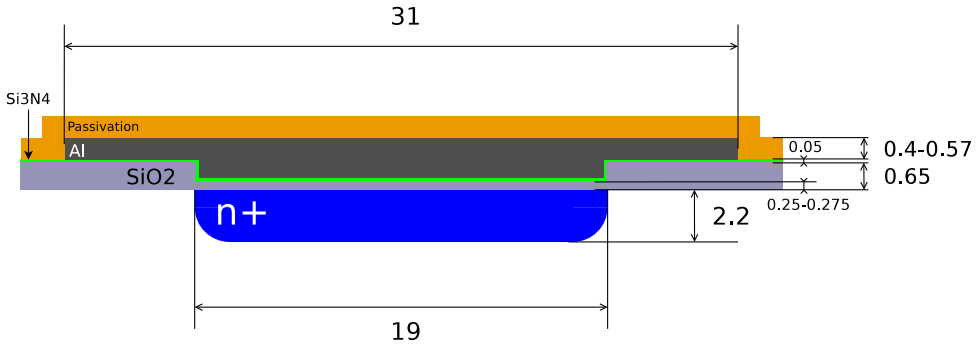

Figure 8.1: Layout of a single strip. Dimensions given in µm.

drawing of the strip and the strip isolation is shown in figures 8.1 and 8.2.

Figure 8.1 shows only the region of a strip in a p-bulk sensor. The n^+-implant that collects the charge is connected via a resistor to ground. The signal is ac-coupled to the readout aluminum strip. A high coupling capacitance is beneficial, so a thin isolation layer consisting of SiO_2 and Si_3N_4 is used in the area of the implant.
Outside the implant the thickness of the isolation layer is increased to obtain a higher breakdown voltage. Also, the metal overhang of the aluminum readout strip is used to reduce high field spots and to increase the breakdown voltage.
Another isolation layer covers the surface of the whole sensor (except contact holes) to increase the mechanical robustness of the sensor.

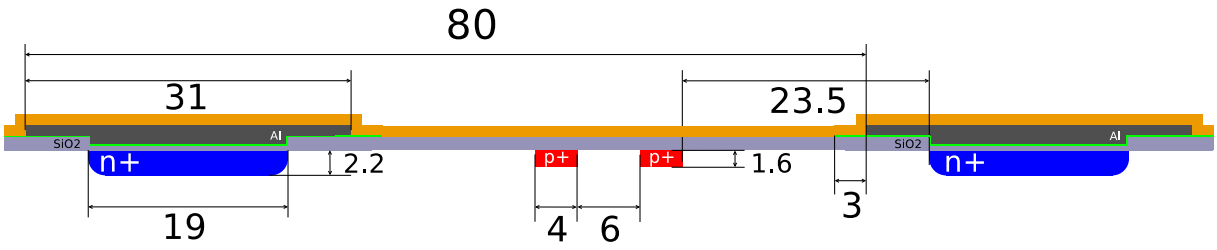

Figure 8.2: Layout of two strips isolated with p-stop. Dimensions given in µm.

The isolation of two strips with the p-stop technique is shown in figure 8.2. A well of medium-high p^+ doped silicon surrounds the strip implant, so that two p-stop wells are placed between two strips.
The isolation of the strips is needed in p-bulk sensors since the Si-SiO_2 interface is positively charged due to imperfections in the lattice there. This positive charge attracts electrons which cannot enter the interface and therefore accumulate beneath the interface. This electron accumulation layer is a conductor that connects the n^+ implants. Obviously, this connection is not wanted, so the accumulation layer is interrupted by the p-stop (see figure 8.3).

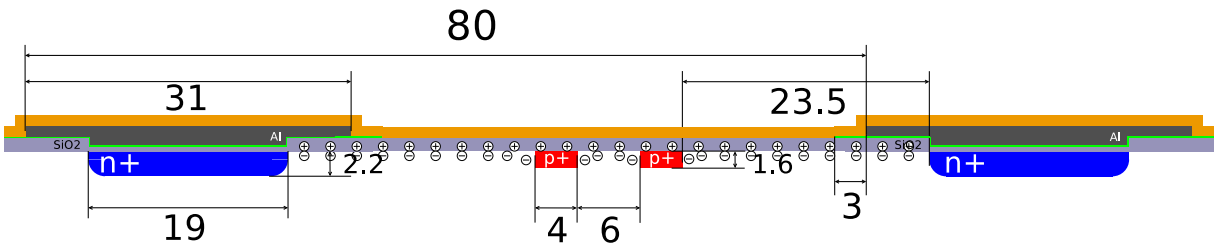

Figure 8.3: Sketch of two strips with p-stop and oxide charge. Dimensions given in µm.

Ionizing and non-ionizing dose

The ^{90}Sr source has an activity of 100 MBq with a broad electron energy spectrum up to 2.2 MeV (see figure 4.13).

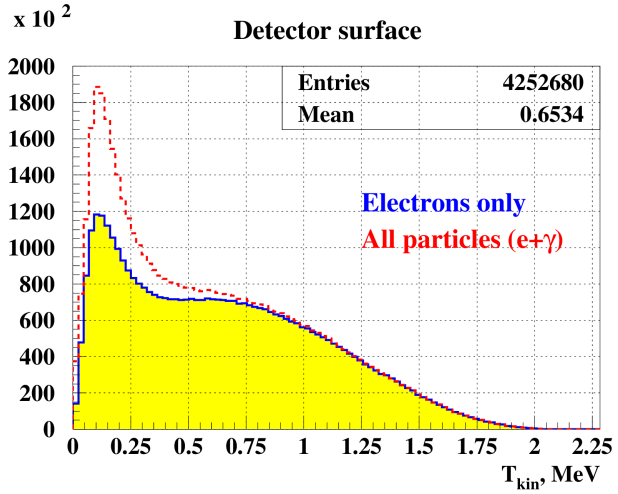

(a) Energy distribution of particles crossing the surface of the sensor

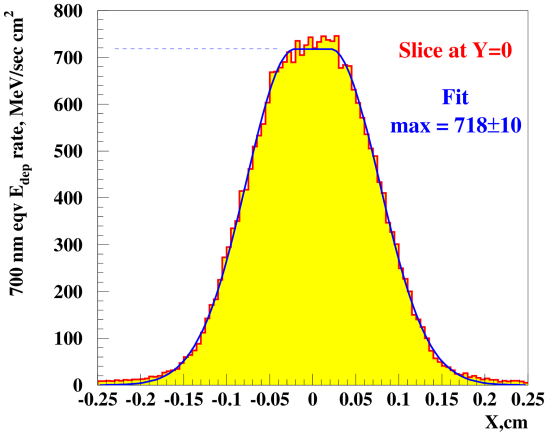

(b) Energy deposition of particles crossing the surface of the sensor

Figure 8.4: Simulated energy distribution (a) and deposition (b) of the electrons and photons passing through the silicon dioxide on the sensor surface. The simulation was performed by Sergej Schuwalow using GEANT 3 [40].

Most electrons are absorbed by the collimator and only a fraction reaches the surface of the sensor. The resulting energy spectrum at the sensor's surface is shown in figure 8.4a. Only the high energetic tail is selected for the measurement by a trigger system, but the low energetic particles also deposit energy in the sensor. The energy deposition in the thin silicon oxide layer on the surface of the sensor is shown in figure 8.4b. The simulations were performed by Sergej Schuwalow using GEANT 3.
Since the particles are collimated using a 0.7 mm hole, the energy is deposited in a spot with a FWHM of about 1.8 mm and a flat maximum with a diameter of 0.7 mm. In the maximum spot the surface is irradiated with $\approx$ 2.25 Gy per hour. The integrated dose of the sensor during the measurements described in the following is shown in figure 8.5.

In addition to the surface damage, that was discussed above, the used ^{90}Sr source is able to

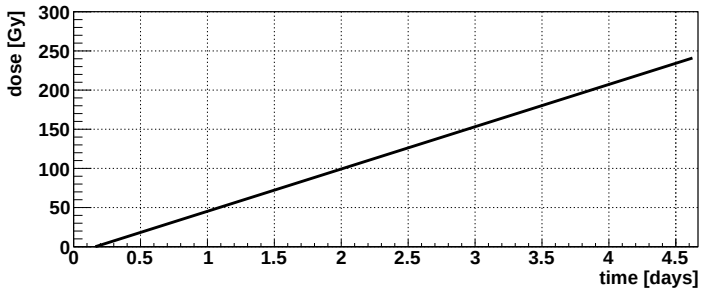

Figure 8.5: Cumulated dose of the ^{90}Sr source based on the simulation shown in figure 8.4.

produce bulk damage. The energy needed to produce damage in the silicon lattice is about 300 keV. However, the damage produced is strongly dependent on the particle energy, so that only the high energetic tail produces defects in a relevant amount. This also leads to a uniformly distributed damage of the hole depth of 200 µm of the sensor. The lateral bulk damage distribution is shown in figure 8.6.
In the central region the fluence was simulated to be $\approx 4.7 \cdot 10^8\,\mathrm{neq\,cm^{-2}\,h^{-1}}$.
This means, that after 5 days of irradiation, a bulk damage comparable to $\approx 5.6 \cdot 10^{10}\,\mathrm{cm^{-2}}$ 1 MeV neutrons is produced. This fluence is one order of magnitude below fluences, where changes of the macrospopic behavior are observed. This leads to the assumption, that the bulk damage can be neglected in this case.

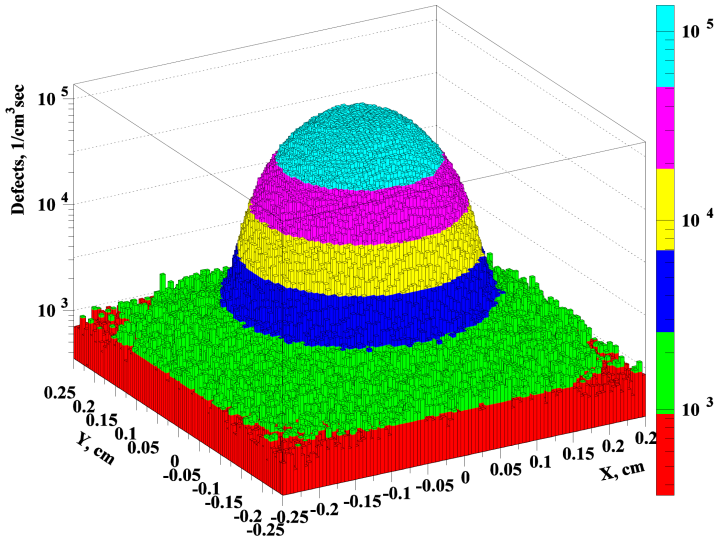

Figure 8.6: Bulk damage caused by the used ^{90}Sr source. The simulation was performed using GEANT 3 by Sergej Schuwalow [40].

8.1.2 Development of the sensor characteristics with time

In this section the development of the charge loss in the first days of measurement will be discussed.
In contrast to the chapters before, in this section not the most probable value (MPV) of the Landau distribution convoluted with a Gaussian is shown, but the median of the distribution. The reason is that the seed distribution is only well described by the Landau-Gauss convolution if enough charge is collected by the seed.
Since the effect discussed in this section reduces the seed signal and increases the charge sharing, the description is not sufficient anymore. The usual choice would be the mean in such a situation, however, the highly skewed Landau distribution leads to a very unstable mean. The median is much more stable, since a few events with a high signal have only a small influence on the median value.
The median value is typically higher than the MPV (in the order of 10 % in this case), yet the absolute scale is not important for the change in sensor performance.

Cluster charge

Figure 8.7 shows the signal loss of a non-irradiated MCz200P sensor with time.

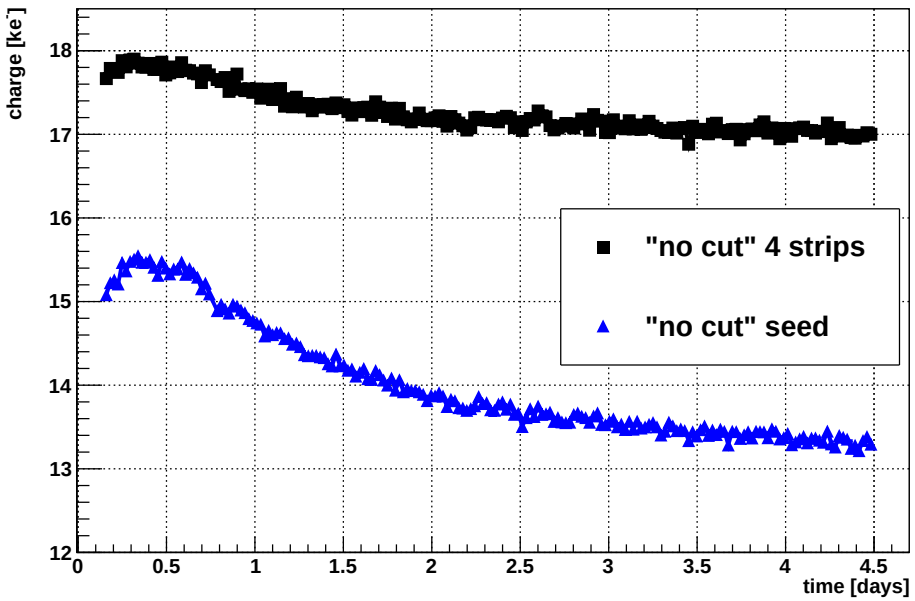

Figure 8.7: Change of collected charge with time for a non-irradiated MCz200P strip sensor at a bias voltage of 600 V.

The ^{90}Sr source constantly irradiated the sensor. Runs with a length of $\approx$ 10 minutes are alternating with breaks of $\approx$ 20 minutes. During the breaks the bias voltage and irradiation by

the ^{90}Sr source stay constant.
The signal height increases for the first five hours. After that, the signal height starts an exponential decrease that nearly saturates after 4.5 days.
The effect is different for the "full" 4 strip wide cluster and the seed signal alone. While the loss is in the order of 5 % for the full cluster, the seed cluster's loss is found in the order of 15 %.
The difference can be explained by a difference in the charge sharing between the strips.

Charge sharing

A measure of the charge sharing is the η-distribution, which was discussed in section 7.2.3.
The position distribution of the particles does not change with time, so the ratio of particles crossing the sensor near the readout strips to particles crossing in between readout strips stays constant.
Using this knowledge, the fraction of events with a value of η in the range of $0.2 < \eta < 0.8$ (in between the strips) is used to show the change in charge sharing:

$$\frac{N_{0.2<\eta<0.8}}{0.6 \cdot N}$$

The scaling is chosen in such way, that at 0 % no charge is shared between strips and at 100 % the η-distribution is uniform, indicating a very strong charge sharing.

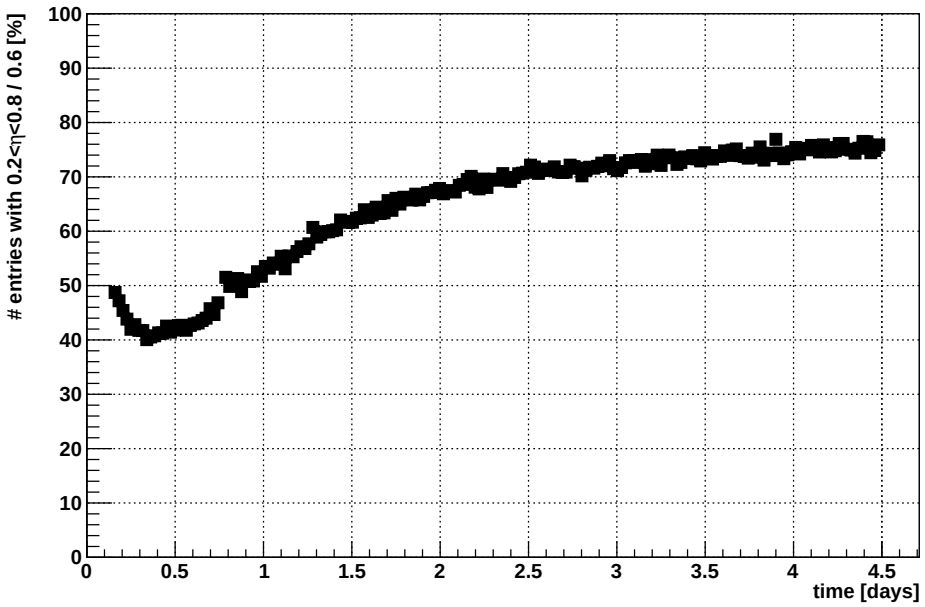

Figure 8.8: Change of charge sharing with time for a non-irradiated MCz200P strip sensor at a bias voltage of 600 V.

The change of the charge sharing, as shown in figure 8.8, reflects the charge loss of the seed

shown in figure 8.7. It decreases in the first 5 hours and starts to increase afterwards.
The increase of charge sharing leads to a signal loss in the seed channel and an increasing charge collected by the neighboring strips and therefore lost for the seed signal.

Noise

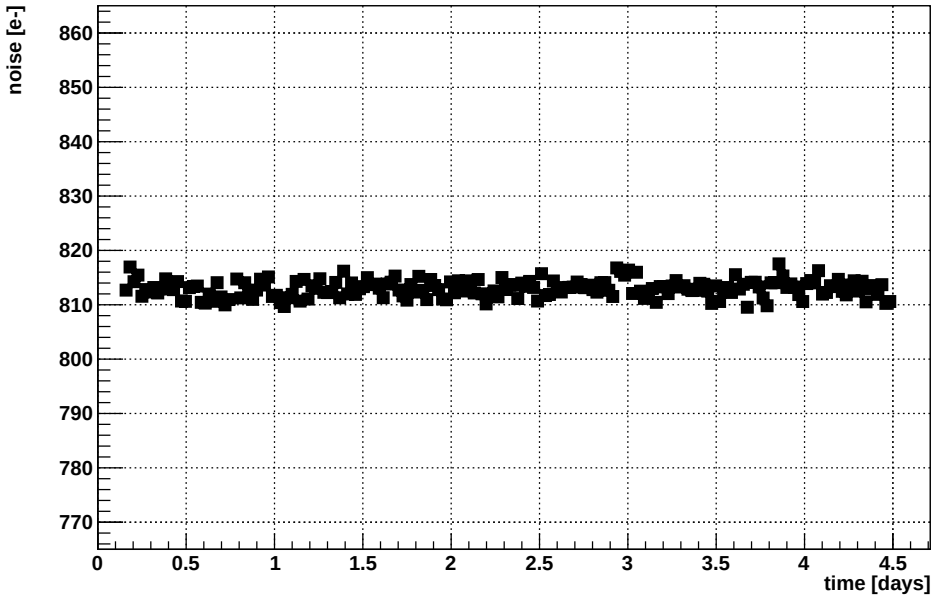

(a) Noise development with time.

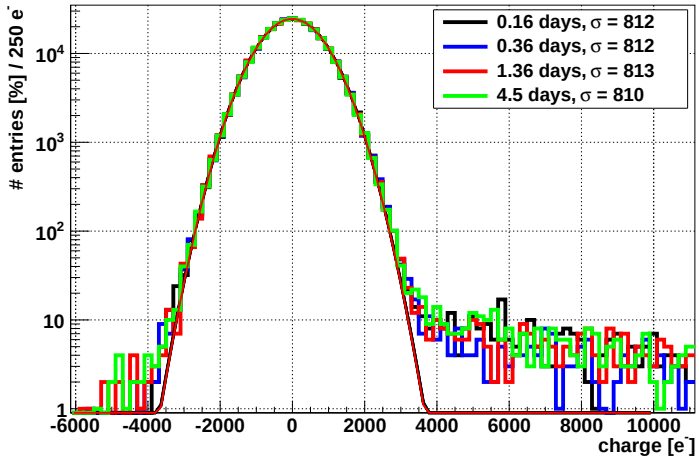

(b) Noise at specific points in time.

Figure 8.9: Noise development with time and at specific points in time for a non-irradiated MCz200P strip sensor at a bias voltage of 600 V.

The noise shown in figure 8.9a is defined here as the σ of a Gaussian fit to the distribution of all single channel signals after pedestal and common-mode correction of randomly triggered events (see figure 8.9b), while the ^{90}Sr source is placed above the sensor. The tail of this noise distribution is caused by particles creating signal in the randomly triggered measurements,

since the probability of signals created by particles is small but not zero.
The noise is very stable over time, indicating that the measurement system calibration does not change. This fact proves that the found decrease of signal is not caused by an instability of the measurement system.

8.1.3 Sensor characteristics at specific times

Voltage dependence of the charge collection at relevant times

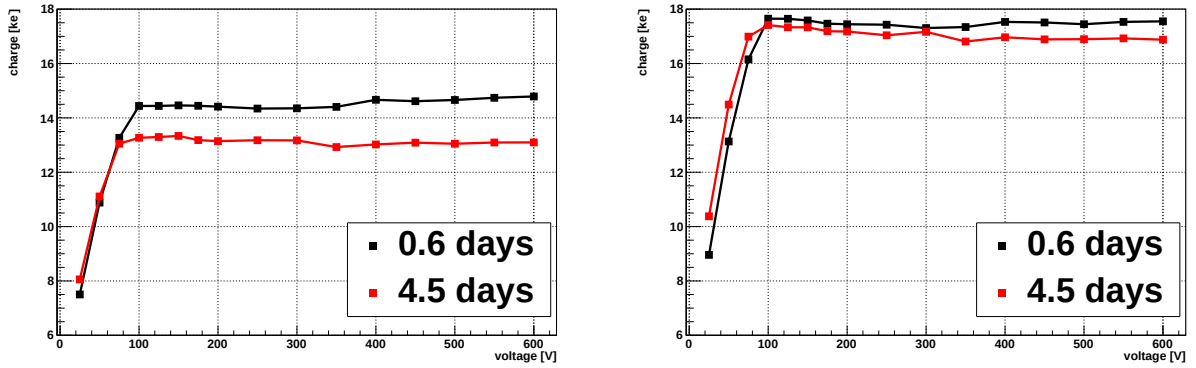

(a) Seed charge

(b) Four strip cluster charge

Figure 8.10: The signal with voltage for two different times (at the maximum and after saturation of the collected charge). Figure (a) shows the collected charge determined using the seed of the "no-cut" algorithm, while figure (b) shows the collected charge using the four strip cluster of the "no-cut" algorithm.

Figure 8.10 shows the measurement of the charge collection versus voltage for two specific points in time, one near the maximum (after 0.6 days) and one at the end of the measurement shown in figure 8.7 (after 4.5 days). Two time dependent effects are visible:

1. A change of the full depletion voltage,

2. A change of signal height.

While the change in collected charge is very significant, the change of the full depletion voltage is less clear.
The change in full depletion voltage could be explained by a change of fixed charges in-between the strips leading to a change in the distribution of the electric field and thus allowing a smaller bias voltage to deplete the whole volume.
The change in signal height was already shown for 600 V in figure 8.7. However, figure 8.10 shows this change over the full voltage range above full depletion.

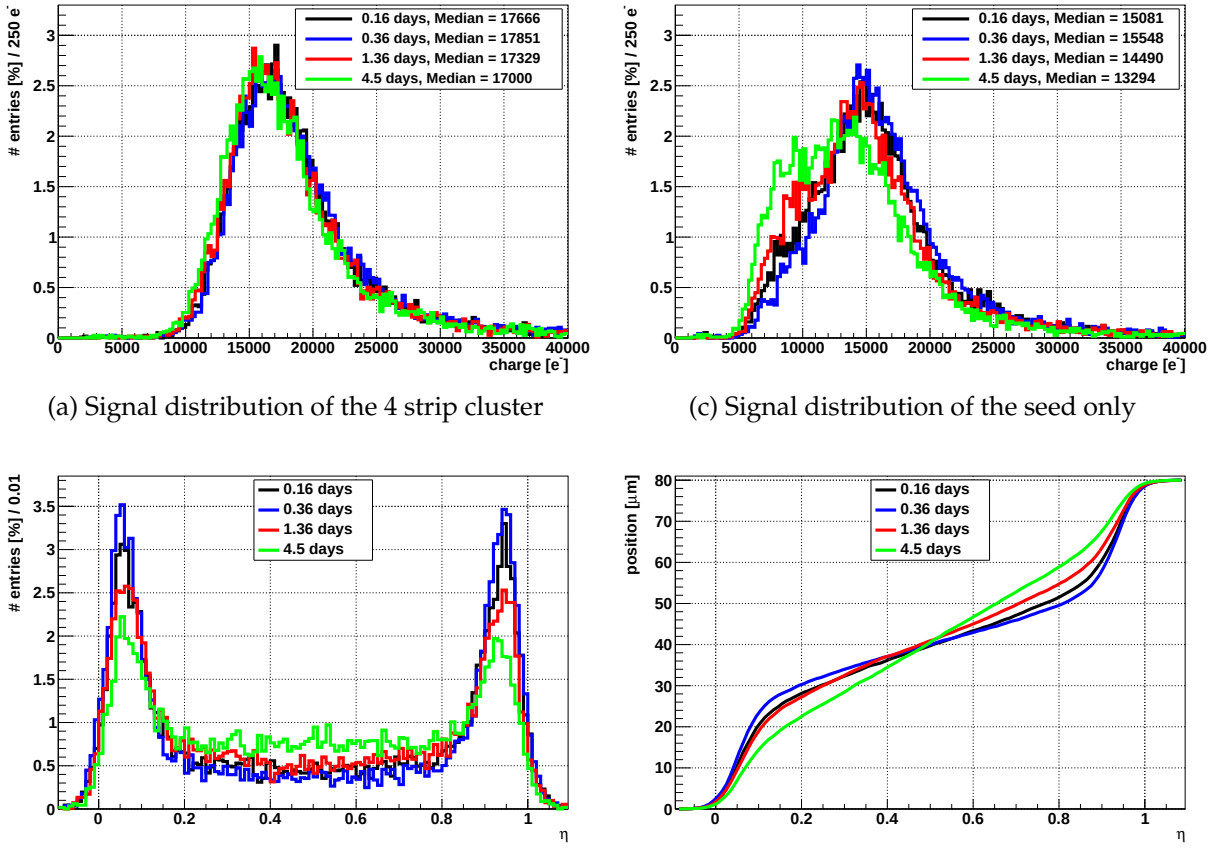

(a) Signal distribution of the 4 strip cluster

(c) Signal distribution of the seed only

(b) η-distribution

(d) $\int$ η-distribution

Figure 8.11: Charge collection and η-distributions of a MCz200P strip sensor.

Distributions of the collected charge and η at specific times

Figure 8.11 shows key distributions for four important times in the charge loss development shown in figure 8.7. The upper row (figures 8.11a and 8.11c) show the charge distributions of the cluster and the seed signal. While the charge distributions of the four strip clusters (a) show only a shift of the median, the shape of the charge distributions of the seed (c) changes in addition to a shift.
The distribution after 0.36 days (8 h and 38 min) shows a similar shape to the four strip cluster charge distributions, which is, however, slightly broader. The distribution at the other points in time shows a broadening towards lower values, while the higher edge only changes slightly. This is caused by the increase of charge sharing, which leads to an increased number of events with a relevant fraction of charge induced in a neighboring strip.
The η-distribution (b) and the integral of it (d) also show this increase in charge sharing. The region of $0.2 < \eta < 0.8$ shows an increasing part of entries for a decreasing seed signal.
The integral of the η-distribution can be used to correlate the η value and the position where

the particle passes through the sensor. To do so, the assumption is made that the number of particles crossing the sensor is equally distributed over the whole area. This is not fully correct in this case, but since the spot of the source is about 2 mm wide and the pitch is 80 µm, it is a good assumption.

Charge sharing at specific times

The signal of the seed and neighboring strips is shown for different position of passing particles in figure 8.13. The position is obtained using the integrated η-distribution shown in figure 8.11d. The strips are labeled according to figure 8.12. The particle passes in-between strips L and R.

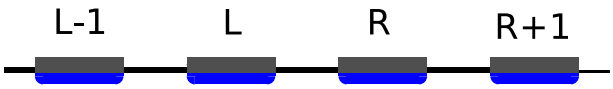

Figure 8.12: Schematic of the nomenclature for used strips.

The positions in figure 8.13 are binned with a bin width of 16 µm to have enough statistics. This means, that the centers of the outer bins (around 8 µm and 72 µm) reach from the strip centers (at 0 µm or 80 µm) 16 µm towards the other strip, while only the first (last) 8.5 µm are at the strip implant. Figure 8.13a shows the case of maximal seed signal and minimal charge sharing (after 0.36 days). Most signal is induced to one strip, only when particles are crossing in the very middle between the readout strips the charge is shared between them. The outer strips only contribute, when they are near the seed strip and the particle passes in the middle between strips.
Figure 8.13b shows the case of a decreased seed signal and increased charge sharing (after 4.5 days). The signal is shared between several strips, whenever the particle crosses not directly through the readout strip.
Strips further away from the position where the particle crossed the sensor do not contribute to the signal significantly, as shown in figure 8.14. While the fifth strip adds $\approx 100\,e^-$ to the cluster signal, the cluster signal is stable when more strips are added. This indicates that the signal induced in the far outer strips is too small to compensate the charge loss in the central strips.
This means that not only the charge sharing is increased with time, but also the total signal is reduced.

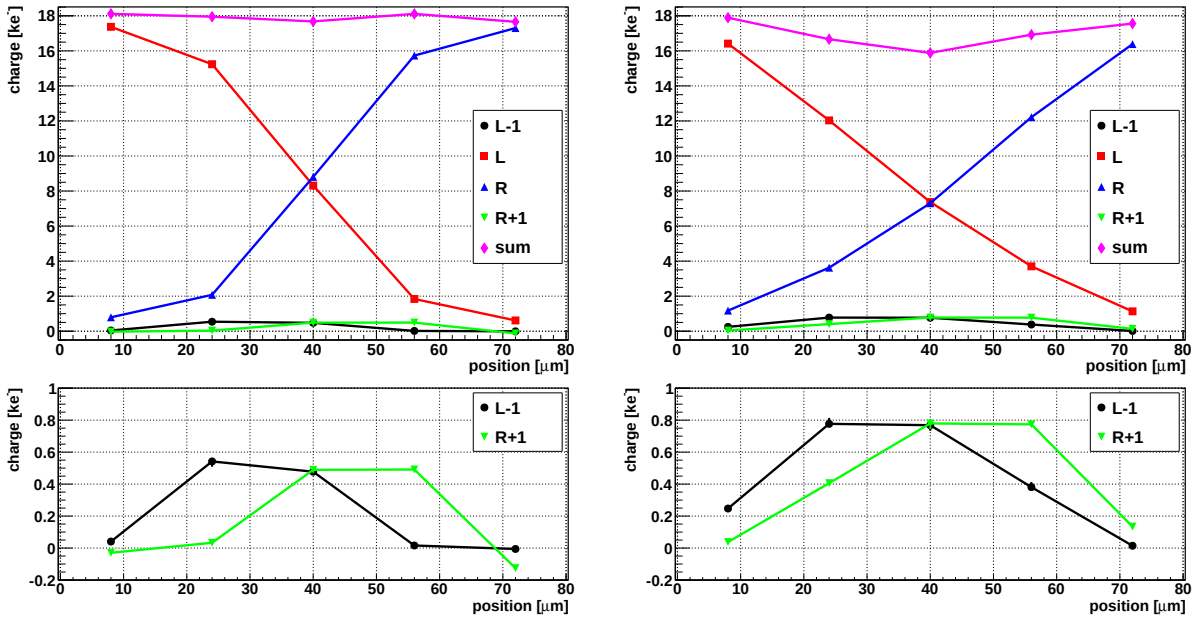

(a) 0.36 days

(b) 4.5 days

Figure 8.13: Collected charge at different positions.

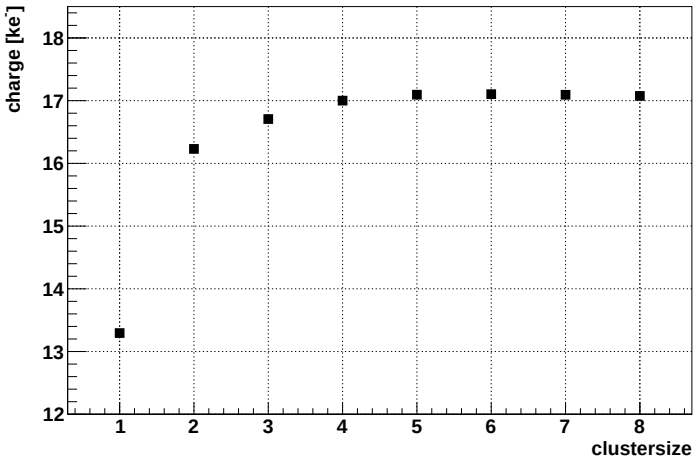

Figure 8.14: Dependence of the total signal on the cluster size for a non-irradiated MCz200P strip sensor after 4.5 days at a bias voltage of 600 V.

8.1.4 Possible explanation

Using the concept of weighting potentials (see figure 7.7) and the data shown in figure 8.13, the change in charge sharing can be explained by a change of the electrical field in the region

between the strips.
If the field is shaped in such a way that the field lines end at the readout strip (the situation after 0.36 days), the signal couples strongly to the strip where the charge carriers arrive, and either not at all or only weakly to neighboring strips.
If the field is shaped in such a way that at least some field lines end between the readout strips (the situation after 4.5 days), charges are slowed down at the surface between the strips so much, that they do not reach the readout strips within the integration time. This results in a stronger coupling to several surrounding strips and therefore in an increased charge sharing as well as a loss in absolute signal height.
The electrical field is influenced not only by the geometry of the readout strips, but also by surface charge in-between the strips. An irradiation with the ^{90}Sr source leads to a change of the surface charges and thus change the electrical field configuration.

8.1.5 Simulation results of the electric field at the sensor surface

In figure 8.15 the electrical potential and field distribution for a low and high surface charge concentration is shown. The simulations of the electrical field and potential were performed by Jörn Schwandt [62].
The electrical field shows a strong bending towards the readout strips in the situation with low oxide charge (figures (8.15a) and (8.15b)) Charges drifting along the field lines induce a strong signal on the strip at which they arrive. This means the seed signal is high and the charge sharing is dominated by particles crossing at varying angles and diffusion.
In figures (8.15c) and (8.15d) the electrical field distribution for a sensor with a higher amount of surface charges is shown.
Many field lines do not point towards a readout strip anymore, but out of the sensor surface. Charges drifting along those field lines get stuck at the surface and cannot fully contribute to the signal within the integration time. Using the weighting potential together with the simulated electrical field, this means the coupling to the nearest readout strip is reduced and that to other strips is increased. This effect now dominates the charge sharing in the sensor.

8.1.6 Charge loss with a reduced dose rate

In figure 8.16 a comparison of the charge loss with the 100 MBq ^{90}Sr source shown in figure 8.7 and using a 37 MBq ^{90}Sr source is shown. The measurement with the 37 MBq ^{90}Sr source was performed at a new undamaged position on the sensor.
Since the dose rate is reduced, the comparison on the time axis is not showing a good agreement. However, if the x-axis is scaled to the estimated dose, the agreement is better, but still not perfect. It seems that the effect sets in with a delay of about 1 day (20 Gy) for the measurement with the reduced dose rate, compared to the one with the high dose rate. Moreover, the rise in the first hours after starting the measurement that was observed with the high dose rate, could not be observed here.
Even though the behavior is similar, there are some differences in the charge loss with time between the two used ^{90}Sr sources.

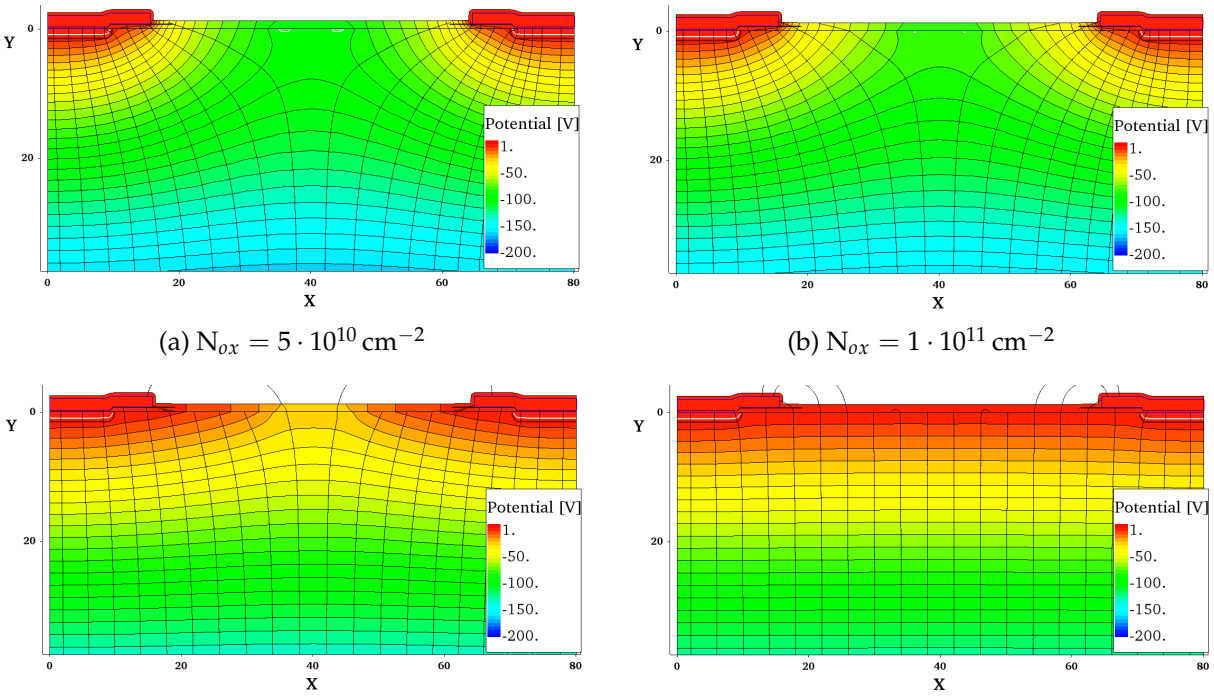

(a) $N_{ox} = 5 \cdot 10^{10}\,cm^{-2}$

(b) $N_{ox} = 1 \cdot 10^{11}\,cm^{-2}$

(c) $N_{ox} = 2.5 \cdot 10^{11}\,cm^{-2}$

(d) $N_{ox} = 5 \cdot 10^{11}\,cm^{-2}$

Figure 8.15: Electrical potential at 600 V with oxide charges of N_{ox}=0.5E11 cm^{-2} (a), N_{ox}=1E11 cm^{-2} (b), N_{ox}=2.5E11 cm^{-2} (c) and N_{ox}=5E11 cm^{-2} (d). Figures taken from [62].

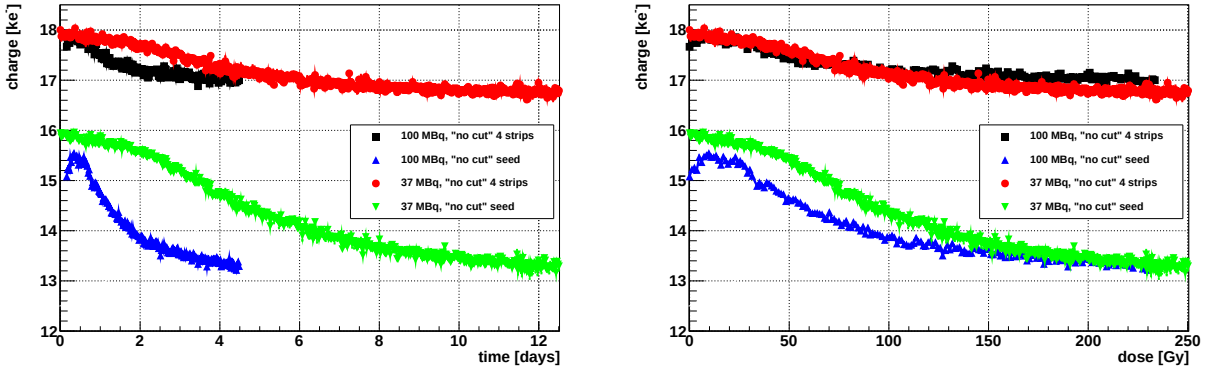

(a) Charge loss with time

(b) Charge loss with dose

Figure 8.16: Charge loss with time (a) and dose (b) using a weaker (37 MBq) ^{90}Sr source with the same geometry as the standard (100 MBq) ^{90}Sr source.

8.1.7 Position scan over damaged spot

To show that the observed charge loss is really caused by the irradiation with the ^{90}Sr source that was used for measurement, a position scan along the strips over the damaged spot was performed (see figure 8.17). It can clearly be seen that the seed as well as the cluster signal drop in the region of 58 mm to 64 mm. The used position for most measurements was 61 mm. This indicates, that the charge loss really is caused by the ^{90}Sr source.

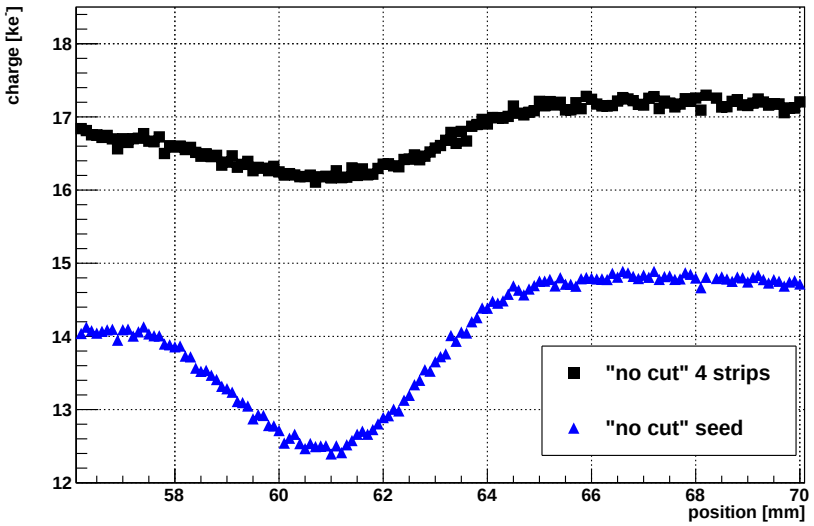

Figure 8.17: Position scan over the damaged spot along the strips with the 100 MBq ^{90}Sr source.

8.1.8 Annealing of surface charge

It was tried to recover the initial state of the surface charges after the initial charge loss, shown in figure 8.18. This was done by an increase of the sensor temperature for 18 hours and a 6 hour measurement at -20 °C afterwards. The bias voltage was kept constant at 600 V, except during the annealing at 80 °C. The ^{90}Sr source was removed during annealing.
While annealing with temperatures $\leq$ 40 °C did not change the situation visibly, the annealing at 60 °C shows a visible recovery, which is even more pronounced after the annealing at 80 °C. However, the sensor is not recovered immediately but recovers during a period of 6 hours of measurement. After the initial recovery the charge sharing starts to increase again, with a similar time constant as in the beginning. The recovery during the measurement after annealing is not yet understood.

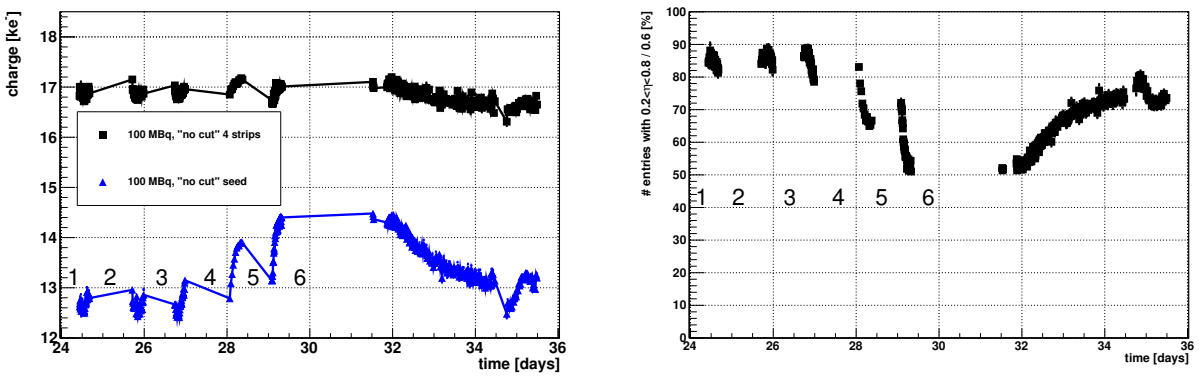

(a) (b)

Figure 8.18: Charge collection (a) and charge sharing (b) after annealing. Between the shown measurements, the sensor was annealed. A description can be found in 8.1.

	end time [days]	duration [hours]	temperature [°C]	bias voltage [V]
1	24.5	120	-20	600
2	25.5	18	20	600
3	26.5	18	40	600
4	28	18	60	600
5	29	18	80	$\approx$ 350
6	32	60	-20	600

Table 8.1: Annealing history of non-irradiated MCz200P strip sensor.

8.1.9 Charge loss on a FZ200Y sensor

The charge loss discussed above was studied on a MCz200P sensor, meaning the strips are isolated using the p-stop technique. A similar behavior was found measuring a sensor with p-spray isolation. The charge loss of a FZ200Y sensor is shown in figure 8.19.
Unfortunately, the first day of measurement was not taken, since the measurement got stuck at 125 V bias voltage. However, this sensor shows qualitatively a similar behavior. The signal measured on the seed decreases strongly over time, while the four strip cluster signal decreases only slightly. This is reflected in the increase of the charge sharing.

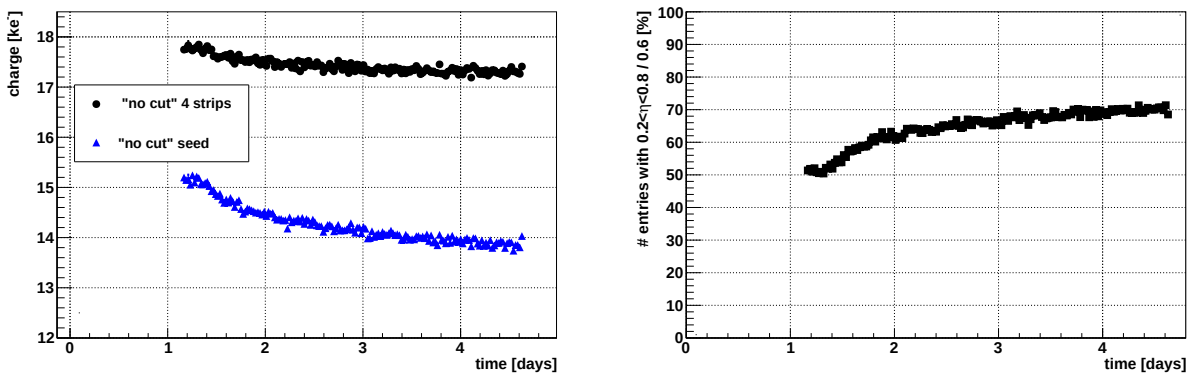

(a) Charge collection (b) Charge sharing

Figure 8.19: Charge loss of a FZ200Y sensor with p-spray isolation.

8.1.10 Charge loss of an irradiated sensor

Sensors that were irradiated at the PS with 23 GeV protons also show an increase in charge sharing with time, however, not as strong as the non-irradiated sensors. During the proton irradiation the surface irradiaton dose was in the order of $\mathcal{O}(10^5\,\mathrm{Gy})$, so if the dose is the only relevant contribution the sensors should be in a state of very high charge sharing. An example of a FZ200P sensor irradiated to a fluence $\Phi_{neq} = 1.5 \cdot 10^{15}\,\mathrm{cm}^{-2}$ with protons and in addition $\Phi_{neq} = 6 \cdot 10^{14}\,\mathrm{cm}^{-2}$ neutrons is shown in figure 8.20.
Before the shown measurements start, several measurements and also annealing were performed. The shown timeline starts from the last annealing.

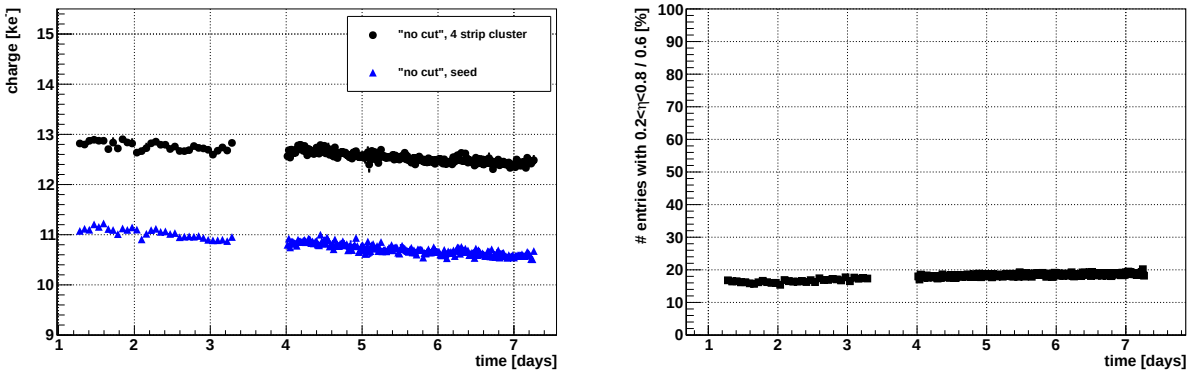

(a) Collected charge (b) Charge sharing

Figure 8.20: Charge loss of a sensor irradiated with protons and neutrons (15 p_G + 6 n). Measured at a bias voltage of 1000 V.

Even after this very high dose, the charge sharing is very low. The qualitative picture with time is similar to the measurements of the non-irradiated sensors. The total signal is reduced, while

the charge sharing is increased.
The voltage scans shown in figure 8.21, however, show a decrease of the collected charge as well as a slight decrease in charge sharing for the two measurements after the second irradiation but before any annealing (labelled 50 Gy and 340 Gy). The measurement in between the timeline shown in figure 8.20 is labelled 3.5 days. It shows a strong increase of the collected charge at low voltages compared to the first two measurements, while it is compatible at higher voltages. The charge sharing at higher voltages is slightly increase.
The fact that a long time inside the setup reduces the charge collection further, indicates that the irradiation with the ^{90}Sr source inside the setup still changes the surface charges. Since the additional dose of the ^{90}Sr source is very low compared to that of the proton irradiation this was not expected.
Possible explanations for this observation could be that:

- The local concentration of irradiation inside the measurement setup causes a different behavior than a uniform irradiation.
- The additional high bulk damage during the proton irradiation influences the electrical field in such ways, that the charge sharing is reduced.
- The influence of the low energetic electrons is different to that of high energetic protons.

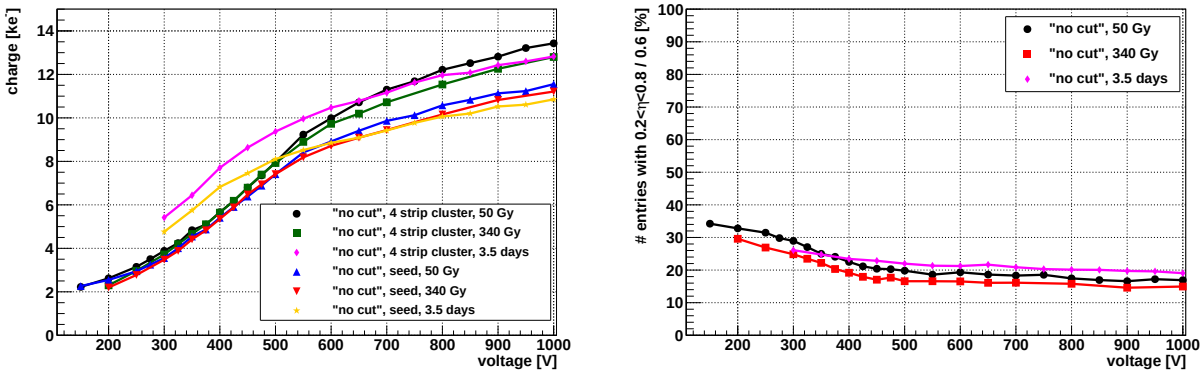

(a) Collected charge

(b) Charge sharing

Figure 8.21: Charge of a sensor irradiated with protons and neutrons (15 p_G + 6 n) versus voltage. The measurements labelled 50 Gy and 340 Gy were performed after the irradiation and the given dose is the cumulated dose in the setup after both irradiations. The measurement labelled $\approx$ 3.5 days was performed after more measurements and annealing. The time is counted from the last annealing and corresponds to the time given in figure 8.20.

8.1.11 Relevance for the CMS tracker

While the effect of charge loss discussed above occurs already at doses in the order of $\mathcal{O}(100\,\mathrm{Gy})$, the expected dose in the CMS tracker is according to [63] in the order of $\mathcal{O}(10^5\,\mathrm{Gy})$ after an integrated luminosity of L$= 3000\,\mathrm{fb}^{-1}$, which corresponds to the HL-LHC runtime. This would indicate that the sensors will show this increased charge sharing already after a few days of operation.
As discussed in section 7.2.1, the cluster finding efficiency in the case of a binary readout is strongly dependent on the seed signal and not so much on the cluster signal. The cluster finding efficiency for a bulk damaged sensor at the end of the HL-LHC runtime positioned at the inner radius of the strip-tracker is at $\approx$ 90 % with a threshold of $6000\,\mathrm{e}^-$ and a bias voltage of 600 V, not taking into account the Lorentz angle and higher angles of crossing particles (see figure 7.12). A decrease of the seed signal of $\approx$ 15 % and the corresponding change of the shape of the distribution would result in an cluster finding efficiency in the order of $\approx$ 80 % with the same threshold and bias voltage.

However, the proton irradiation of sensors at the PS to a fluence of $\Phi_{neq} = 1.5 \cdot 10^{15}\,\mathrm{cm}^{-2}$ corresponds to an irradiation dose of the sensor surface in the order of $\mathcal{O}(10^5\,\mathrm{Gy})$. As shown in figure 8.20 and 8.21, the charge sharing is not as high as it could be expected from the dose.
However, more studies will need to be performed to understand the exact conditions causing the change in charge sharing.

8.2 Non-Gaussian noise on n-bulk strip sensors

The sensors irradiated with neutrons show only a slightly increased noise, while the proton irradiated samples show a stronger increase of the noise, especially the sensors irradiated with 23 GeV protons. The sensors discussed in this chapter are baby additional (Badd) sensors with 64 strips, a pitch of 80 µm, an implant width of 19 µm and a metal width of 31 µm, similar to that shown in figures 8.1 and 8.2 with p^+ readout implant, n-bulk and no p-stop wells.

8.2.1 N-bulk strip sensors irradiated with 23 GeV protons and neutrons

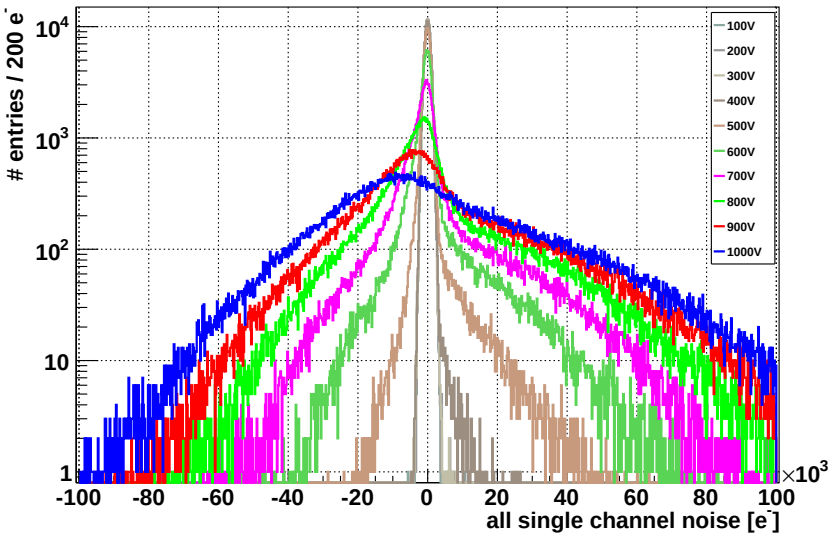

Figure 8.22: Noise histograms at different bias voltages after irradiation to a fluence of $(15+6)\cdot 10^{14}\,cm^{-2}$. The noise of this sensor at a bias voltage $\leq$ 300 V is similar to the best noise distribution that can be achieved with this setup. At high bias voltages, however, the noise is very much increased and shows strong non-Gaussian tails. Moreover the maximum of the Gaussian part is shifted to negative values, which could be caused by a bias of the common mode noise correction.

An example of the additional (non-Gaussian) noise is shown in figure 8.22. At a low bias voltage $\leq$ 300 V the noise distribution is Gaussian and narrow, with a RMS of about 1000 e^-. At higher bias voltages the non-Gaussian noise is clearly visible. The maximum of the distribution is shifted to lower values due to a failure of the common mode correction at this high noise level.

Time dependence

The noise is reduced with time when bias voltage is applied (1000 V in the case shown in figure 8.23). The shown noise value is the RMS of distributions like the one shown in figure 8.22. The

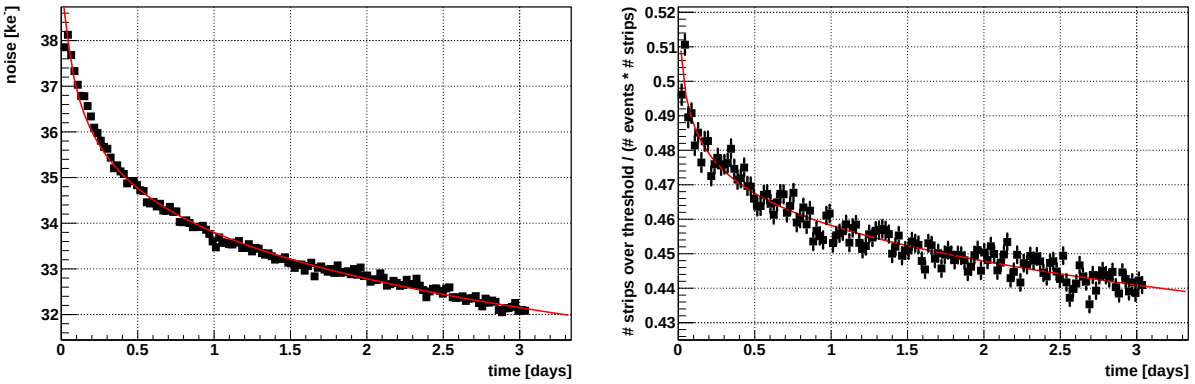

(a) Noise versus time

(b) Noise occupancy versus time

Figure 8.23: Noise versus time (a) and noise occupancy versus time (b) for MCz200N material strip sensors after 23 GeV proton and neutron irradiation to a fluence of $(15 + 6) \cdot 10^{14}\, cm^{-2}$. The measurements were performed at a fixed bias voltage of 1000 V.

noise occupancy shown in figure 8.23b is defined as the number of strips above a threshold of 6000 e^- divided by the number of events and active strips. The resulting noise occupancy gives an estimation of false hits. This value gives a measure how often a discharge is taken as a signal. In this case multiple counts per event are allowed. A value of 1 would mean all strips give always a fake hit, and 0 means that no fake hits occur at all.
The noise reduction is very slow and can be described using a logarithm.

$$-1.4 \cdot log(10^{-8} \cdot x) + 7.9$$

Training procedure

It was found within this work that the noise can be reduced faster using a training procedure:

1. Set the temperature of the sensor to 1 °C.
2. Increase the humidity to a dew point of ≈ 5 °C.
3. Set the bias voltage to the highest possible value (typically in the range of 600 to 750 V).
4. Wait ≈ 5 minutes.
5. Reduce the humidity and wait until the sensor is completely dry.
6. Switch off the bias voltage.

The noise versus bias voltage is shown in figure 8.24a before and after the "training" procedure. The plotted value is the RMS taken from a histogram like those shown in figure 8.22.

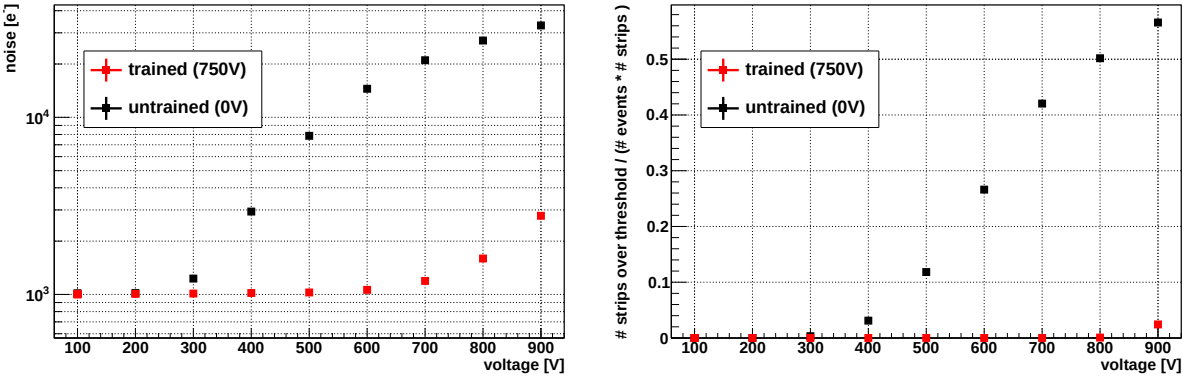

(a) Noise versus bias voltage

(b) Noise occupancy versus bias voltage

Figure 8.24: Noise versus bias voltage (a) and noise occupancy versus bias voltage (b) for FZ200N material strip sensors after 23 GeV proton and neutron irradiation to a fluence of $(15+6)\cdot 10^{14}\,cm^{-2}$. The black points show the "untrained" sensor (training procedure performed at 0 V), while the red points show the sensor "trained" at 750 V.

Possible explanation

This high noise could be explained by micro-discharges near the strips. Simulations of other institutes in the campaign show that the electrical field of n-bulk sensors after ionizing irradiation has very high peaks near the strips due to charges in the Si-SiO_2 interface (see also [60]). The surface charges need a counter-charge on the surface to reduce the peaks of the electrical field within the sensor. These surface charges have to be mobile, in order to balance the interface charges. This can be achieved by applying a high bias voltage for a long time or by applying the bias voltage in a humid atmosphere for a shorter time, since the mobility of surface charges depends very strongly on the humidity on the surface, as discussed in [34].
The noise occupancy shown in figure 8.24b is defined as the number of strips above a threshold of 6000 e^- divided by the number of events and active strips. The resulting noise occupancy gives an estimation of false hits.
The figures 8.24 show the very high noise level of the untrained sensor from 400 V upwards. After the training procedure described above, the noise is reduced to a normal level up to 700 V due to the applied voltage for the training of 750 V.

8.2.2 Non-irradiated n-bulk strip sensors

In non-irradiated strip sensors the noise could be created by irradiating with the ^{90}Sr source. Figure 8.25 shows the noise and noise occupancy versus time under bias (600 V) and underneath the source. It is clearly visible that the noise increases after some days of measurement time.

The measurements were performed several times in a dry atmosphere with increasing and decreasing bias voltage to obtain a hysteresis. The first measurement ends at 600 V at a noise

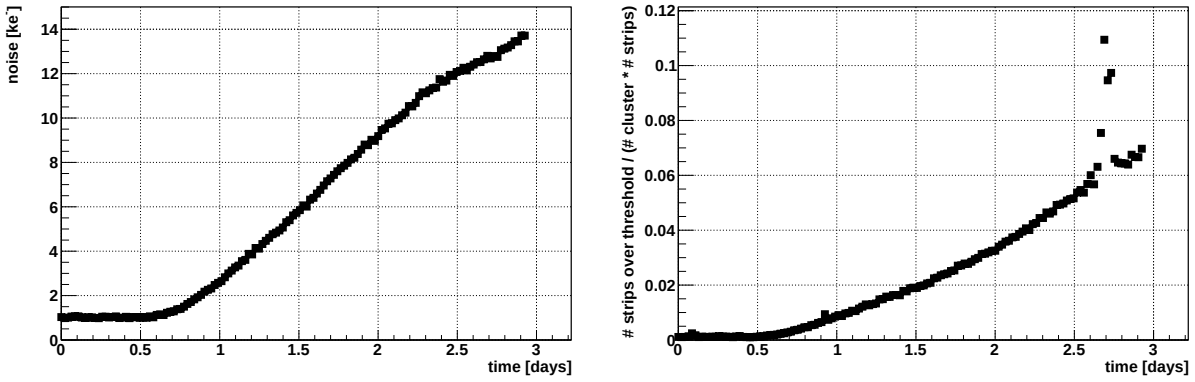

(a) Noise versus time (b) Noise occupancy versus time

Figure 8.25: Noise versus time (a) and noise occupancy versus time (b) for non-irradiated n-bulk material strip sensors at a stable bias voltage of 600 V. The source was kept in the same position during the measurement.

level of $\approx 6000\,\mathrm{ke}^-$. The next two measurements range up to 700 V. While the noise at 600 V is reduced to a normal level, it starts to increase at voltages above 600 V. From the second to the third measurement, a small noise reduction of $\approx 4000\,\mathrm{ke}^-$ at a given voltage is visible.

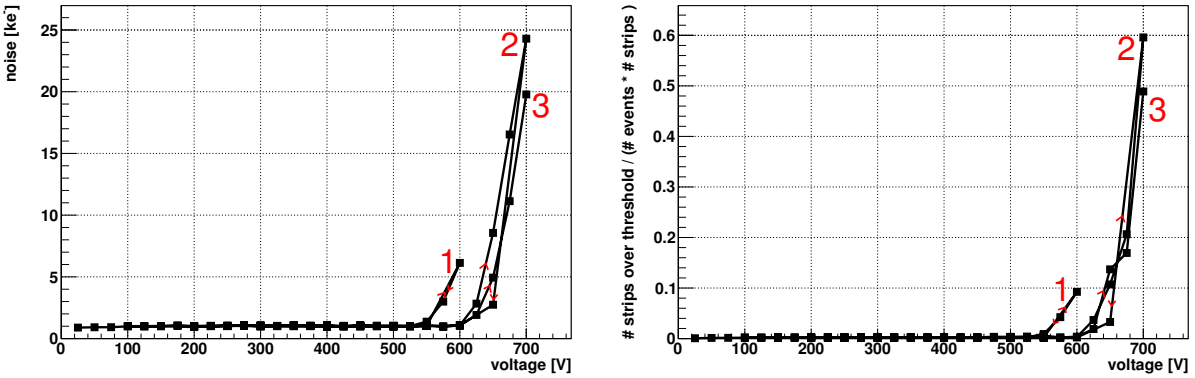

(a) Noise versus bias voltage (b) Noise occupancy versus bias voltage

Figure 8.26: Noise versus bias voltage (a) and noise occupancy versus bias voltage (b) for non-irradiated n-bulk material strip sensors. The measurements were performed several times with increasing and decreasing bias voltage to measure a hysteresis. The numbers indicate the order of measurements, the arrows indicate the direction (increase or decrease of the voltage).

The influence of the source is shown in figure 8.27. The noise profile (figure 8.27a) follows the profile of the ^{90}Sr source (figure 8.27b). This indicates that charge is created within the Si-SiO_2, hereby changing the configuration of the electrical field. This then leads to discharges in the strips creating the non-Gaussian noise or fake hits. The dependence on the bias voltage history is also visible in figure 8.26. The noise starts always slightly below the voltage at which the

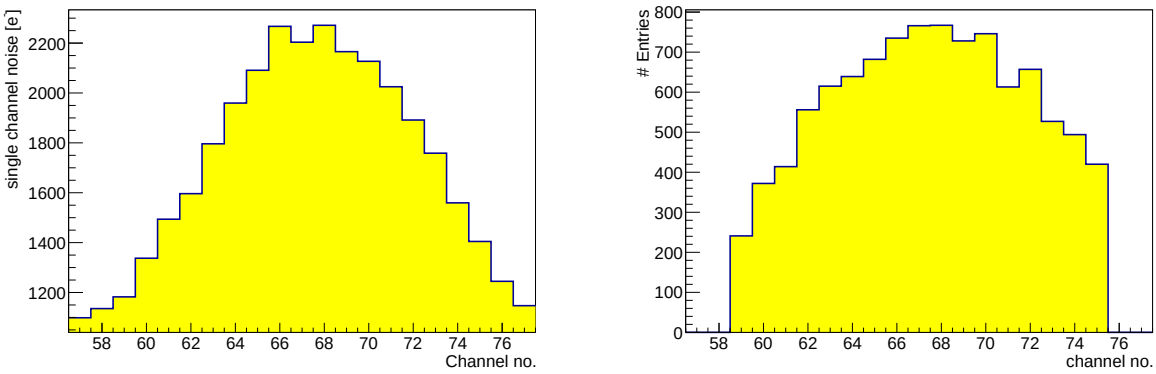

(a) Noise versus position

(b) Hitmap of the ^{90}Sr source

Figure 8.27: Noise versus position a) and the hitmap of the β source (b) for a non-irradiated n-bulk material strip sensor

sensor was kept for some time.

8.2.3 Conclusions

The noise of the irradiated and non-irradiated sensors show an increase that can be explained by charges within the Si-SiO_2 that change the configuration of the electrical field. This is supported by changes of the time constants of the noise reduction by the surface humidity.
The creation of the noise with the ^{90}Sr source in the non-irradiated sensors implies that the current design is not optimal for the operation of n-bulk silicon sensors in a environment of high levels of ionizing radiation.

8.3 Conclusions

Surface dependent effects have been found in the studied n- and p-bulk strip sensors.
In the p-bulk sensors, the change in the surface charges lead to a field configuration that resulted in an increased charge sharing and a reduced signal height and cluster finding efficiency. In the n-bulk sensors, the change in the surface charges lead to non-Gaussian noise likely caused by high electric fields close to the readout strips.
Due to the non-Gaussian noise and the resulting increase of the fake hit rate, CMS decided to concentrate on the development of p-bulk sensors. A dependence on the oxygen content of the sensor bulk material, however, was not found.

The surface structures should be further optimized to reduce the charge sharing to a minimum and make a stable operation possible.

Summary and conclusions

A variety of test-structures were produced by Hamamatsu Photonics on different kinds of silicon materials. The silicon materials were produced using different growing methods, which lead to different impurities in the silicon crystal, mainly different oxygen concentrations.
To test the different materials for their operation in the harsh radiation environment of CMS at the HL-LHC, the samples were irradiated to comparable fluences of up to
$\Phi_{neq} = 2.1 \cdot 10^{15}\,\mathrm{cm}^{-2}$. Different mixtures of protons and neutrons were used starting with a high neutron fraction corresponding to the outer layers of the CMS tracker and increasing the proton fraction towards higher fluences (inner layers).
To take the expected energy spectrum into account, the neutron irradiation was performed in a TRIGA reactor with a similar spectrum as expected for CMS at the HL-LHC. The proton irradiations were performed at accelerators with a proton energy of 23 MeV and 23 GeV, which corresponds to the lower and upper limit of the expected energy spectrum.
The most promising of the studied materials is the oxygen rich MCz, since its annealing is very weak. That would make long annealing periods possible, which would reduce the reverse current.
As a polarity, CMS chose p-bulk material with an electron readout. This choice has the advantage of a depletion zone growing from the readout side, the readout of the faster electrons (with a lower trapping probability) and no non-Gaussian noise.
However, a reduced charge collection was found in p-type sensors under certain conditions, which should be taken into account for the design of the structure of the sensors.
More specific conclusions are summarized below.

9.1 Change of bulk material characteristics with irradiation

9.1.1 Reverse current

The reverse current of the studied samples was found to be compatible to the expectation discussed in [32]. The reverse current normalized to the volume and the fluence is only dependent on the temperature of the sample and the annealing time.

9.1.2 Full depletion voltage

The development of the full depletion voltage with fluence and with annealing depends on the particle type and energy, as well as the material of the sample. The low oxygen materials show no significant dependence on the energy of the protons, while differences between proton and neutron irradiation are visible.
The dependence on the proton energy is significant for oxygen high materials, like the studied

MCz200. This can be seen in the space-charge-sign-inversion (SCSI). Depending on the proton energy, either the n-bulk or the p-bulk material underwent SCSI. The irradiation with neutron creates a higher number of acceptors in all materials than the proton irradiations do.
The irradiations of low oxygen materials in general and low energetic proton irradiation of high oxygen materials lead to a strong increase of the full depletion voltage at fluences with a high neutron fraction.
In the case of the irradiation of oxygen rich materials with high energetic protons and neutrons, the full depletion voltage is reduced, compared to an irradiation to the same fluence with protons only. This effect is called compensation.
The annealing also shows differences for oxygen rich material irradiated with high energetic protons and all other materials and irradiations. After an irradiation with neutrons and 23 MeV protons all materials follow the behavior described by the Hamburg model, discussed in [32]. After an irradiation with 23 GeV protons, however, the oxygen rich material shows very small changes of the full depletion voltage with annealing, in contrast to the oxygen lean material. The oxygen lean material has a lower full depletion voltage at the annealing condition where materials are usually compared for high fluences than the oxygen rich material. However, the strong long term annealing of the oxygen lean material makes it very prone to a high full depletion voltage at high annealing times, while the oxygen rich material is very robust in that sense.

9.1.3 Charge collection

The charge collection of the pad sensors at a given voltage and thickness depends on trapping of charge carriers and the full depletion voltage. While the trapping is independent of the material, the collected charge changes with changes of the full depletion voltage.
The collected charge determined on pad sensors with an infrared laser that penetrates the sensor over the whole depth, scaled to the expected value for a MIP (73 e^- per μm) is considered to be equal to the collected charge of a strip sensor using a β source if enough strips are taken into account.
It was shown that this assumption is correct for the case where positive signals are induced on neighboring strips and also for the case where negative signals are induced on neighboring strips. The assumption is, however, only correct, if surface effects are negligible.

9.2 Surface effects on strip sensors

The strip sensors studied in this work showed a strong dependence on the surface conditions. In the case of the p-bulk sensors, the dose rate of the used β source, lead to a reduction of the signal induced on the nearest (seed) strip, while the induced signal on neighboring strips was increased. The additional signal on the neighboring strips can not balance the loss on the seed strip, so that the total signal was reduced. The signal height in the seed strip dominates the clusterfinding efficiency, which was also reduced.
This could be explained by a change of the concentration of surface charges, in such a way that not all field lines end at the readout strips anymore. Charges drifting along field lines ending

at the surface get stuck there for a longer time than the readout signal is integrated.
In the case of the n-bulk sensors, surface charges change the electrical field in such a way that local breakdowns occur. The high field regions can be countered by charges redistributed on top of the passivation layer. This can be achieved by leaving the sensor biased for several days or weeks. A method to decrease the time of surface charge redistribution is to increase the surface conductivity by using humidity.

Appendix

In this chapter, the results of the fits with the Hamburg model from chapter 6.2 are given. This way the readability of the text in chapter 6.2 is improved.
First (1) the results of the discussion on the compensation effect will be given.
Second (2) and third (3) the results of the discussions on the Full depletion voltage after the irradiation with MeV protons and neutrons and GeV protons and neutrons wil be given, respectively.

1 Fit results - full depletion voltage after mixed irradiations (Compensation effect)

	g_a at 3 p_M [$10^{-2}\,cm^{-1}$]	g_a at 3 p_G [$10^{-2}\,cm^{-1}$]	g_a at 4 n [$10^{-2}\,cm^{-1}$]	g_{a2} at 3 p_M + 4 n [$10^{-2}\,cm^{-1}$]	g_{a2} at 3 p_G + 4 n [$10^{-2}\,cm^{-1}$]
dd-FZ220N	0.39 ± 0.16	–	0.33 ± 0.24	1.29 ± 0.24	–
dd-FZ220P	0.62 ± 0.25	–	0.46 ± 0.35	1.26 ± 0.32	–
dd-FZ300N	0.64 ± 0.11	–	0.50 ± 0.15	0.64 ± 0.12	–
dd-FZ300P	0.84 ± 0.19	–	0.54 ± 0.28	0.43 ± 0.20	–
FZ200N	–	0.73 ± 0.22	1.29 ± 0.27	–	1.31 ± 0.18
FZ200P	–	0.62 ± 0.30	1.50 ± 0.37	–	1.64 ± 0.26
MCz200N	0.37 ± 0.25	-0.66 ± 0.18	1.02 ± 0.25	1.59 ± 0.26	0.94 ± 0.14
MCz200P	0.61 ± 0.23	0.23 ± 0.17	1.17 ± 0.36	1.67 ± 0.32	2.27 ± 1.86

(a) Hamburg model parameter g_a.

	g_y at 3 p_M [$10^{-2}\,cm^{-1}$]	g_y at 3 p_G [$10^{-2}\,cm^{-1}$]	g_y at 4 n [$10^{-2}\,cm^{-1}$]	g_{y2} at 3 p_M + 4 n [$10^{-2}\,cm^{-1}$]	g_{y2} at 3 p_G + 4 n [$10^{-2}\,cm^{-1}$]
dd-FZ220N	2.21 ± 0.39	–	3.77 ± 0.49	0.54 ± 0.94	–
dd-FZ220P	4.15 ± 0.61	–	4.19 ± 0.68	0.83 ± 1.32	–
dd-FZ300N	4.18 ± 0.31	–	4.59 ± 0.34	0.00 ± 0.96	–
dd-FZ300P	4.67 ± 0.50	–	3.90 ± 0.53	0.00 ± 8.78	–
FZ200N	–	6.15 ± 0.78	2.86 ± 0.45	–	2.59 ± 0.38
FZ200P	–	7.85 ± 1.04	5.04 ± 0.68	–	2.38 ± 0.53
MCz200N	1.60 ± 0.68	-5.17 ± 0.46	3.39 ± 0.47	1.56 ± 1.02	0.00 ± 0.32
MCz200P	3.90 ± 0.58	2.50 ± 0.48	4.32 ± 0.67	1.08 ± 1.26	0.28 ± 7.58

(b) Hamburg model parameter g_y.

	N_C at 3 p_M [$10^{12}\,cm^{-3}$]	N_C at 3 p_G [$10^{12}\,cm^{-3}$]	N_C at 4 n [$10^{12}\,cm^{-3}$]	N_{C2} at 3 p_M + 4 n [$10^{12}\,cm^{-3}$]	N_{C2} at 3 p_G + 4 n [$10^{12}\,cm^{-3}$]
dd-FZ220N	5.40 ± 0.22	–	9.73 ± 0.36	10.66 ± 0.51	–
dd-FZ220P	-3.75 ± 0.33	–	-9.18 ± 0.51	-9.95 ± 0.71	–
dd-FZ300N	4.40 ± 0.16	–	7.22 ± 0.22	8.19 ± 0.18	–
dd-FZ300P	-1.68 ± 0.27	–	-7.73 ± 0.40	-7.19 ± 0.30	–
FZ200N	–	3.07 ± 0.47	7.68 ± 0.35	–	5.14 ± 0.33
FZ200P	–	-1.12 ± 0.63	-7.77 ± 0.50	–	-5.99 ± 0.49
MCz200N	5.14 ± 0.59	0.41 ± 0.25	8.54 ± 0.35	10.75 ± 0.54	2.67 ± 0.20
MCz200P	-1.63 ± 0.33	0.82 ± 0.21	-7.69 ± 0.50	-7.55 ± 0.67	0.11 ± 7.51

(c) Hamburg model parameter N_C.

Table 1: Hamburg model parameters of the fits shown in figures 6.10a to 6.11c.
For single irradiations the parameter shown is from the first irradiation term. For mixed irradiation the parameter shown describes the the second irradiation term. In this case the parameter of the first irradiation term is fixed to the corresponding value of the (first) p_M or p_G irradiation.

2 Fit results - full depletion voltage after MeV proton and neutron irradiations

Φ_{eq}	3 p_M	10 p_M	15 p_M	3 p_M + 4 n	10 p_M + 5 n
parameter	g_a	g_a	g_a	g_{a2}	g_{a2}
	$[10^{-2}\,\mathrm{cm}^{-1}]$	$[10^{-2}\,\mathrm{cm}^{-1}]$	$[10^{-2}\,\mathrm{cm}^{-1}]$	$[10^{-2}\,\mathrm{cm}^{-1}]$	$[10^{-2}\,\mathrm{cm}^{-1}]$
dd-FZ220N	0.39 ± 0.16	0.70 ± 0.13	0.55 ± 0.05	1.29 ± 0.24	0.55 ± 0.25
dd-FZ220P	0.62 ± 0.25	0.82 ± 0.15	0.85 ± 0.11	1.26 ± 0.32	0.40 ± 0.26
dd-FZ300N	0.64 ± 0.11	0.54 ± 0.07	0.37 ± 0.05	0.64 ± 0.12	0.13 ± 0.11
dd-FZ300P	0.84 ± 0.19	0.86 ± 0.10	0.79 ± 0.07	0.43 ± 0.20	0.00 ± 0.24
MCz200N	0.37 ± 0.25	1.09 ± 0.22	0.69 ± 0.08	1.59 ± 0.26	0.23 ± 0.28
MCz200P	0.61 ± 0.23	0.70 ± 2.80	0.80 ± 0.09	1.67 ± 0.32	1.18 ± 0.33

(a) Hamburg model parameter g_a.

Φ_{eq}	3 p_M	10 p_M	15 p_M	3 p_M + 4 n	10 p_M + 5 n
parameter	g_y	g_y	g_y	g_{y2}	g_{y2}
	$[10^{-2}\,\mathrm{cm}^{-1}]$	$[10^{-2}\,\mathrm{cm}^{-1}]$	$[10^{-2}\,\mathrm{cm}^{-1}]$	$[10^{-2}\,\mathrm{cm}^{-1}]$	$[10^{-2}\,\mathrm{cm}^{-1}]$
dd-FZ220N	2.21 ± 0.39	0.00 ± 4.93	0.00 ± 0.62	0.54 ± 0.94	0.02 ± 8.35
dd-FZ220P	4.15 ± 0.61	1.59 ± 0.90	0.58 ± 0.59	0.83 ± 1.32	0.00 ± 8.32
dd-FZ300N	4.18 ± 0.31	1.11 ± 0.39	0.36 ± 0.29	0.00 ± 0.96	0.00 ± 0.93
dd-FZ300P	4.67 ± 0.50	1.47 ± 0.59	0.73 ± 0.38	0.00 ± 8.82	0.00 ± 0.41
MCz200N	1.60 ± 0.68	4.24 ± 3.09	0.78 ± 0.43	1.56 ± 1.03	-4.60 ± 1.06
MCz200P	3.90 ± 0.58	0.01 ± 4.58	0.48 ± 0.50	1.08 ± 1.26	1.06 ± 1.22

(b) Hamburg model parameter g_y.

Φ_{eq}	3 p_M	10 p_M	15 p_M	3 p_M + 4 n	10 p_M + 5 n
parameter	N_C	N_C	N_C	N_C	N_C
	$[10^{12}\,\mathrm{cm}^{-3}]$	$[10^{12}\,\mathrm{cm}^{-3}]$	$[10^{12}\,\mathrm{cm}^{-3}]$	$[10^{12}\,\mathrm{cm}^{-3}]$	$[10^{12}\,\mathrm{cm}^{-3}]$
dd-FZ220N	5.40 ± 0.22	9.96 ± 0.86	10.27 ± 0.26	10.66 ± 0.51	13.95 ± 0.63
dd-FZ220P	3.75 ± 0.33	10.07 ± 0.77	12.33 ± 0.75	9.95 ± 0.71	14.51 ± 0.49
dd-FZ300N	4.40 ± 0.16	6.88 ± 0.35	9.34 ± 0.39	8.19 ± 0.18	9.91 ± 0.21
dd-FZ300P	1.68 ± 0.27	4.08 ± 0.54	4.37 ± 0.52	7.19 ± 0.30	6.70 ± 0.30
MCz200N	5.14 ± 0.59	8.11 ± 1.78	10.12 ± 0.59	10.75 ± 0.55	14.91 ± 0.71
MCz200P	1.63 ± 0.33	7.95 ± 3.00	6.45 ± 0.70	7.55 ± 0.67	11.63 ± 0.84

(c) Hamburg model parameter N_C.

Table 2: Hamburg model parameter of the fits shown in figures 6.14a to 6.15b.
For single irradiations the parameter shown is from the first irradiation term. For mixed irradiation the parameter shown is from the second irradiation term. In this case the parameter of the first irradiation term is fixed to the corresponding value of the (first) p_M irradiation.

	c $[10^{-14}\,\mathrm{cm}^2]$	c_2 $[10^{-14}\,\mathrm{cm}^2]$	g_c $[10^{-2}\,\mathrm{cm}^{-1}]$	g_{c2} $[10^{-2}\,\mathrm{cm}^{-1}]$	N_{C0} $[10^{12}\,\mathrm{cm}^{-3}]$	N_{C0_2} $[10^{12}\,\mathrm{cm}^{-3}]$
dd-FZ220N	2.99 ± 8.04	0.67 ± 9.66	0.64 ± 0.06	-1.40 ± 1.54	2.99 ± 0.10	12.05 ± 27.46
dd-FZ220P	0.54 ± 0.39	0.64 ± 9.31	0.74 ± 0.07	-1.25 ± 2.03	2.04 ± 1.89	11.88 ± 27.89
dd-FZ300N	4.13 ± 3.24	9.47 ± 5.75	0.44 ± 0.03	-1.14 ± 0.34	2.90 ± 0.14	8.34 ± 1.41
dd-FZ300P	0.18 ± 0.04	5.56 ± 5.52	0.07 ± 0.03	-2.15 ± 0.37	3.71 ± 3.52	13.68 ± 1.65
MCz200N	6.63 ± 8.02	0.47 ± 5.82	0.41 ± 0.05	1.00 ± 1.06	3.95 ± 0.47	2.01 ± 6.84
MCz200P	0.16 ± 0.09	0.66 ± 9.65	0.32 ± 0.05	0.79 ± 1.80	2.05 ± 1.42	2.98 ± 9.89

Table 3: Hamburg model parameters of the fits shown in figures 6.16 and 6.17.
For single irradiations the parameter shown is c, g_c or N_{C0}. For mixed irradiation the parameter shown is c_2, g_{c2} or N_{C0_2} of the second irradiation term. In this case the parameter c, g_c or N_{C0} of the first irradiation term is fixed to the corresponding value of the (first) p_M irradiation.

3 Fit results - full depletion voltage after GeV proton and neutron irradiations

Φ_{eq} parameter	3 p_G g_a $[10^{-2}\,cm^{-1}]$	10 p_G g_a $[10^{-2}\,cm^{-1}]$	15 p_G g_a $[10^{-2}\,cm^{-1}]$	3 p_G + 4 n g_{a2} $[10^{-2}\,cm^{-1}]$	10 p_G + 5 n g_{a2} $[10^{-2}\,cm^{-1}]$	15 p_G + 6 n g_{a2} $[10^{-2}\,cm^{-1}]$
FZ200N	0.80 ± 0.24	0.68 ± 0.09	0.56 ± 0.39	1.28 ± 0.18	0.24 ± 0.15	0.16 ± 0.15
FZ200P	0.68 ± 0.32	0.45 ± 0.11	0.46 ± 0.08	1.61 ± 0.26	0.87 ± 0.20	0.57 ± 0.12
MCz200N	-1.21 ± 0.33	-0.00 ± 4.59	-0.41 ± 0.45	1.72 ± 0.16	0.32 ± 0.15	0.27 ± 0.17
MCz200P	0.48 ± 0.31	-0.00 ± 0.25	-0.16 ± 0.41	1.42 ± 0.20	0.67 ± 0.17	0.48 ± 0.14

(a) Hamburg model parameter g_a.

Φ_{eq} parameter	3 p_G g_y $[10^{-2}\,cm^{-1}]$	10 p_G g_y $[10^{-2}\,cm^{-1}]$	15 p_G g_y $[10^{-2}\,cm^{-1}]$	3 p_G + 4 n g_{y2} $[10^{-2}\,cm^{-1}]$	10 p_G + 5 n g_{y2} $[10^{-2}\,cm^{-1}]$	15 p_G + 6 n g_{y2} $[10^{-2}\,cm^{-1}]$
FZ200N	6.35 ± 0.80	3.92 ± 0.16	0.00 ± 6.28	2.55 ± 0.38	0.96 ± 0.38	0.00 ± 0.24
FZ200P	8.12 ± 1.06	3.88 ± 0.18	2.81 ± 0.13	2.30 ± 0.53	1.64 ± 0.46	1.09 ± 0.05
MCz200N	-5.35 ± 0.48	-0.53 ± 0.06	-0.51 ± 0.06	4.76 ± 0.30	0.56 ± 0.27	0.49 ± 0.37
MCz200P	2.59 ± 0.49	-0.12 ± 0.06	-0.31 ± 0.05	2.25 ± 0.38	0.68 ± 0.29	0.26 ± 0.23

(b) Hamburg model parameter g_y.

Φ_{eq} parameter	3 p_G N_C $[10^{12}\,cm^{-3}]$	10 p_G N_C $[10^{12}\,cm^{-3}]$	15 p_G N_C $[10^{12}\,cm^{-3}]$	3 p_G + 4 n N_{C2} $[10^{12}\,cm^{-3}]$	10 p_G + 5 n N_{C2} $[10^{12}\,cm^{-3}]$	15 p_G + 6 n N_{C2} $[10^{12}\,cm^{-3}]$
FZ200N	3.05 ± 0.47	3.00 ± 0.51	3.90 ± 4.11	5.08 ± 0.33	4.88 ± 0.39	4.35 ± 0.45
FZ200P	1.08 ± 0.63	1.22 ± 0.61	0.86 ± 0.62	5.93 ± 0.49	3.75 ± 0.49	3.57 ± 0.29
MCz200N	-0.37 ± 0.25	3.59 ± 0.29	6.18 ± 0.40	6.76 ± 0.30	12.36 ± 0.40	14.41 ± 0.50
MCz200P	3.26 ± 0.22	8.28 ± 0.26	11.30 ± 0.38	2.53 ± 0.36	5.74 ± 0.41	8.18 ± 0.44

(c) Hamburg model parameter N_C.

Table 4: Hamburg model parameter of the fits shown in figures 6.18a to 6.20c.
For single irradiations the parameter shown is from the first irradiation term. For mixed irradiation the parameter shown is from the second irradiation term. In this case the parameter of the first irradiation term is fixed to the corresponding value of the (first) p_G irradiation.

	c $[10^{-14}\,cm^2]$	c_2 $[10^{-14}\,cm^2]$	g_c $[10^{-2}\,cm^{-1}]$	g_{c2} $[10^{-2}\,cm^{-1}]$	N_{C0} $[10^{12}\,cm^{-3}]$	N_{C0_2} $[10^{12}\,cm^{-3}]$
FZ200N	9.12 ± 5.37	0.57 ± 0.31	0.01 ± 0.16	-0.61 ± 0.11	2.99 ± 2.03	5.00 ± 9.80
FZ200P	4.42 ± 7.68	4.27 ± 5.64	0.01 ± 0.01	-1.40 ± 0.33	0.96 ± 0.33	10.22 ± 1.72
MCz200N	0.18 ± 0.04	0.08 ± 0.22	0.58 ± 0.02	1.23 ± 0.85	-3.20 ± 0.00	5.99 ± 11.00
MCz200P	5.57 ± 7.69	3.31 ± 8.00	0.62 ± 0.02	-1.18 ± 0.33	1.49 ± 0.18	3.70 ± 5.57

Table 5: Hamburg model parameters of the fits shown in figures 6.21 and 6.22.
For single irradiations the parameter shown is c, g_c or N_{C0}. For mixed irradiation the parameter shown is c_2, g_{c2} or N_{C0_2} of the second irradiation term. In this case the parameter c, g_c or N_{C0} of the first irradiation term is fixed to the corresponding value of the (first) p_G irradiation.

Bibliography

[1] CERN Press Office Photo Selection, 2013. URL http://cds.cern.ch/collection/Photos.

[2] The ALICE Collaboration. The ALICE experiment at the CERN LHC. *Journal of Instrumentation*, 3(08):S08002, 2008. URL http://stacks.iop.org/1748-0221/3/i=08/a=S08002.

[3] The ATLAS Collaboration. The ATLAS Experiment at the CERN Large Hadron Collider. *Journal of Instrumentation*, 3(08):S08003, 2008. URL http://stacks.iop.org/1748-0221/3/i=08/a=S08003.

[4] The LHCb Collaboration. The LHCb Detector at the LHC. *Journal of Instrumentation*, 3(08): S08005, 2008. URL http://stacks.iop.org/1748-0221/3/i=08/a=S08005.

[5] The CMS Collaboration. The CMS experiment at the CERN LHC. *Journal of Instrumentation*, 3(08):S08004, 2008. URL http://stacks.iop.org/1748-0221/3/i=08/a=S08004.

[6] David Barney, 2004. URL https://cms-docdb.cern.ch/cgi-bin/PublicDocDB/ShowDocument?docid=4172.

[7] The CMS Collaboration. *CMS Physics: Technical Design Report Volume 1: Detector Performance and Software*. Technical Design Report CMS. CERN, Geneva, 2006.

[8] L. Rossi. LHC Upgrade Plans: Options and Strategy. *Conf.Proc.*, C110904:908–912, 2011.

[9] M Tytgat et al. The upgrade of the cms rpc system during the first lhc long shutdown. *Journal of Instrumentation*, 8(02):T02002, 2013. URL http://stacks.iop.org/1748-0221/8/i=02/a=T02002.

[10] D Abbaneo et al. An overview of the design, construction and performance of large area triple-gem prototypes for future upgrades of the cms forward muon system. *Journal of Instrumentation*, 7(05):C05008, 2012. URL http://stacks.iop.org/1748-0221/7/i=05/a=C05008.

[11] CMS Collaboration. CMS Technical Design Report for the Pixel Detector Upgrade. Technical report, 2012.

[12] Jacob Anderson and the CMS Hcal Collaboration. Upgrade of the cms hadron calorimeter for an upgraded lhc. *Journal of Physics: Conference Series*, 404(1):012019, 2012. URL http://stacks.iop.org/1742-6596/404/i=1/a=012019.

[13] Oliver Pooth. Muon track fast tag : A muon trigger upgrade for cms at the hl-lhc. Technical Report CMS-CR-2012-310. CERN-CMS-CR-2012-310, CERN, Geneva, Nov 2012.

[14] Stefano Mersi. CMS silicon tracker upgrade for HL-LHC. *PoS*, RD11:030, 2011.

[15] A. Annovi, G. Broccolo, A. Ciocci, P. Giannetti, F. Ligabue, et al. Associative memory for L1 track triggering in LHC environment. *Real Time Conference (RT), 2012 18th IEEE-NPSS*, 2012. doi: 10.1109/RTC.2012.6418193.

[16] S.M. Sze and Kwok K. Ng. *p-n Junctions*. John Wiley & Sons, Inc., 2006. ISBN 9780470068328. doi: 10.1002/0470068329.

[17] Frank Hartmann. Evolution of Silicon Sensor Technology in Particle Physics. *Springer Tracts Mod.Phys.*, 231:1–204, 2009.

[18] A. Chilingarov. Generation current temperature scaling. Technical report, Lancaster University, 2011. URL `http://rd50.web.cern.ch/RD50/doc/Internal/rd50_2011_001-I-T_scaling.pdf`.

[19] J. Beringer et. al. (Particle Data Group). The Review of Particle Physics. *Physical Review D*, 86:010001, 2012. URL `http://pdg.lbl.gov`.

[20] Donald E. Groom, Nikolai V. Mokhov, and Sergei I. Striganov. MUON STOPPING POWER AND RANGE TABLES 10 MeV–100 TeV. *Atomic Data and Nuclear Data Tables*, 78(2):183 – 356, 2001. ISSN 0092-640X. doi: 10.1006/adnd.2001.0861. URL `http://www.sciencedirect.com/science/article/pii/S0092640X01908617`.

[21] NIST SRD 124 Stopping-Power and Range Tables for Electrons, Protons, and Helium Ions. http://physics.nist.gov/PhysRefData/Star/Text/ESTAR.html, Release August 2005. URL `http://www.nist.gov/pml/data/star/index.cfm`.

[22] Stephen M. Seltzer and Martin J. Berger. Evaluation of the collision stopping power of elements and compounds for electrons and positrons. *The International Journal of Applied Radiation and Isotopes*, 33(11):1189 – 1218, 1982. ISSN 0020-708X. doi: 10.1016/0020-708X(82)90244-7. URL `http://www.sciencedirect.com/science/article/pii/0020708X82902447`.

[23] Stephen M. Seltzer and Martin J. Berger. Improved procedure for calculating the collision stopping power of elements and compounds for electrons and positrons. *The International Journal of Applied Radiation and Isotopes*, 35(7):665 – 676, 1984. ISSN 0020-708X. doi: 10.1016/0020-708X(84)90113-3. URL `http://www.sciencedirect.com/science/article/pii/0020708X84901133`.

[24] R.H. Pratt, H.K. Tseng, C.M. Lee, Lynn Kissel, Crawford MacCallum, and Merle Riley. Bremsstrahlung energy spectra from electrons of kinetic energy 1 keV $\leq T_1 \leq$ 2000 keV incident on neutral atoms $2 \leq Z \leq 92$. *Atomic Data and Nuclear Data Tables*, 20(2):175 – 209, 1977. ISSN 0092-640X. doi: 10.1016/0092-640X(77)90045-6. URL `http://www.sciencedirect.com/science/article/pii/0092640X77900456`.

[25] L. Landau. On the energy loss of fast particles by ionization. *J.Phys.(USSR)*, 8:201–205, 1944.

[26] G. Kramberger, V. Cindro, I. Dolenc, E. Fretwurst, G. Lindström, I. Mandić, M. Mikuž, and M. Zavrtanik. Charge collection properties of heavily irradiated epitaxial silicon detectors. *Nuclear Instruments and Methods in Physics Research Section A: Accelerators, Spectrometers, Detectors and Associated Equipment*, 554(1–3):212 – 219, 2005. ISSN 0168-9002. doi: 10.1016/j.nima.2005.08.066. URL http://www.sciencedirect.com/science/article/pii/S016890020501675X.

[27] Alexandra Junkes. *Influence of Radiation Induced Defect Clusters on Silicon Particle Detectors*. PhD thesis, University of Hamburg, 2011. URL http://www-library.desy.de/preparch/desy/thesis/desy-thesis-11-031.pdf.

[28] A. Ruzin, G. Casse, M. Glaser, A. Zanet, F. Lemeilleur, and S. Watts. Comparison of radiation damage in silicon induced by proton and neutron irradiation. *Nuclear Science, IEEE Transactions on*, 46(5):1310–1313, 1999. ISSN 0018-9499. doi: 10.1109/23.795808.

[29] Michael Moll. *Radiation damage in silicon particle detectors: Microscopic defects and macroscopic properties*. PhD thesis, Universty of Hamburg, 1999. URL http://www-library.desy.de/cgi-bin/showprep.pl?desy-thesis-99-040.

[30] M. Huhtinen. Simulation of non-ionising energy loss and defect formation in silicon. *Nucl.Instrum.Meth.*, A491:194–215, 2002. doi: 10.1016/S0168-9002(02)01227-5.

[31] A Akkerman, J Barak, M.B Chadwick, J Levinson, M Murat, and Y Lifshitz. Updated niel calculations for estimating the damage induced by particles and γ-rays in si and gaas. *Radiation Physics and Chemistry*, 62(4):301 – 310, 2001. ISSN 0969-806X. doi: 10.1016/S0969-806X(01)00207-9. URL http://www.sciencedirect.com/science/article/pii/S0969806X01002079.

[32] G. Lindström, M. Moll, and E. Fretwurst. Radiation hardness of silicon detectors - a challenge from high-energy physics. *Nuclear Instruments and Methods in Physics Research Section A: Accelerators, Spectrometers, Detectors and Associated Equipment*, 426(1):1 – 15, 1999. ISSN 0168-9002. doi: 10.1016/S0168-9002(98)01462-4.

[33] Renate Wunstorf. *A Systematic investigation of the radiation hardness of silicon detectors for high-energy physics experiments*. PhD thesis, Universty of Hamburg, 1992.

[34] Thomas Poehlsen. *Charge Losses in Silicon Sensors and Electric Field Studies at the Si-SiO_2 Interface*. PhD thesis, University of Hamburg, 2013.

[35] Agilent Technologies Inc. E4980A Precision LCR Meter Users Guide, May 2013. URL http://www.home.agilent.com/en/pd-715495-pn-E4980A/precision-lcr-meter-20-hz-to-2-mhz.

[36] Thomas Pöhlsen, 2013. Private communication.

[37] R. Marco-Hernandez. A portable readout system for microstrip silicon sensors (alibava). *Nuclear Science, IEEE Transactions on*, 56(3):1642–1649, 2009. ISSN 0018-9499. doi: 10.1109/TNS.2009.2017261.

[38] Löchner, S. and Schmelling, M. The Beetle Reference Manual - chip version 1.3, 1.4 and 1.5. 2006.

[39] J.J. Devaney. Beta spectra of ^{90}Sr and ^{90}Y. Technical report, Los Alamos National Lab., NM (USA), Aug 1985.

[40] Sergej Schuwalow, 2013. Private communication.

[41] O. Blunck and S. Leisegang. Zum Energieverlust schneller Elektronen in dünnen Schichten. *Zeitschrift für Physik*, 128(4):500–505, 1950. ISSN 0044-3328. doi: 10.1007/BF01330032.

[42] Adam Barcz. Institute of Electron Technology at Al. Lotnikow 32/46 in Warsaw.

[43] G. Lindström et. al. Radiation hard silicon detectors—developments by the {RD48} (rose) collaboration. *Nuclear Instruments and Methods in Physics Research Section A: Accelerators, Spectrometers, Detectors and Associated Equipment*, 466(2):308 – 326, 2001. ISSN 0168-9002. doi: 10.1016/S0168-9002(01)00560-5. URL `http://www.sciencedirect.com/science/article/pii/S0168900201005605`.

[44] Alexander Dierlamm. Characterisation of silicon sensor materials and designs for the CMS Tracker Upgrade. In *PoS(Vertex 2011)*, PoS. Sissa, 2012. URL `http://pos.sissa.it/cgi-bin/reader/conf.cgi?confid=167`.

[45] Moritz Guthoff, 2014. PhD thesis in preparation.

[46] Luka Snoj and Gašper Žerovnik and Andrej Trkov. Computational analysis of irradiation facilities at the jsi triga reactor. *Applied Radiation and Isotopes*, 70(3):483 – 488, 2012. ISSN 0969-8043. doi: 10.1016/j.apradiso.2011.11.042. URL `http://www.sciencedirect.com/science/article/pii/S0969804311005963`.

[47] M. Glaser, F. Ravotti, and M. Moll. Dosimetry assessments in the irradiation facilities at the cern-ps accelerator. *Nuclear Science, IEEE Transactions on*, 53(4):2016–2022, 2006. ISSN 0018-9499. doi: 10.1109/TNS.2006.880569.

[48] Alexander Dierlamm, 2013. URL `http://www.ekp.kit.edu/english/264.php`.

[49] Alexander Dierlamm. Proton irradiation in karlsruhe. In *16th RD50 Workshop*. CERN, 2010. URL `http://indico.cern.ch/getFile.py/access?contribId=19&sessionId=3&resId=1&materialId=slides&confId=86625`.

[50] W.G. Oldham and S.S. Naik. Admittance of p-n junctions containing traps. *Solid-State Electronics*, 15(10):1085 – 1096, 1972. ISSN 0038-1101. doi: http://dx.doi.org/10.1016/0038-1101(72)90167-0. URL `http://www.sciencedirect.com/science/article/pii/0038110172901670`.

[51] Zheng Li and H.W. Kraner. Studies of frequency dependent c-v characteristics of neutron irradiated p+-n silicon detectors. *Nuclear Science, IEEE Transactions on*, 38(2):244–250, 1991. ISSN 0018-9499. doi: 10.1109/23.289304.

[52] Thomas Poehlsen, Eckhart Fretwurst, Robert Klanner, Sergej Schuwalow, Jörn Schwandt, and Jiaguo Zhang. Charge losses in segmented silicon sensors at the si–sio2 interface. *Nuclear Instruments and Methods in Physics Research Section A: Accelerators, Spectrometers, Detectors and Associated Equipment*, 700(0):22 – 39, 2013. ISSN 0168-9002. doi: http://dx.doi.org/10.1016/j.nima.2012.10.063. URL http://www.sciencedirect.com/science/article/pii/S0168900212012090.

[53] G. Kramberger, V. Cindro, I. Dolenc, I. Mandić, M. Mikuž, and M. Zavrtanik. Performance of silicon pad detectors after mixed irradiations with neutrons and fast charged hadrons. *Nuclear Instruments and Methods in Physics Research Section A: Accelerators, Spectrometers, Detectors and Associated Equipment*, 609(2–3):142 – 148, 2009. ISSN 0168-9002. doi: http://dx.doi.org/10.1016/j.nima.2009.08.030. URL http://www.sciencedirect.com/science/article/pii/S0168900209016088.

[54] E. Fretwurst, F. Hönniger, G. Kramberger, G. Lindström, I. Pintilie, and R. Röder. Radiation damage studies on {MCz} and standard and oxygen enriched epitaxial silicon devices. *Nuclear Instruments and Methods in Physics Research Section A: Accelerators, Spectrometers, Detectors and Associated Equipment*, 583(1):58 – 63, 2007. ISSN 0168-9002. doi: http://dx.doi.org/10.1016/j.nima.2007.08.194. URL http://www.sciencedirect.com/science/article/pii/S0168900207019031.

[55] G Lindström, S Watts, and F Lemeilleur. 3rd RD48 status report: the ROSE collaboration (R&D on silicon for future experiments). Technical Report CERN-LHCC-2000-009, CERN, Geneva, Dec 1999.

[56] Michael Moll. RD50 Status Report 2009/2010 - Radiation hard semiconductor devices for very high luminosity colliders. Technical Report CERN-LHCC-2012-010. LHCC-SR-004, CERN, Geneva, Jun 2012.

[57] Simon Ramo. Currents induced by electron motion. *Proceedings of the IRE*, 27(9):584–585, 1939. ISSN 0096-8390. doi: 10.1109/JRPROC.1939.228757.

[58] W. Shockley. Currents to conductors induced by a moving point charge. *Journal of Applied Physics*, 9(10):635–636, 1938. doi: http://dx.doi.org/10.1063/1.1710367. URL http://scitation.aip.org/content/aip/journal/jap/9/10/10.1063/1.1710367.

[59] Helmuth Spieler. Lectures on Detector Techniques - Semiconductor Detectors Part 1. Oct 1998. URL http://www-physics.lbl.gov/~spieler/SLAC_Lectures/PDF/Sem-Det-I.pdf.

[60] Andreas Nürnberg, 2014. PhD thesis in preparation.

[61] E. Belau, R. Klanner, G. Lutz, E. Neugebauer, H.J. Seebrunner, A. Wylie, T. Böhringer, L. Hubbeling, P. Weilhammer, J. Kemmer, U. Kötz, and M. Riebesell. Charge collection in silicon strip detectors. *Nuclear Instruments and Methods in Physics Research*, 214(2–3):253 – 260, 1983. ISSN 0167-5087. doi: http://dx.doi.org/10.1016/0167-5087(83)90591-4. URL http://www.sciencedirect.com/science/article/pii/0167508783905914.

[62] Jörn Schwandt, 2013. private communication.

[63] M. Huhtinen. The Radiation environment at the CMS experiment at the LHC. 1996.

List of Figures

List of Tables

Acknowledgements

First I want to thank Georg Steinbrück for the discussions and suggestions during my work and especially during the writing of this thesis. Also thanks to Eckhart Fretwurst, Robert Klanner, Alexandra Junkes, Sergej Schuwalow, Erika Garutti and Doris Eckstein for discussions and critical questions. Thank you Jörn Schwandt and Sergej Schuwalow for simulating electric fields and the particle distribution of the β-source.
I also want to thank the particle physics group in Hamburg for the nice talks, board game evenings and BBQs. Special thanks to the colleagues in my office: Thomas Pöhlsen, Christian Scharf, Henning Kröhnke, Ole Brandt, Christian Henkel and Viktor Danescu.
Thank you colleagues in the CMS tracker collaboration, especially Karl-Heinz Hoffmann, Andreas Nürnberg, Robert Eber and Alexander Dierlamm. Also thank to the RD50 collaboration for interesting meetings and good discussions, especially Nicola Pacifico, Marcos Fernandez Garcia, Irena Dolenc Kittelmann and Michael Moll.
Also many thanks to the people in the lab that make measurements possible: Michael Matysek, Peter Buhmann, Wolfgang Gärtner, Rainer-Peter Feller and Ronald Mohrmann. And thank you HIWI-students for making thousands of measurements.
I also want to thank my family for their support during the years of study. Without you this work would not exist.
The research leading to the results of this thesis has received funding from the European Commission under the FP7 Research Infrastructures project AIDA, grant agreement no 262025.
This work is supported by the Initiative and Networking Fund of the Helmholtz Association, contract HA-101 ("Physics at the Terascale").

Finally thank you Yahweh, God of Abraham, Isaac and Jacob. Thank you for making live worth living.

„Falls Gott die Welt geschaffen hat, war seine Hauptsorge sicher nicht, sie so zu machen, dass wir sie verstehen können."[2]

[2] Albert Einstein

Selbständigkeitserklärung

Ich erkläre, dass ich die vorliegende Arbeit selbständig und nur unter Verwendung der angegebenen Literatur und Hilfsmittel angefertigt habe.

Hamburg, den 5. Mai 2014 Joachim Erfle